DMYTRO GREBENNIKOV

Influence of Nonstoichiometry in $Ba_3BNb_2O_9$ on Microwave Properties

INFLUENCE OF NONSTOICHIOMETRY IN $Ba_{3+3x}B_{1+y}Nb_2O_9$ (B=Co or Zn) PEROVSKITES ON THE MICROWAVE PROPERTIES

By

DMYTRO GREBENNIKOV, M.A.Sc.

A Thesis

Submitted to the School of Graduate Studies

In Partial Fulfillment of the Requirements

For the Degree

Doctor of Philosophy

McMaster University

DOCTOR OF PHILOSOPHY (2011) **McMASTER UNIVERSITY**

(Engineering Physics) Hamilton, Ontario, Canada

TITLE	Influence of Nonstoichiometry in $Ba_{3+3x}B_{1+y}Nb_2O_9$ (B=Co or Zn) Perovskites on the Microwave Properties
AUTHOR	Dmytro Grebennikov, M.A.Sc. (McMaster University)
SUPERVISOR	Professor Peter Mascher
NUMBER OF PAGES	xx, 174

Abstract

Near stoichiometric compositions of $Ba_{3+3x}B_{1+y}Nb_2O_9$ (B = Co or Zn) perovskites were studied by microstructure analysis and optical techniques. Materials considered in the present research belong to the family of perovskites exhibiting disorder-1:2 order phase transitions that are important for microwave applications. It was found that deviation from stoichiometry involving cation deficiencies on Ba- or B-positions facilitates formation of an ordered structure for small values of cation deficiencies. Excessive deviation from the nominal values as well as introduction of extra cations destabilizes the perovskite structure leading to the precipitation of secondary phases.

Formation of a Ba-deficient $Ba_6BNb_9O_{30}$ (B = Co or Zn) phase influences the grain growth rate through reduction in the surface energy of grains. In combination with large strain in precursor materials caused by applied pressure during fabrication and high sintering temperature this results in increased porosity and lower density.

Appearance of Raman active modes in the considered $Ba_{3+3x}B_{1+y}Nb_2O_9$ materials was attributed to the formation of a 1:2 cation ordered structure. It was shown that microwave losses are influenced by the degree of 1:2 cation ordering that depends on the formation of secondary phases as well as a densification process. The appearance of an "extra" peak in Raman spectra was attributed to the formation of 1:1 cation order described based on the "space-charge" model. Changes in the position of the mode, attributed to "breathing-type" vibrations of oxygen anions from materials having

"partially" ordered 1:1 structure to those having 1:2 ordered structure, indicate formation of more rigid oxygen octahedra associated with lower microwave losses.

Structural distortion caused by 1:2 cation ordering results in changes in the mutual orientation of transition metal-ligand molecular orbitals and the appearance of two emission bands signifying formation of two different NbO_6 octahedra. The first octahedron, present in the 1:2 ordered structure, gives origin to the lower energy photoluminescence band, while the second one, forming a disordered cubic structure, produces an emission peak at higher energies with the variation in the position of the maximum depending on the type of cation on the B-site. Changes in the maximum position of the high-energy peak were attributed to different structure distortions caused by off-center motion of Nb^{5+} and stabilization by neighboring BO_6 octahedra. The stabilization power of BO_6 octahedra depends on the covalency of B-O bonds and is larger for cobalt containing perovskites.

Acknowledgements

There are a number of people who helped me throughout the course of this research.

First of all, I want to express my thanks to my supervisor, Prof. Peter Mascher, for his guidance, constant encouragement and generous support of this work. I am indebted to him for providing me with freedom to work on what I was interested in.

I am grateful to Dr. Antoni Dabkowski for introducing me to the field of oxide materials and numerous discussions on samples' preparation and characterization. His tremendous experience in the area of oxides helped me to accomplish this research.

I extend my thanks to Evgueni Chelomentsev for discussions on materials' properties and help on samples' characterization during the time I spent working on this project.

I would like to thank a number of people at McMaster University. Prof. Yurij Mozharivskyj for help in X-ray diffraction measurements and Wen He Gong for advice on properties of studied materials and help in analysis of crystallographic data. Technical assistance and discussion on design of an experimental setup provided by Jim Garrett are greatly appreciated.

I want to acknowledge help of Fred Pearson and Julia Huang for introduction to the field of TEM measurement and help in samples' preparation. I am thankful to Steve Koprich for help with SEM measurements.

Thanks to Prof. Anatoli Belous and his research group from the Institute of General and Inorganic Chemistry, Kyiv, Ukraine, for the provided perovskite materials.

I thank Grzegorz Szymanski (Guelph University) for providing me with access to the Raman system and guidance during Raman measurements.

I wish to acknowledge the financial support of the Natural Sciences and Engineering Research Council of Canada.

Contents

List of Figures

List of Tables

Notations and Abbreviations

BMT	$Ba(Mg_{1/3}Ta_{2/3})O_3$
BZT	$Ba(Zn_{1/3}Ta_{2/3})O_3$
BMN	$Ba(Mg_{1/3}Nb_{2/3})O_3$
BZN	$Ba(Zn_{1/3}Nb_{2/3})O_3$
BNN	$Ba(Ni_{1/3}Nb_{2/3})O_3$
BCN	$Ba(Co_{1/3}Nb_{2/3})O_3$
XRD	X-ray diffraction [technique]
t	tolerance factor
Q	quality factor
Qxf	product of quality factor and resonance frequency
ε_r	dielectric constant
τ_f	temperature coefficient of the resonant frequency
τ_ε	temperature coefficient of the dielectric constant
R_i	ionic radius
FWHM	full width at half maximum
PLS	positron lifetime spectroscopy
PL	photoluminescence
TM	transition metal

List of Publications and Presentations

Publications

D. Grebennikov and P. Mascher. Photoluminescent properties of $Ba(B'_{1/3}B''_{2/3})O_3$ (B' = Mg, Co or Zn, B" = Nb or Ta) ceramics with perovskite structure. Accepted for publication in J. Luminescence.

D. Grebennikov and P. Mascher. Structural properties of near-stoichiometric composition of $Ba(B'_{1/3}B''_{2/3})O_3$ (B' = Mg, Co or Zn, B" = Nb or Ta) perovskites. J. Mater. Res., 26(9), 2011

D. Grebennikov, O. Ovchar, A. Belous and P. Mascher. Application of positron annihilation and Raman spectroscopies to the study of perovskite type materials. J. Appl. Phys., 108:114109, 2010.

H. Seyedrezai, **D. Grebennikov**, P. Mascher and H.S. Zurob. Study of the early stages of clustering in Al–Mg–Si alloys using the electrical resistivity measurements. Mater. Sci. Eng. A, 525:186, 2009.

A. Belous, O. Ovchar, B. Jancar, M. Spreitzer, G. Annino, **D. Grebennikov**, and P. Mascher. The effect of chemical composition on the structure and dielectric properties of the columbites $A^{2+}Nb_2O_6$. J. Electrochem. Soc., 156:206, 2009.

O. Ovchar, A. Belous, O. Kramarenko, D. Mischuk, B. Jancar, M. Spreitzer, D. Suvorov, G. Annino, **D. Grebennikov**, and P. Mascher. The Effect of Impurity Phases on the Structure and Properties of Microwave Dielectrics based on Complex Perovskites $Ba(Co_{1/3}Nb_{2/3})O_3$. Ferroelectrics, 387:189, 2009.

A. Belous, O. Ovchar, O. Kramarenko, D. Mischuk, B. Jancar, M. Spreitzer, D. Suvorov, G. Annino, **D. Grebennikov**, and P. Mascher. Low-loss Perovskite Niobates $Ba(M^{2+}_{1/3}Nb_{2/3})O_3$: Composition, Structure, and Microwave Dielectric Properties. Ferroelectrics, 387:36, 2009.

D. Grebennikov, O. Ovchar, S. Neretina, A. Belous and P. Mascher. Characterization of columbite ceramics $A_{1-x}Nb_2O_6$ by positron annihilation spectroscopy. Physica Status Solidi(c), 4:3835, 2007.

S. Neretina, **D. Grebennikov**, R.A. Hughes, M. Weber, K.G. Lynn, P.J. Simpson, J.S Preston and P. Mascher. Defect Characterization of CdTe thin films using a slow positron beam. Physica Status Solidi(c), 4:3659, 2007.

Presentations

D. Grebennikov, O. Ovchar, A. Belous and P. Mascher. The International Workshop on Positron Studies of Defects, Prague, Czech Republic, 2008.

D. Grebennikov, O. Ovchar, A. Belous and P. Mascher. 19th Canadian Materials Science Conference, McMaster University, 2007.

Chapter 1

Introduction

The versatility of modern electronics depends on the ability of industries to produce smaller and cheaper components. Developments in microwave-based communication technologies triggered an extensive search for new materials suitable for microwave applications. In spite of the large variety of materials being studied, only a limited number of them can be used for mass production. Progress in the industry of semiconductors resulted in a significant miniaturization of microwave components. Initial improvements were achieved by the development of microstrip resonators on plastic or alumina substrates. The application of high temperature superconductors used in combination with high permittivity dielectrics also demonstrates miniaturization potential. Microwave filters with low insertion losses, composed of a superconducting microstrip on a high dielectric substrate were realized [1]. Cooling requirements for such systems, however, significantly restricted their industrial applications and left cavity-based dielectric resonators as the main candidate for the fabrication of microwave components.

Currently there are several groups of ceramic materials used for application in dielectric resonators [2]. The suitability of these ceramics or other materials for microwave application is determined based on their quality factor (Q), dielectric constant (ε_r) and the temperature coefficient of the resonant frequency (τ_f). By increasing the operational frequency, the quality factor of the system is determined mainly by losses

inside of the dielectric material composing the resonator. A more thorough description of the factors influencing ceramic losses in the studied microwave range will be given in the subsequent sections of this thesis. Restrictions on the value of the dielectric constant arise from the demand of consumers to miniaturize the final product. The size of the resonator depends on the inverse of the square root of the dielectric constant. Thus, in order to realize a product with small dimensions, dielectric materials with large dielectric constants are required. Ferroelectric materials like, for example, $BaTiO_3$ having a dielectric constant of 1500 would be advantageous from the point of view of the final resonator size, but significant losses in the microwave range made this class of materials unsuitable for microwave applications [2].

The required stability of the resulting oscillators and filters at different operating temperatures imposes restrictions on the temperature behavior of the ceramic material: the temperature coefficient of resonance frequency should be zero. Zirconium titanate-based materials $(Zr,Sn)TiO_4$ have been recognized as temperature stable dielectrics. Temperature stability and high quality factors are realized in this system by incorporation of Sn atoms. Within the ZrO_2-TiO_2-SnO_2 system, single-phase materials exist only over a limited range of compositions. Although it is possible to substitute Sn for both Ti and Zr, the best properties are obtained for materials with pure Zr substitution, $Zr_{1-x}Sn_xTiO_4$. At compositions between $0.2 < x < 0.3$, the measured dielectric constant was 38, τ_f = 1-5 ppm $°C^{-1}$, and the maximum value of the quality factor was 7000-10000 [3].

Among the first practical dielectric materials were binary barium titanates: $BaTi_4O_9$ and $Ba_2Ti_9O_{20}$ [4,5]. The former exhibits ε = 38, τ_f = 14ppm $°C^{-1}$, and

Q>10000, while the latter having a similar dielectric constant and quality factor, shows better temperature stability (τ_f = 4ppm $°C^{-1}$) [6]. In spite of good compliance with the requirements for dielectric resonators, these materials are highly sensitive to preparation conditions. Because of the relatively low proportion of the valence-stabilizing electropositive elements like Ba or Zr (used as additives to change the temperature behavior), the quality factor is highly susceptible to the defect chemistry. Under normal ceramic processing conditions, Ti^{4+} is easily reduced to Ti^{3+}, producing an electron. Introduction of electrical conductivity due to electrons reduces Q-values [2]. This was one of the main limiting factors in the mass production of Ba- and Ti-based ceramics, where sometimes preparation control cannot be easily realized.

Along with the other ceramics used for dielectric applications, it is worth to mention the $BaO-R_2O_3-TiO_2$ family of materials, where R is a rare-earth species (Nd, La, Sm, Pr). This group of materials has large dielectric constants (typically 80-100), but moderate values of the Q-factor (only a few thousands) [7].

Currently, Ta- and Nb-based ceramic materials having the perovskite $Ba_3(B'B''_2)O_9$ (B' = Mg, Co, Ni or Zn, B'' = Ta or Nb) structure are employed in dielectric resonators. The dielectric materials with the composition $A^{2+}{}_3(B'B''_2)O_9$, where A^{2+} = Sr or Ba, B' = Mg, Sr, Ni, Co or Zn and B'' = Nb or Ta with two different cations on the B-sublattice have been known for many years [8,9] since the discovery by Galasso of the 1:2 ordering of B-site cations along the [111] direction of the parent cubic cell in the $Ba_3SrTa_2O_9$ system [10]. But it was not until the 1980's when it was realized that changes in the material structure as a result of 1:2 ordering drastically improve its microwave

properties [11,12]. Since then, it has been established that several factors, excluding the presence of long-range order, influence dielectric losses. Among them, the most significant factors are the formation of secondary phases, the presence of point defects, grain growth, and densification during the sintering process. The presence of several factors makes it difficult to establish an unambiguous correlation between structural changes and microwave properties. For example, in [13-15], the authors emphasize the importance of the 1:2 long range order on losses of $Ba_3(B'B''_2)O_9$ (B' = Zn, Mg or Co, B"= Nb or Ta) ceramics, while others, for example in [16], claim the importance of densification and grain growth for dielectric losses. Much research has been done on the influence of additives (like V_2O_5, WO_3, ZrO_2) on the microstructure, grain growth, defect chemistry, sinterability, and finally, microwave losses in perovskites [16-19]. The role of additives is either to introduce an ion with a different size and valency that promotes ordering through unit cell distortion, or to create conditions for liquid phase sintering. Davies *et al* [13] attributed the enhanced cation ordering in the $Ba(Zn_{1/3}Ta_{2/3})O_3$-$BaZrO_3$ system, in which $BaZrO_3$ was used as an additive, to the stabilization of the ordering-induced domain boundaries via the partial segregation of Zr cations. This thesis focuses on the influence of nonstoichiometry on the microwave losses in $Ba_3(BNb_2)O_9$ (B = Zn or Co) materials via modification in the densification process, formation of secondary phases, and changes in microstructure.

Deviation from stoichiometry results in structure destabilization and the appearance of secondary phases. The cubic perovskite structure is well known for its ability to accommodate a large degree of nonstoichiometry and vacancy formation on

cation and anion positions. Deviation from stoichiometry that results in B-site cation deficiency almost always improves microwave properties. The beneficial effect of cation deficiencies was observed in, for example, $Ba(Zn_{1/3}Ta_{2/3})O_3$ (BZT) [20], $Ba(Mg_{1/3}Ta_{2/3})O_3$ (BMT) [21] and $Ba(Mg_{1/3}Nb_{2/3})O_3$ (BMN) [22] perovskites. Desu and O'Bryan [23] observed ZnO loss in BZT perovskite and the simultaneous increase in the quality factor, and attributed it to the partial replacement of lost Zn with Ba ions from the A-site. Substitution of Ba with a larger ionic radius than that of the lost Zn causes unit cell distortion, facilitating the ordering process. Further evaporation of ZnO resulted in the appearance of zinc deficient secondary phases that did not degrade the quality factor. Contrary to the zinc tantalate system, formation of B-site cation vacancies due to the loss of ZnO and NiO, respectively, in $Ba(Zn_{1/3}Nb_{2/3})O_3$ (BZN) and $Ba(Ni_{1/3}Nb_{2/3})O_3$ (BNN) perovskites, resulted in a poor quality factor [24]. The decrease in Q was ascribed to the abrupt increase in the unit cell size and liquid phase formation that inhibited cation ordering.

Similar to the effect of B-site nonstoichiometry, conflicting literature data exists regarding the influence and its mechanisms of Ba-nonstoichiometry on microwave properties. While Lu and Tsai [21] observed an increase in cation ordering in Ba-deficient BMT due to an increase in the grain size and density because of liquid phase formation, Surendran *et al* [25] observed a similar behavior in the BMT system with small barium deficiencies, and did not find any evidence of liquid phase formation. BNN samples with an excess of barium oxide exhibited abnormal grain growth and poor

density [26], while in BMT perovskites with excess of BaO, uniform grains were observed [25].

Due to the lack in agreement on the influence of nonstoichiometry on Ba- and B-sites on the microwave quality factor in 1:2 perovskites, in our studies we correlated the change in the microwave quality factor with the densification influenced by the formation of secondary phases in $Ba_3(BNb_2)O_9$ (B = Zn or Co) perovskites. Deviation from stoichiometry results in the formation of Ba- and Nb-rich secondary phases with different symmetries. Depending on the structure, the role of those phases is either to introduce point defects facilitating B-site cation diffusion, or to enhance the densification process, decreasing available cation diffusion sites. Ceramic densification at the expense of decreasing inter-grain space results in the formation of voids because of the inability of air trapped inside of the material to escape during fast grain growth. While the relative density affects the quality factor of the studied ceramics, the loss value in pores or voids is higher than that of grains.

The ordering degree depends on the charge and/or size difference between cations on the B-sublattice. Conventionally, X-ray diffraction techniques (XRD) have been used to monitor changes in the superlattice splitting, as a result of ordering. For some materials like $Ba_3MgTa_2O_9$ and $Ba_3ZnTa_2O_9$ with large differences in B-site cation charge, the intensity of superlattice splitting is noticeable. However, for perovskites like $Ba_3CoNb_2O_9$ (BCN) and $Ba_3ZnNb_2O_9$ where ordering occurs on the scale of several nanometers, superstructure splitting is weak and X-ray techniques can be insensitive. The second goal of this thesis is to demonstrate the application of photoluminescence

spectroscopy to monitoring disorder-order phase transitions in the studied materials. Lowering in the symmetry from cubic to hexagonal as a result of 1:2 cation ordering removes degeneracy in molecular orbitals participating in the photoluminescence process, producing an additional luminescent band. The theory explaining photoluminescence as a result of ordering and the influence of the electronic structure of transition metal ions on the position of the photoluminescence band will be presented.

According to the literature data, in spite of the 1:2 ratio of B-site cations, $A^{2+}{}_3(B'B''_2)O_9$ perovskites can undergo so-called 1:1 ordering when B-cations arrange themselves in a 1:1 ratio along the [111] direction of the perovskite parent cubic cell [27]. Formation of the 1:1 ordered phase in the studied materials was found in the narrow range of nonstoichiometries. Another goal of the current research is to explain the formation of a "partial" 1:1 order in materials with 1:2 ratio of the B-site cations and to establish the influence of the 1:1 order on the microwave quality factor.

This work is organized as follows: Chapter 2 begins with the general introduction of the ideal ABO_3 perovskite structure. A brief review on the different cation substitutions, distortion mechanisms as well as factors influencing the stability of the perovskite structure is presented. A literature survey of the different types of cation order, with emphasis on the B-site order is given.

Chapter 3 introduces the concept of a dielectric resonator and presents a general review of dielectric materials for microwave applications with emphasis on the sources of microwave losses.

Chapter 4 reviews literature results on the application of Raman spectroscopy to the study of the ordering process in perovskite type materials. Two existing approaches used to analyze experimental spectra are described. This chapter also deals with the optical properties of the perovskite type materials. The origin of the emission signal in the perovskite structure as well as the influence of structural distortion on the optical properties of perovskite oxides is considered.

The theory of microstructure formation during the sintering process, including the influence of the initial preparation conditions and presence of impurities is given in Chapter 5.

The description of samples' preparation process and details of methods used to characterize perovskite materials are given in Chapter 6.

Chapters 7 through 9 present experimental results. At first, results of crystallographic analysis of nonstoichiometric perovskites, demonstrating formation of secondary phases are given in Chapter 7. Then, the influence of secondary phases and initial preparation conditions on the densification process and microstructure of ceramics is discussed in Chapter 8. Finally, changes in the optical and dielectric properties of nonstoichiometric perovskites as a result of secondary phase formation and variation in the densification process are discussed in Chapter 9.

Chapter 10 contains a summary and suggestions for future work.

Chapter 2

Perovskite Materials

2.1 Ideal perovskite structure

The name perovskite dates back to the beginning of the nineteenth century when a Russian mineralogist, L.A. Perovski, discovered a calcium titanium oxide mineral. Since then, oxides having a geometrical arrangement of atoms similar to that in $CaTiO_3$ are classified as perovskites.

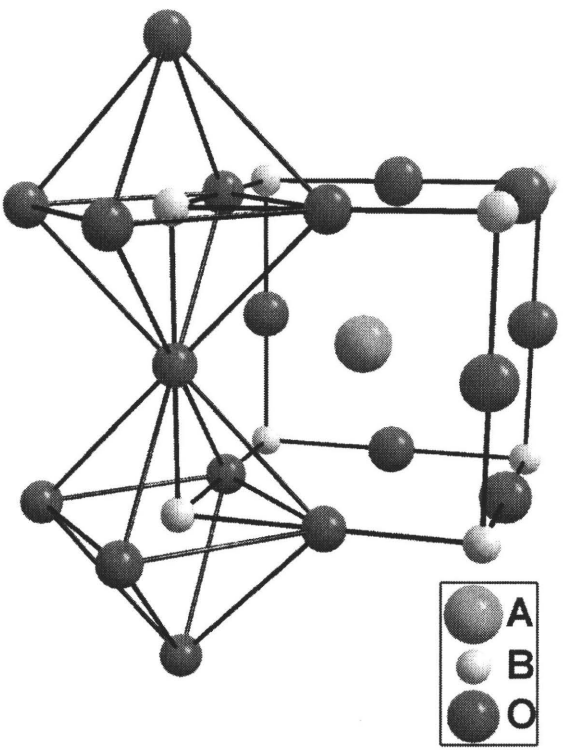

Figure 2.1: Ideal perovskite structure.

The ideal ABX_3 structure is cubic with the space group Pm-3m, where the A-site cations are typically larger than the B-site cations and the size of the X-site anions is similar to that of the A-site cation (Fig.2.1). The type of anion determines which cations occur in the perovskite structure. In the case of a monovalent anion (e.g. F, Cl, Br or I), structure diversity is limited to the monovalent A-site cation (e.g. Na or K) and divalent B-site cation (e.g. Mg, Ni or Cu). Incorporation of oxygen anions allows more flexibility in the structure composition: the sum of cation valences should be six. This can include, for example the following combinations of cations: La^{3+}+Fe^{3+}(3+3), K^{+}+Nb^{5+} (1+5) and □+Re^{6+} (0+6) (□- means cation vacancies) [28]. The last combination assumes the lack of the A-site cation.

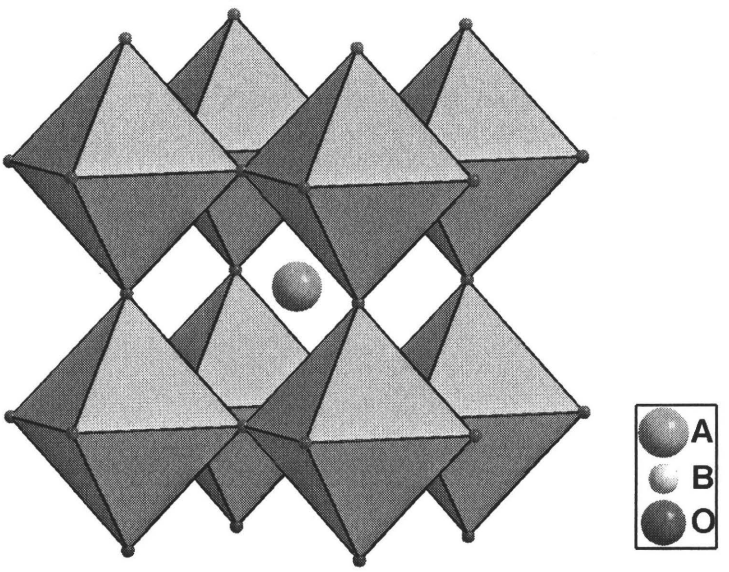

Figure 2.2 Linkage of BO_6 octahedra within an ideal ABO_3 structure.

Structurally ideal ABO_3 perovskite materials contain the linkage of corner sharing BO_6 octahedra formed by close packing of AO_3 layers (Fig.2.2). Alternatively, this

structure can be considered to have the B cation positioned in the center of the oxygen octahedra with A-site cations occupying the resulting spaces between BO_6 complexes. In this configuration, A-site cations are surrounded by twelve oxygens, while B-site cations have a 6-fold coordination with oxygen anions. The oxygen anions are coordinated by four A-site cations and two B-site cations.

2.2 Stability of the perovskite structure: tolerance factor

Goldschmidt did an initial study on different cation substitution in the 1920's [29]. During those studies, in the addition to the electro-neutrality principle, Goldschmidt considered geometrical sizes of constituent ions. By considering the perovskite structure as a set of touching spheres, each one having a radius equal to the ionic radius of the ion composing the structure, he came to the conclusion that the radii of ions are fundamental for the structure. The stability of the ideal cubic structure depends on the relative ionic sizes of the constituent ions. In order to have contact between atoms in the unit cell, $R_A + R_O$ should be equal to $\sqrt{2}(R_B + R_O)$, where R_A, R_B and R_O are the ionic radii of A- and B-site cations, and oxygen anions, respectively. As a characteristic parameter of stability of the cubic structure, Goldschmidt introduced the tolerance factor

$$t = \frac{R_A + R_O}{\sqrt{2}(R_B + R_O)} \tag{2.1}$$

This factor characterizes the geometrical compatibility of constituent ions [30]. Presently, all chemical elements of the periodic table with different electronic configurations

including first and second group elements, transition metals, and lanthanides have been substituted on cation sites in the ABO_3 structure to obtain new materials [28].

Only a limited number of materials produce an ideal perovskite structure with cubic symmetry. Stable cubic structures have been obtained for materials with the tolerance factor *t* ranging from 0.8 to 1.1 [28]. Even though the naturally occurring compound $CaTiO_3$ was initially accepted to have cubic symmetry and has been used as an example of an ideal cubic structure, it was later demonstrated that $CaTiO_3$ has orthorhombic symmetry [31]. $SrTiO_3$ with a tolerance factor t = 1.002 [28] is commonly regarded as the ideal cubic structure. In many perovskites, the bond lengths between cations and anions are geometrically incompatible (that is, the tolerance factor is significantly different from unity), and a lower symmetry structure can be stabilized. Structural deviations from the ideal cubic structure with orthorhombic, rhombohedral, tetragonal, monoclinic and triclinic symmetries are known [32,33]. In addition to the geometrical compatibility of ions composing the ABO_3 structure, there are a number of other factors influencing the stability of the ideal perovskite structure. For example, although $LaGaO_3$ has t = 0.9, at room temperature, this material adopts an orthorhombic structure [28]. Other factors that control stability and lead to distorted derivatives of the perovskite structure include first order Jahn-Teller distortion of BO_6 octahedra, second order Jahn-Teller effects that reflect mixing of molecular orbitals within A- and B-cation polyhedra, the degree of covalency, and metal-metal interactions. Changes in one of these parameters can produce structural modifications through the tilting or rotation of octahedra, formation of different B-O bond lengths, or off-center displacement of B-site

cations that results in suppression of one of the symmetry operations in the space group of the initial cubic structure. The mechanism of each of those distortions will be considered later in this chapter.

2.3 Nonstoichiometry in perovskites

Broad substitution possibilities lead to considerable freedom of ionic radii and ionic charges that can be introduced into the perovskite lattice. In addition to a broad range of cation substitutions, the perovskite structure is tolerant to anion and cation nonstoichiometries and substitution of several different cations on either A- or B-sites. Anion-deficient perovskites typically ranging from ABO_3 to $ABO_{2.5}$ have been found in the homologous series of $A_nB_nO_{3n-1}$ (N = 2,3,4, and 8) compounds, for example, $Ba_2In_2O_5$ [34], $La_4Ni_4O_{11}$ [35] and $Sr_8Fe_8O_{23}$ [36]. Perovskites containing excess oxygen are less common, likely because an introduction of interstitial oxygen in a close-packed perovskite structure is thermodynamically unfavorable. Oxygen excess in perovskite structures was found, for example, in the $LaMnO_{3+x}$ (x = 0.12) material [37]. Nonstoichiometry on cation sites could be more easily achieved in the case of A-site cation deficiency. This is explained by the fact that corner-sharing BO_6 octahedra form a stable network, and A-site ions can be partially missing. This was realized in the already mentioned ReO_3 structure with a completely vacant A-site, as well as, for example, the $Cu_{0.5}TaO_3$ perovskite [38] with partial occupation of the A-site. Ease of creation of A-site cation deficiencies because of the presence of a stable BO_6 corner-sharing octahedra network explains difficulties in the formation of vacancies on the B-site. The stability of

the corner sharing BO_6 network is based on the presence of a highly charged B-site ion with a small ionic radius, and B-B interactions between consecutive layers. The absence of the B-site cation results in hexagonal stacking of AO_3 layers that, according to Pauling's rules for the sharing of coordination polyhedra, is less favorable in ionic crystals. B-site cation deficiencies have been realized, for example, in $Ba_8(Ta_6Ni)O_{24}$ [39], where cation vacancies are ordered between two face-shared BO_6 layers.

2.4 Double cation substitution

After initial studies of single cation substitution on A- and B- positions in the ABO_3 structure done by Goldschmidt [29], the next step was to explore properties of perovskite materials with more than one ion on either A- and B- positions, or on both. In the 1950's, Roy's research group prepared a number of materials by substituting different atoms and groups of atoms on A- and B- positions [40]. The main principle during cation substitution was to maintain charge neutrality and geometrical compatibility of constituent ions. By starting with $BaTiO_3$ as the mostly studied material at the time because of its military applications, Roy's group replaced divalent Ba ions with monovalent and trivalent ions like K-La and K-Nd, giving $KLaTi_2O_6$ and $KNdTi_2O_6$ compounds that have the perovskite structure. Introduction of rare earth ions opens the possibility of varying the composition of the material in small steps. While La- and Nd-containing compositions exhibit perovskite structure, substitution of Sm yielded a structure with different symmetry. This was attributed to the small size of Sm^{3+} ions that resulted in structural distortion. Similar double substitutions were done on the B-site. For

example, replacement of Ti^{4+} ions with $1/3Co^{2+}+ 2/3Ta^{5+}$ in $Ba_3CoTa_2O_9$ was reported to crystallize in the perovskite structure. However, swapping Ba^{2+} with Pb^{2+}, having a similar ionic radius, fails to produce the perovskite structure. The significance of Roy's results is the indication that some other factors other than valences and ionic radii are responsible for the stabilization of the perovskite structure.

2.5 Cation ordering

The presence of several dissimilar ions on either A- or B- sites with different electronic structure and ionic radii can result in structural changes caused by the tendency of the structure to minimize energy through cation ordering. Order-disorder transitions in complex perovskites play a significant role in changing crystal structure, physical properties, and structural stability. Disorder-order phase transitions and alteration in the degree of order can produce significant changes in the dielectric and ferroelectric response, conductivity, or magnetic behavior [41]. An ordered system is generally stabilized when two neighboring cations occupying the same site differ significantly in valence, size, or coordination preferences. While there are literature reports on the A-site cation ordering, ordering of B-site cations is more common due to the increased covalent character of the -B-O-B- network.

According to literature data, the A-site ordering is mostly found in nonstoichiometric, oxygen-deficient perovskites. Ordering of the A-site cations has been correlated with the ordering of the anion vacancies that reduces the coordination of the A-site cation, enhancing the driving force for A-site cation diffusion. An illustrative

example of the A-site order is the $Ba_2YCu_3O_{7-x}$ material where the A-site is occupied by a 2:1 mixture of Ba and Y cations [41]. Ordering on the A-position in stoichiometric perovskites that does not involve the presence of anion vacancies is only found in systems where cations on the A-site have a large difference in valence and size, for example, in the $(Nd_{1/2}Ag_{1/2})TiO_3$ system [42]. The significance of the A-site order can be seen in the example of the work by Harada *et al* [43] who studied the A-site ordering in the $(La_{0.67-x}Li_{3x})TiO_3$ system and reported that changes in the unit cell volumes that resulted from ordering are responsible for the variation in the ionic conductivity of the material.

As in the case of the ordering on the A-position, B-site order can be achieved by changing coordination preferences of B-site cations through introduction of a high concentration of oxygen vacancies. The importance of B-site ordered perovskites is in their applications as dielectric and ferroelectric materials. So, the presence of significant concentrations of oxygen vacancies can be harmful for the final properties of a material. In this case, structural stability of the ordered phase is determined by the size and charge difference of B-site cations.

2.5.1 1:1 ordered perovskite structure

The most frequently encountered group of the ordered complex perovskites are those containing a 1:1 ratio of B-site cations with the general formula $A(B_{1/2}B'_{1/2})O_3$. The undistorted ideal 1:1 ordered perovskite represents a corner sharing arrangement of BO_6 octahedra in which different B-site cations are arranged in a 1:1 ratio along the [111]

direction of the perovskite unit cell (Fig. 2.3). The ideal 1:1 ordered perovskite is characterized by long-range cation order with no mixing of the B-site cations over the two available crystallographic sites. The resultant double perovskite structure, with the unit cell size twice as large as that of the size of the unit cell of the disordered structure, has Fm-3m symmetry. Doubling of the unit cell results in that the structural formula can be rewritten as $A_2BB'O_6$. In the ordered structure, there are two distinct B-cation sublattices (or alternatively, two different BO_6 complexes) that are occupied exclusively by B- and B'-cations, respectively. Disorder or random distribution of cations makes B-

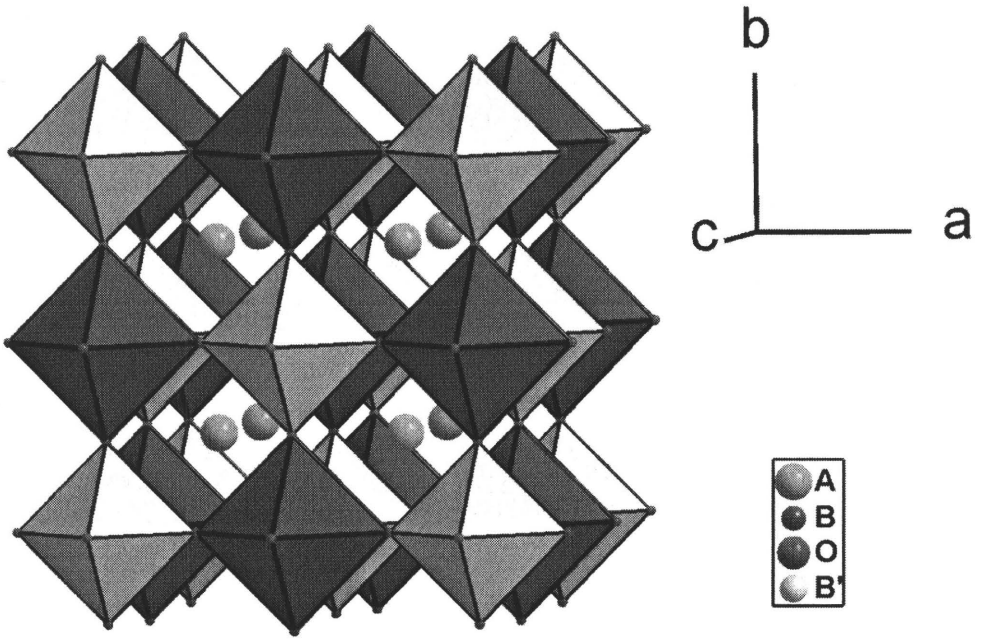

Figure 2.3 Ideal perovskite structure with 1:1 ordered B-site cations.

and B'-sublattices indistinguishable, thus changing the symmetry from Fm-3m to Pm-3m. The order maximizes separation of similar ions, enabling the intermediate

oxygen anions to more easily satisfy the different bond length requirements of the two dissimilar cations. This is achieved by an anion moving toward a smaller cation.

The first 1:1 ordered perovskite was described by Steward and Rooksby in 1951 for the mixture of alkaline earth elements with Mo^{6+} and W^{6+} as having a structure analogous to the previously studied $(NH_4)_3FeF_6$ system [44]. Later, Galasso performed an analysis of the available structural data, suggesting that the ordering degree depends on the charge and/or size difference of the B-site cations [45]. Since then there have been few systematic studies of the ordering in double perovskites, demonstrating that in addition to the previous conclusions, the degree of order depends on polarization properties of the B-site cations and preparation conditions [46-48]. Generally, higher annealing temperatures produce a greater ordering degree. Some exceptions were connected with the chemical stability of cations. For example, comparing Ba- and Pb-containing perovskites prepared under identical conditions, it was noticed that volatilization of Pb resulted in a decrease in the ordering degree when raising the preparation temperature. The material Ba_2ScBiO_6 also demonstrated the opposite trend with increasing temperature, which was attributed to the change in the oxidation state of Bi [49,50]. Woodward [49] indicated that for an undistorted double perovskite with Fm-3m symmetry, the degree of ordering does not significantly depend on the size of the A-site cation, but rather its chemical properties.

Perovskites containing Te, Sn, Sb or Bi are usually highly ordered because of the high polarizability of main group elements and resulting bonding character that produces shorter and stronger metal-oxygen bonds than in case of transition metal ions. High

ordering is attained because of the maximum anion polarization through the formation of asymmetrical, e.g. Te-O-B, bonds rather than symmetrical Te-O-Te ones.

In order to quantitatively evaluate the degree of ordering, Sleight [46] introduced the ordering parameter

$$S = 2X_B - 1 \tag{2.2}$$

where X_B- is the fraction of B-cations on the B-site. For complete order when all B-cations are on the B-position and B'-cations are on the B'-position, the ordering parameter S = 1. For complete disorder (X_B = 1/2), S = 0. Intermediate values of the ordering parameter when 1:1 ordering occurs only in some domains within grains composing the material have been reported. For example, Woodward, studying the Sr_2AlTaO_6 system with Fm-3m symmetry, reported the ordering parameter to be equal to 0.66. The ordering

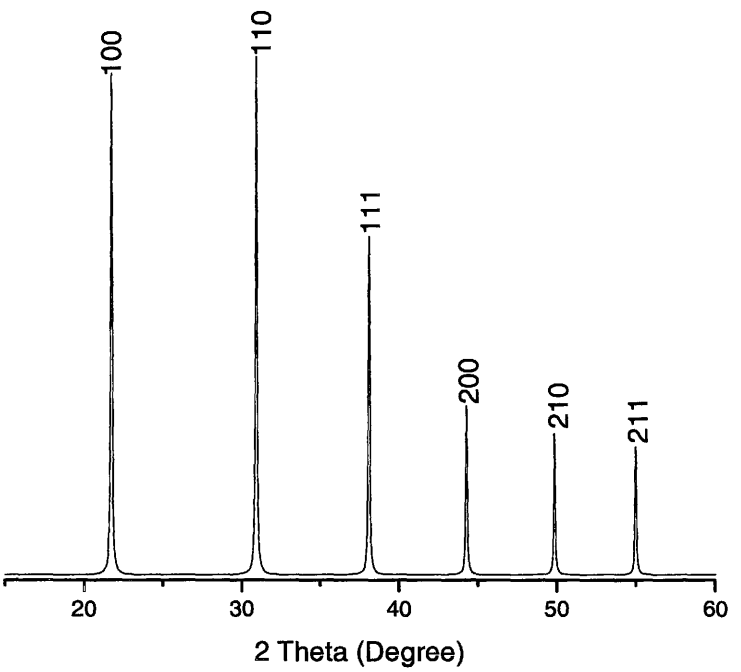

Figure 2.4 X-ray diffraction pattern of a completely disordered perovskite having the Pm-3m space group.

degree can be calculated from XRD patterns by comparing the intensities of the superlattice reflections originating from ordering to those that do not depend on ordering. For a completely disordered structure with Pm-3m symmetry, X-ray diffraction patterns are characterized by the appearance of strong and weak peaks without peak splitting and the formation of superstructure lines (Fig. 2.4).

1:1 order resulting in the Fm-3m space group produces reflections for which Miller indices h,k,l are either all odd or all even (Fig. 2.5). Intensities of the odd reflections depend on the ordering and can be used to estimate the S parameter. In particular, the ratio of intensities of the most intense I_{111} line originating from the 1:1 order to I_{220} that does not depend on the ordering is used to estimate the degree of the

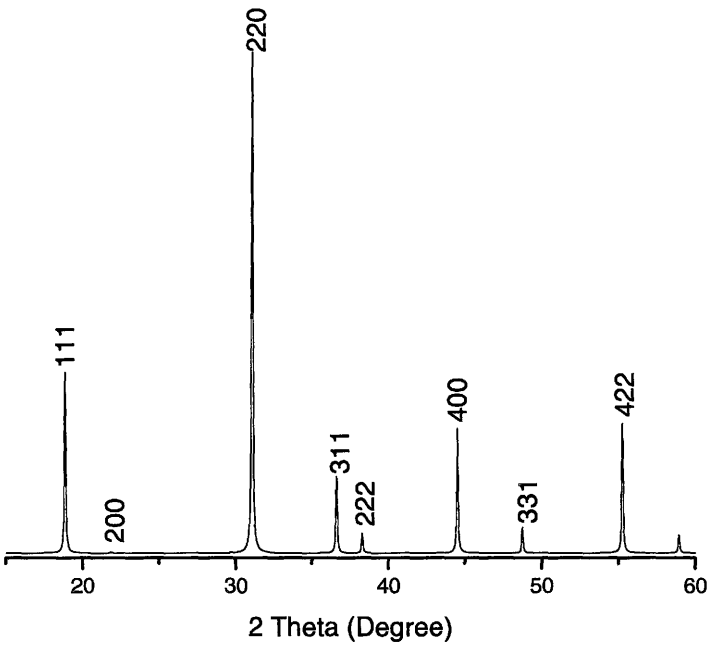

Figure 2.5 X-ray diffraction pattern of a 1:1 ordered perovskite with the Fm-3m space group.

long-range order. As already mentioned above, among other equal parameters, the ordering degree depends on the size and valence differences of the cations on the B-position. For divalent cations on the A-site, perovskites of the type of $A^{2+}{}_2B^{2+}B^{6+}O_6$ and $A^{2+}{}_2B^{1+}B^{7+}O_6$ show complete ordering while $A^{2+}{}_2B^{3+}B^{5+}O_6$ demonstrates various ordering degrees. Setter, studying 1:1 mixtures of the B-site cations [51] with double valence cations like Ca^{2+}, Ba^{2+} and Pb^{2+} on the A-site, found that in $Ca(Cr_{1/2}Nb_{1/2})O_3$ with |B'-Nb| = 0.03Å, no order exists, while increasing |B'-Nb| to 0.15 and 0.24Å, respectively in $Ca(In_{1/2}Nb_{1/2})O_3$ and $Ca(Er_{1/2}Nb_{1/2})O_3$ materials results in an increase in the ordering degree. Short range ordering existing in $A^{2+}{}_2B^{3+}B^{5+}O_6$ perovskites will likely be undetectable by XRD diffraction technique, but can be resolved by, for example, electron diffraction (e.g. SrLaMnRuO6 [52]).

2.5.2 1:2 ordered perovskite structure

The existence of 1:2 and 1:3 mixtures of cations on the B-site sublattice has been reported to produce 1:2 and 1:3 ordering, respectively [8,9,53-58]. 1:2 ordered structures are more interesting because of their practical applications as dielectric resonators. There is small number of literature reports on the formation of the 1:2 ordered structure in perovskites with mono- and trivalent cations on the A-site. The existence of unstable short-range ordering in $A^{1+}(B^{3+}{}_{1/3}B^{6+}{}_{2/3})O_3$ with a monovalent cation on the A-position was observed in tungsten systems, like $Na(Al^{3+}{}_{1/3}W^{6+}{}_{2/3})O_3$ [59]. The limited stability of this family of perovskites was attributed to local imbalances in anion bond valences. The presence of two dissimilar cations on the B-site creates two types of BO_6 octahedra with

different anion environments. The highly charged W^{6+} cation significantly distorts the anion network by overbonding the neighboring oxygen ions and leaving the rest of the anions underbonded. The formation of the 1:2 ordered perovskite structure with a trivalent cation on the A-sublattice was explored in the Ti^{4+} ($A^{3+}(B^{1+}_{1/3}B^{4+}_{2/3})O_3$) group of perovskites and was attributed to the tendency of Ti^{4+} to adopt a stable off-center octahedral coordination [60]. The largest number of 1:2 ordered structures was observed in the family of perovskite type materials containing 1:2 mixtures of B-site cations with a divalent cation on the A-site. Formation of 1:2 ordering was observed in $A^{2+}(B^{2+}_{1/3}B^{5+}_{2/3})O_3$ (A^{2+} = Ca, Sr and Ba, B^{2+} = Mg, Ca, Sr, Mn, Co, Ni and Zn, B^{5+} = Nb and Ta) materials [8,9].

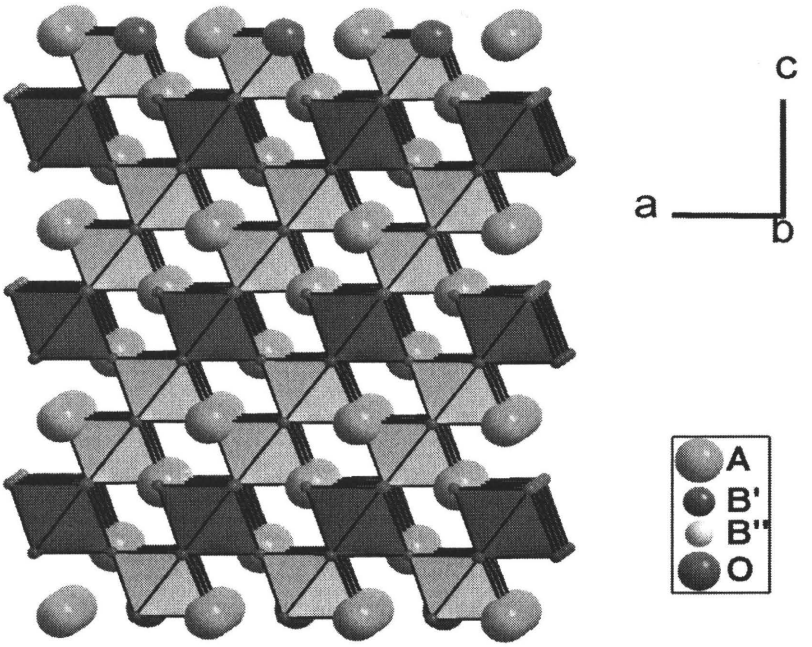

Figure 2.6 Structure of an ideal 1:2 ordered perovskite showing layers of $B'O_6$ octahedra separated by a double layer of $B''O_6$ octahedra.

The first 1:2 ordered structure was observed by Galasso in the $Ba_3SrTa_2O_9$ perovskite [10]. The ideal untilted 1:2 double perovskite structure is formed by ordering of B-site cations in a –B'-B"-B"-B'- sequence along the [111] direction of the perovskite parent cubic cell (Fig.2.6). Electrostatic repulsion between two small, highly charged B" (e.g. Nb^{5+} and Ta^{5+}) cations in neighboring cells creates crystallographic distortion, elongating the original cell along the [111] direction. Rhombohedral distortion lowers the symmetry of the system from cubic, with the space group Pm-3m, to hexagonal, with the P-3m1 space group. In the undistorted structure, the *c* axis of the hexagonal cell is equal to $\sqrt{3}*a$, where *a* is the size of the cubic perovskite cell. Long range 1:2 ordering, as in the case of 1:1 ordered perovskites, depends on the size and charge difference of B-site

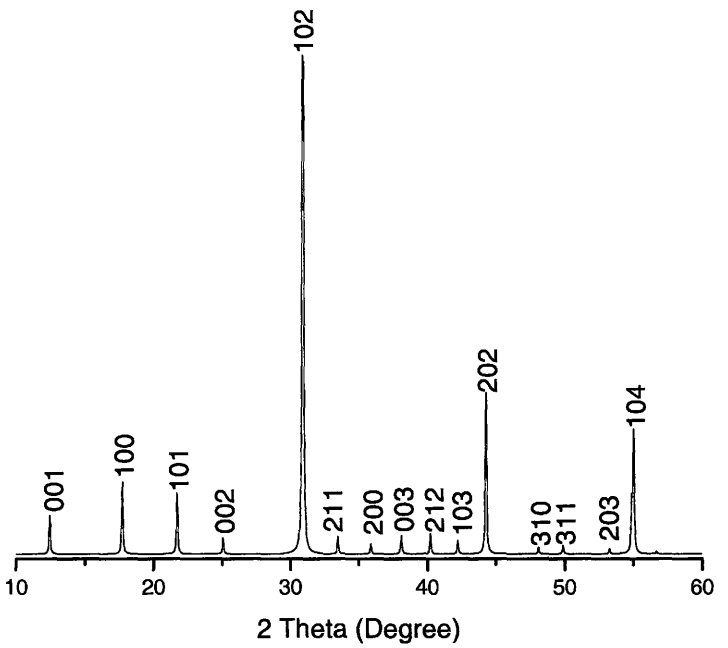

Figure 2.7 X-ray diffraction pattern of a 1:2 ordered perovskite demonstrating the appearance of additional lines at low diffraction angles.

ions constituting the material increases *c/a* ratio ($c/a > \sqrt{3}$) [61,62]. In X-ray diffraction spectra, deviation of the *c/a* lattice parameter from $\sqrt{3}$ produces the splitting of peaks and the appearance of extra lines at $2\theta < 40°$ (Fig.2.7).

Extensive research on perovskites containing a double valence cation on the A-site and a 1:2 mixture of B-site cations demonstrated that not all materials actually produce a 1:2 ordered structure. For example, the formation of a 1:1 ordered structure was observed in $Ba_3WSm_2O_9$ [63], $Ba_3UFe_2O_9$ [64], and $Sr_3WB'_2O_9$ (B' = Cr, Fe) [65] materials in spite of the different cation ratios. Lufaso [66] emphasized the importance of transition metal cations with empty *d*-shell orbitals on the B-site to stabilize the 1:2 ordered structure. In particular, substitution of Nb^{5+} or Ta^{5+} for isovalent Sb^{5+} with a similar ionic radius (0.74Å for Sb^{5+} versus 0.78Å for Nb^{5+} and Ta^{5+}) in double perovskites with barium on the A-site results in the formation of a structure different from a double perovskite (e.g., $Ba_3BSb_2O_9$ (B = Mg, Ni), as it crystallizes in the $P6_3/mmc$ space group [67]). Formation of structures with space groups different from P-3m1 has been attributed to the different stabilization power of the cation-anion network to off-center displacement of the B-site cation. As in the case of the disordered cubic structure where charge compensation is achieved only on average within several unit cells, the charge and size imbalance caused by the presence of two dissimilar B-site cations with different size and charge is accommodated by the long-range displacement of oxygen anions toward smaller, more highly charged B cations (usually B"). As a result, the anion layer lying between two B" cations with higher charge becomes overbonded while leaving oxygen ions in the –B'-O-B"- chain underbonded (Fig.2.6). Collective

displacement of B" cations toward the face of their octahedron (that is, out of center) can optimize the anion coordination environment. The result of the out of center distortion is the formation of three longer B"-O-B" and three shorter B"-O-B' bonds. The ability of the B" cation to stabilize an out of center distortion depends on the presence of available empty *d*-orbitals that are able to mix with oxygen *2p* orbitals. This explains the formation of the 1:1 ordered structure in, for example, $A_3TeCo_2O_9$ (A = Ba or Sr) [68] and $Ba_3B'B"_2O_9$ (B' = Mo, W, B" = Dy, Gd) [63] materials with B-site cations containing partially filled *d*-orbitals, as well as the crystallization of $Ba_3BSb_2O_9$ (B = Mg, Ni) with Sb^{5+}, which does not have an empty *d*-orbital (Sb^{5+}:$Kr4d^{10}$), in the $P6_3/mmc$ space group [67].

The above discussion demonstrates that structural parameters of cations composing a material are not the only factors influencing the strength of the double perovskite structure. B-site cation-anion interactions involving orbital mixing are crucial for structure stabilization. Another important aspect that has not been considered yet is the influence of chemistry of the A-site cation on 1:2 order. The presence of Sr^{2+} and Ba^{2+} cations with ionic radii of 1.54 and 1.74Å, respectively, on the A-site produces the 1:2 ordered double perovskite structure [45]. Substitution of Pb^{2+} on the A-site with an atom with an intermediate ionic radius (R_i = 1.63Å) was reported to produce 1:1 ordering in $Pb(B^{2+}_{1/3}B^{5+}_{2/3})O_3$ (B^{2+} = Mg, Zn, B^{5+} = Ta, Nb) perovskites [69-73]. The formation of a 1:1 ordered structure in lead perovskites with a 1:2 mixture of B-site cations was explained by the difference in the electronic structure between Pb^{2+} and alkali earth metals. The reason that a 1:1 ordered structure rather than a 1:2 ordered one is formed

was attributed to the change in the electron density of oxygen anions caused by the presence of a smaller B-site cation. The distorted anion network interacts with a $6s^2$ lone pair of the Pb^{2+} stabilizing 1:1 ordered structure [74].

2.5.3 "Random-site" vs. "Space-charge" models

The formation of a 1:1 ordered structure in materials containing a 1:2 mixture of cations on the B-sublattice demonstrates, on the one hand, the stability of 1:1 ordering to large nonstoichiometries on the B-site that is to a large deviation from the 1:2 ratio of B-cations. On the other hand, it brings up the question on how the structure can accommodate such a large excess of cations. According to literature data [*e.g.*75], formation of 1:1 order in the $A(B'_{1/3}B''_{2/3})O_3$ structure can be described by either the so-called "random-site" model or the "space-charge" model.

First, the "random-site" model considers that one of the two B-sites in the $A_2(B'B'')O_6$ structure is occupied exclusively by a B" cation, and the second B-site is occupied by a random mixture of B' and the remaining B" cations. In this model, the ordered 1:1 structure can be represented as $A[(B'_{2/3}B''_{1/3})_{0.5}B''_{0.5}]O_3$. In this case, the average composition of the ordered regions is the same as that in the bulk, and charge compensation is achieved within several unit cells. The formation of a homogeneous structure without charge imbalance would be expected to promote growth of ordered domains during heat treatments. The formation of a 1:1 ordered structure in $Sr_3CoSb_2O_9$ perovskite was described by the "random-site" model [75]: one of the B-sites is solely occupied by Sb, while the second B-site contains a random distribution of 1/3Sb+2/3Co.

In the second case, the "space-charge" model, a stoichiometric 1:1 mixture of B' and B" type cations occupy the B-site in the $A_2(B'B")O_6$ structure while the rest of the B" ions, in order to preserve $A(B'_{1/3}B"_{2/3})O_3$ stoichiometry, form regions rich in B"-cations. This model is characterized by the formation of ordered domains with a deficiency of B"-type cations and nearby regions that have excess of B"-type cations with respect to the average $A(B'_{1/3}B"_{2/3})O_3$ composition. Cation imbalance creates a net negative charge within ordered domains and a net positive charge in B"-rich regions. The presence of a strong electric field inside of the material results in that the ordered domain size cannot be changed by heat treatments. In the case of small ordered domains, charge compensation can be achieved by the surrounding B"-rich material [27]. However, for large domain sizes, the charge imbalance inside of the 1:1 ordered structure can be compensated through the creation of point defects (oxygen vacancies in the 1:1 ordered domains and cation vacancies in the surrounding regions) or through donor doping of the ordered structure. The formation of 1:1 order in the $Pb(B^{2+}_{1/3}B^{5+}_{2/3})O_3$ (B^{2+} = Mg, Zn, B^{5+} = Ta, Nb) family of materials has often been ascribed to the "space-charge" model because of the small size of the ordered regions (on the order of several nanometers) and their resistance to heat treatments [*e.g.* 27]. Studying the La-doped $Pb_{1-x}La_x(Mg_{(1+x)/3}Nb_{(2-x)/3})O_3$ system, Chen *et al* observed almost a two order increase in the size of the ordered domains (from 10-20nm to about 1μm) with an increase in the concentration of trivalent La that was attributed to the internal charge compensation [69].

2.5.4 Coexistence of 1:2 and 1:1 order

The previous sections demonstrated that the $A^{2+}(B^{2+}_{1/3}B^{5+}_{2/3})O_3$ (A^{2+} = Ca, Sr and Ba, B^{2+} = Mg, Ca, Sr, Mn, Co, Ni and Zn, B^{5+} = Nb and Ta) family is the main group of materials with a 1:2 B-site cation ratio that adopts a 1:2 ordered structure. Structural stabilization is achieved through the presence of small, highly charged cations and through the collective movement of an anion network in order to optimize its coordination environment. The stability of 1:2 order in the Nb^{5+}/Ta^{5+} family of perovskites has been explored by introducing different levels of dopants. It has been shown that the symmetry of ordering in this group of perovskites can be changed by low-level substitutions of cations on either A- or B-sites [76,77]. The first case was realized in, for example, the $Ba(Zn_{1/3}Nb_{2/3})O_3$-$La(Zn_{1/3}Nb_{2/3})O_3$ system, where the double valence barium cations were gradually replaced by trivalent lanthanum cations [78]. The authors demonstrated that a La-substituted 1:2 ordered $Ba(Zn_{1/3}Nb_{2/3})O_3$ perovskite has a limited range of stability: by increasing the lanthanum concentration above 5%, 1:2 order destabilizes in favor of 1:1 order. The limited stability range was attributed to changes in the geometrical arrangements of ions composing the structure. In order to preserve electrical neutrality for low levels of La^{3+} concentrations, the Zn^{2+} concentration should increase above the 1:2 ratio (as opposed to the stoichiometric $Ba(Zn_{1/3}Nb_{2/3})O_3$ perovskite). The presence of a higher concentration of zinc cations on the B'-sublattice with larger (in comparison to niobium) ionic radius (R_{Zn} = 0.72Å vs. R_{Nb} = 0.64 Å) destabilizes the 1:2 order, and at the same time shifts the Zn:Nb concentration closer to

the 1:1 ratio. An increase in the amount of Zn cations on the B'-site makes a difference in the charge and size of B'- and B"-cations larger stabilizing 1:1 order.

Similar behavior was observed in the mixture of $Ba(Zn_{1/3}Ta_{2/3})O_3$ and $BaZrO_3$ materials [13, 79-81], where Zr^{4+} cations were introduced on the B-site. Changes in the ordering behavior were related to changes in the material's microstructure and the kinetics of the sintering process. Initial X-ray diffraction measurements demonstrated that insertion of small levels of zirconium cations destroys 1:2 long-range order, promoting short-range 1:2 order [80]. By increasing the Zr^{4+} concentration above 3%, 1:2 ordered domains disappear giving rise to 1:1 ordered nanostructures described by the "random-site" model. The choice of this model was based on prolonged heat treatments of samples during which the intensities of X-ray diffraction peaks originating from the 1:1 ordered structure increased, indicating the formation of 1:1 long-range order. According to the "random-site" model, the B"-site is occupied by only Ta^{5+} cations while the B'-site is shared by Zn^{2+}, Zr^{4+} and the remaining Ta^{5+} cations. In this case, the structural formula can be represented as $Ba\{[Zn_{(2-y)/3}Ta_{(1-2y)/3}Zr_y]_{1/2}[Ta]_{1/2}\}O_3$. According to this representation of the 1:1 ordered structure, the current model is valid for up to 25% of $BaZrO_3$ substitution. One of the explanations of the limited stability of 1:2 long-range order was the formation of different equilibrium cation-anion bond lengths with introduction of zirconium. Different Ta-O and Zr-O bond lengths disrupt long-range 1:2 order. 1:1 order is an energetic compromise in which long-range order of tantalum is preserved in only one layer.

2.6 Structural distortion

Summarizing the previous discussions, one can say that there are a limited number of perovskite materials having ideal cubic structure. Most of the compounds in the perovskite family are distorted to produce different coordination environments for cations. Kunz and Brown [82] distinguished four types of distortions: the influence of a bond network, cation-cation repulsion, lattice stresses, and electronic distortion. According to the principle of maximum symmetry that states that all atoms and bonds should be chemically equivalent, the most stable bonding network is formed when the coordination sphere has bonds with the same bond valence, or alternatively, the same bond length. Bond valence is equal to the amount of the atomic valence contributed by each of the atoms participating in bonding. Variation in the coordination environment of one of the ions induces changes in neighboring ions through the bond network. Cation-cation repulsion is critical for materials in which two octahedra share edges or faces. In this case, the structure tries to relax by increasing the cation-cation distance. Lattice stresses appear in materials when the sizes of constituting ions do not match an ideal space for this structure. The presence of electronic distortion is caused by lowering of the energy of the empty *d* orbitals of the transition metal cations and their interaction with anion orbitals. In this case degeneracy of *d* orbitals can be removed by the out of center distortion.

2.6.1 Rotation of oxygen octahedra

Section 2.1.2 introduced the idea of the tolerance factor that shows the fitting of ions in the considered structure. For a tolerance factor of less than 0.8, indicating the presence of undersized A-cations in the cavity formed by BO_6 octahedra, rotation of BO_6 complexes occurs [83,84]. In general, this rotation does not disrupt the corner-sharing connectivity of the BO_6 network, rather, it creates a different A-O bond length. The materials $A(B'_{1/3}B''_{2/3})O_3$ (A = Ba, B' = Mg, Co or Zn, B'' = Nb, Ta) considered in the

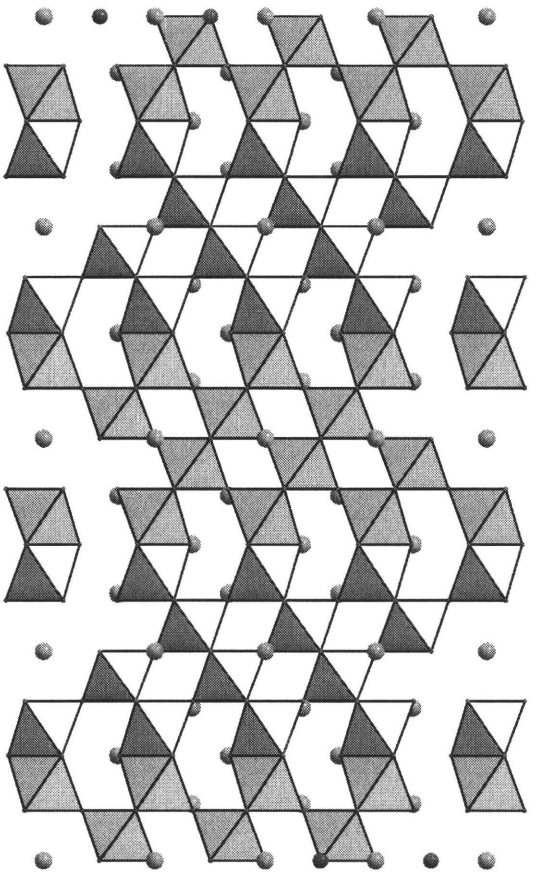

Figure 2.8 Formation of a mixed corner sharing and face sharing BO_6 network.

present research have tolerance factors t > 1 (t = 1.3÷1.35) [e.g. 85], demonstrating that A-O bonds are compressed while B-O bonds are stretched. Placement of the B-site cations in an oversized cavity opens up the possibility of cation "rattling" and out of center displacement. By decreasing the ionic radius of the B-site cations even further (or alternatively increasing the size of the A-site cations), the corner-sharing arrangement of BO_6 octahedra is disrupted in favor of a mixed corner sharing and face sharing BO_6 network (Fig.2.8). The stability of the face sharing structure, as already mentioned, depends on the compensation of the electrostatic repulsion between small, highly charged cations occupying neighboring positions, and can be achieved by the introduction of cations with smaller formal charges or through the formation of vacancies on B-sites [59]. The presence of an ordered arrangement of cation vacancies can locally relax the structure through collective atomic displacement.

Zhang *et al* [86] studying about 232 entries from the Inorganic Crystal Structure Database [87] that crystallize in the perovskite structure came to the conclusion that a stable perovskite is formed when the tolerance factor does not exceed 1.06. Another important result of their research is the conclusion that steric distortion caused by an inconsistency in size of ions is compensated by the formation of an anisotropic environment around transition metal cations.

2.6.2 Out of center distortion

Octahedral complexes containing d^0 transition metal ions are often found in a distorted environment. Distortion occurs due to the out of center movement of a d^0 cation

and results in the formation of unequal B-O bonds. The amount of distortion increases with increasing of formal charge and decreasing size of the cation [82]. For example, for small and highly charged cations like V^{5+}, Mo^{6+}, and W^{6+}, the distortion is large, and for lower charge, large cations like Zr^{4+} and Hf^{4+}, the expected distortion is small. The considered NbO_6 and TaO_6 octahedral complexes with Nb^{5+}/Ta^{5+} cations will have an intermediate amount of distortion with a slightly smaller value for heavier Ta^{5+} cations. The amount of distortion (the so-called octahedral distortion parameter) or out of center displacement of a transition metal cation is determined by the following formula [66]:

$$\Delta d = \frac{1}{6}\left[\sum_{n=1,6} \frac{[d_n - \langle d \rangle]}{\langle d \rangle}\right]^2 \tag{2.3}$$

where $\langle d \rangle$ is the average B-O distance and d_n is the actual B-O bond distance.

Evidence for out of center distortion in the Nb^{5+}/Ta^{5+} family of perovskites with Ba^{2+} on the A-site was first found by Jacobson *et al* [88] in BZT perovskite. They observed B-O bond lengths different from those that should be expected from the sum of the ionic radii. In particular, considering –B'-O-B"- bonds where B' = Zn^{2+} and B" = Ta^{5+}, the observed bond lengths were 1.98Å and 2.14Å (versus 2.09Å and 1.99Å that should be expected from the sum of the ionic radii), respectively, for Zn-O and Ta-O bonds. The authors attributed the unexpected change in the bond lengths to the increased covalence of the Zn-O bond caused by double electron donation between O^{2-} and Zn^{2+}: *3d* electrons are transferred to the modified by Ta^{5+} oxygen orbitals, and are then back donated to the *sp* orbitals of zinc. The decreased contribution to the lattice energy caused by elongation of the Ta-O bond is compensated by out of center movement of the tantalum cation.

Experimental evidence confirmed by theoretical simulations of the out of center distortion of a d^0 cation within the Nb^{5+}/Ta^{5+} family of 1:2 ordered perovskites was found by Lufaso [66]. Studying completely ordered $Ba_3B'B''O_9$ (B' = Mg, Ni, Zn, B'' = Nb, Ta), Lufaso found that octahedral complexes around niobium cations are more distorted than their tantalum analogues, indicating that the Nb-O bond is more covalent than the Ta-O bond. Among niobium and tantalum perovskites, the degree of distortion also changes: the value of the octahedral distortion parameter decreases in Mg-containing perovskites toward Ni-perovskites, with Zn-containing materials occupying an intermediate value of distortion. However, the author did not discuss the influence and role of the B' cation on structural distortion, but this could be possibly connected to differences in electronegativities of B'-site cations and different electronic configurations. Mg^{2+} and Zn^{2+} upper orbitals are filled while Ni^{2+} has partially filled *d*-orbitals. The chemistry of transition metal ions with partially filled *d*-orbitals and especially those with an unpaired number of electrons will be considered in the chapter describing optical properties of transition metals in an octahedral environment. The presence of different cations on the B'-site with different electronic configurations and electronegativities produces different B'-O bonds that influence the stability of the B''-O bond through the bond network.

2.7 Physical properties of perovskite type materials

As concluding remarks of the present chapter, it is worth mentioning the different physical properties that result from a broad range of cation substitutions and the structural changes accompanying them. Different physical properties of perovskite materials are

related to the complex character that metal ions display in certain configurations with an oxygen environment.

The presence of unpaired valence electrons is responsible for the change in the conductive properties from superconductive to semiconductive and dielectric. Superconductive properties have been realized in, for example, cuprites [89]. Semiconducting properties were discovered in perovskites where the oxidation state of the B-site cation is lower than its most stable one (e.g. $CaMoO_3$, $SrMoO_3$, $LaTiO_3$, $LaVO_3$) or in perovskites allowing the B-site cation with two valence states *(e.g.* $La_{1-x}Sr_xMnO_3$, $SrTiO_{3-x}$, $SrVO_{3-x}$, $Ba_{1-x}La_xTiO_3$) [45]. An out of center displacement of Ti^{4+} found in $BaTiO_3$ perovskites is responsible for ferroelectric properties [45].

The introduction of several cations on the B-site and the accompanying ordering processes produces new physical properties. The magnetic properties of oxides are attributed to the presence of unpaired electrons in transition metal ions and the presence of B-O-B bonds. In an ideal cubic structure, the B-O-B bond angle is close to 180 degrees favoring the superexchange interaction mediated by oxygen ions. Although the superexchange interaction results in an antiparallel alignment of magnetic moments, the introduction of a second ion on the B-site can result in the net parallel coupling of nearest magnetic moments. Ferromagnetism was found in a number of materials with the formula $A_2B'B''O_6$ with two different cations on the B-sublattice [90,91]. In this case, an effective coupling between nearest magnetic moments is achieved through the 1:1 ordering of B-site cations. The formation of 1:1 ordered nanodomains in lead double perovskites (e.g. $PbMg_{1/3}Nb_{2/3}O_3$) is responsible for their dielectric properties [92]. This group of materials

possessing exceptionally high dielectric constants has high losses at microwave frequencies that limited their application at lower frequencies. Excellent dielectric properties were found in 1:1 [93-96] and 1:2 [*e.g.* 11-14] ordered perovskites with barium and strontium on the A-site. Having moderate values of the dielectric constant, this group of materials demonstrates exceptionally low losses in the microwave range, enabling their application as dielectric materials in microwave oscillators.

Chapter 3

Dielectrics for Microwave Applications

3.1 Dielectric resonators

Transition from the radio to the microwave frequency range enabled by the progress in material science especially in semiconductor technology and subsequent development of miniature microwave sources triggered the search for new dielectric materials. In addition to being very cost effective, dielectric materials applied in devices operating in the microwave range results in miniaturization of main components. The concept of the dielectric resonator was first introduced by Richtmyer in 1939 when he theoretically demonstrated that a dielectric object without metallic coating can function as a resonator [97]. The physics of dielectric resonators is based on the Maxwell theory of wave-matter interaction: the wavelength of an electromagnetic wave (λ_0) entering a nonmagnetic medium with dielectric constant ε decreases as

$$\lambda = \frac{\lambda_0}{\sqrt{\varepsilon}} \tag{3.1}$$

Application of dielectric materials with high dielectric permittivity forced out bulky waveguide systems in applications that did not require high power transmission.

Dielectric resonators can be used as radiating elements, resonating components, or feedback elements, and are commonly found in Global Positioning System (GPS) devices, mobile communication systems, automobile collision avoidance sensors, TV receivers, military radar systems and others [98-102].

Today, dielectric resonators are found in systems operating in the 1-30 GHz frequency range [99]. In order to cover such a wide frequency range, different dielectric materials should be used.

3.2 Requirements for a dielectric resonator

Applicability of a particular dielectric material in a required frequency range depends mostly on the following factors:

a) High quality factor in order to minimize losses of electromagnetic energy and decrease product size through reduction in power consumption.

b) Small and adjustable temperature coefficient of resonance frequency (τ_f) that prevents frequency drift caused by varying temperature. Usually, the required τ_f values are from –5ppm/K to 5ppm/K.

c) High dielectric permittivity to minimize the size of components of a microwave device.

The above mentioned parameters are interconnected with each other and tuning of one of them requires optimization of the others.

3.2.1 Quality factor

Miniaturization of electronic devices in addition to reducing the size of each component used, requires reduction in consumption power caused mainly by losses in the device's components. The quality factor of resonant cavity depends on the losses in the

walls of the resonator and the inside of the material filling the resonator's cavity. The total losses of the system are defined as

$$\frac{1}{Q} = \frac{1}{Q_d} + \frac{1}{Q_m} \tag{3.2}$$

where $1/Q_d$ is the loss in the dielectric material and $1/Q_m$ is the loss in the resonator's walls. Application of a metal resonant cavity filled with a dielectric material is limited to low frequencies (1-2GHz). In this frequency region, resonators can be realized as either microstrip lines or coaxial transmission lines made from ceramic tubes covered with metal. By increasing the operating frequency of the system, conduction losses inside of the metal walls and electrodes become significant, restricting the component's quality factor. For operating frequencies exceeding 5GHz, dielectric resonators representing a monolithic piece of dielectric material should be used. Absence of metallic parts limits the quality factor of the component by losses in dielectric material. The significant aspect of dielectric materials operating at high frequencies is the frequency dependence of losses (or alternatively the quality factor): an increase in operating frequency is accompanied by an increase in losses (reduction in the quality factor).

3.2.2 Temperature coefficient of the resonance frequency

The usual operating range of microwave devices is from –20C to 80C. In order to achieve frequency stability, the temperature coefficient of resonance frequency defined as

$$\tau_f = \frac{1}{f_0}\frac{\Delta f_0}{\Delta T} \tag{3.3}$$

should be close to zero. The resonance frequency of the oscillator depends on the size and dielectric permittivity of the dielectric material. So, the value of τ_f depends on the temperature coefficient of the dielectric constant (τ_ε) and the linear thermal expansion coefficient of the dielectric material (α):

$$\tau_f = -\alpha - \frac{1}{2}\tau_\varepsilon \tag{3.4}$$

For ionic materials, the value of α usually falls in the range 8-15ppm/K limiting τ_ε values to $\tau_\varepsilon = -2\alpha \approx -30ppm/K$.

There are a limited number of materials having appropriate values of the temperature coefficient of the dielectric constant. Several methods to obtain temperature stable materials are presently used: preparation of a composition consisting of several phases with opposite signs of τ_ε [103-106]; preparation of a layered composition with each layer having opposite sign values of the temperature coefficient of the dielectric constant [107]; through aliovalent substitutions [108, 109].

Several attempts to correlate the temperature coefficient of the dielectric constant with dielectric permittivity and the tolerance factor have been made. Colla *et al* [110] and Steiner *et al* [111], both studying perovskite materials, showed that tilting of the oxygen octahedra is responsible for the behavior of τ_ε. Later, Reaney showed a relationship between the temperature coefficient of the dielectric constant and the tolerance factor, describing the stability of the perovskite structure [85]. Wersing correlated values of the temperature coefficient of the dielectric constant with the dielectric permittivity [1].

3.2.3 Dielectric constant and classification of dielectric resonators

The choice of the operating frequency and the restrictions on the size of the final components define the required dielectric constant of the material employed. At low frequencies (the lower limit of the microwave region that usually ranges from 0.3 to 4 GHz) the quality factor is not an issue and two of the limiting factors are the value and temperature stability of the dielectric constant. In order to obtain small-size components for low frequency applications, dielectric materials with a large dielectric constant (on the order of 80-100) have to be used. The previously mentioned $BaO\text{-}R_2O_3\text{-}TiO_2$ (R = Sm, Nd, La) system [103, 104, 112] has a relatively high dielectric constant. Temperature stabilization of this ceramic family can be achieved by mixing different ratios of BaO, R_2O_3 and TiO_2 oxides. Resonators based on high ε dielectric materials can be found in cellular and personal communication systems [99, 101].

The increase in the operating frequency above several GHz is accompanied by a significant increase in losses. In the 1-100 GHz frequency range, dielectric polarizability without strong energy absorption can be obtained through optical and infrared polarizations. The impact of optical polarization on the total value of polarizability for most materials is usually small. So, materials having high infrared polarizabilities that result from cation and anion displacement caused by an applied electrical field should be used to obtain temperature stable dielectrics with moderate dielectric constant and low losses. Infrared polarization mechanisms can only be realized in ionic crystals [113]. In the 5-15GHz range, materials with dielectric constant of $\varepsilon \approx 40$ are used. $(Zr,Sn)TiO_4$, $BaTi_4O_9$, $Ba_2Ti_9O_{20}$ [4-6, 114, 115] are mostly used in the aforementioned frequency

range. For frequencies falling in the 15-30GHz range, materials with ultra-low losses and dielectric permittivities in 20-30 range are employed. The Ba-based family of 1:2 and 1:1 ordered perovskites belong to this class of materials with low dielectric permittivities.

3.3 Current materials with ultra-low losses for microwave dielectrics

Presently $Ba(B'_{1/3}B''_{2/3})O_3$ (B' = Mg, Ni, Co, Zn, B'' = Nb, Ta) ceramics compose a class of dielectric materials having ultra low losses and ε = 20-40 suitable for dielectric resonator applications.

The first excellent microwave properties of this family of materials were reported by Kawashima *et al* [11]. Studying $Ba(Zn_{1/3}Ta_{2/3})O_3$ ceramics they reported a Qxf = 168 THz value, a near zero temperature coefficient of the resonance frequency, and ε = 33. Since then, multiple substitutions for zinc cations have been tried [80, 116, 117]. Increasing cost of Ta_2O_5 used as a precursor for perovskite ceramics made researchers to look for other, cheaper components. The search for materials with good microwave properties and replacements of Ta^{5+} cations with Nb^{5+} cations has been realized. In spite of having the same ionic radius, Nb-based ceramics demonstrated lower values of the quality factor, more positive values of the temperature coefficient of the resonance frequency, and higher values of the dielectric constant (Table 3.1). In particular, BZN and BCN materials have values of the coefficient of resonance frequency of similar order of magnitude but with different signs. In order to attain temperature stability, properties of $(1-x)BaCo_{1/3}Nb_{2/3}O_3$-$xBaZn_{1/3}Nb_{2/3}O_3$ ceramics were studied [119,120]. For x = 0.3, the frequency drift due to temperature variation was compensated, and simultaneously, the

quality factor of the system was improved, reaching its maximum value (Qxf = 97THz). In spite of acceptable microwave characteristics of the niobium group of 1:2 ordered barium perovskites, losses and temperature stabilities in the tantalum analogues still have superior values. The origin of the differences in the dielectric properties of isostructural materials is still far from a complete understanding.

Table 3.1 Dielectric properties of 1:2 ordered barium-based family of perovskite materials (τ_f- temperature coefficient of the resonant frequency, ε - dielectric constant, Qxf- product of quality factor and resonance frequency, *t*-tolerance factor).

Material	τ_f, ppm/K	ε	Qxf, 10^{12} Hz	t
$Ba(Mg_{1/3}Ta_{2/3})O_3$ [116,117]	2.7...5.4	24...25	176...430	1.029
$Ba(Zn_{1/3}Ta_{2/3})O_3$ [11,23]	0	29...30	80...170	1.026
$Ba(Co_{1/3}Ta_{2/3})O_3$ [80]	-16	25	46	1.025
$Ba(Mg_{1/3}Nb_{2/3})O_3$ [76,80,121]	14...34	31...34	39...160	1.029
$Ba(Zn_{1/3}Nb_{2/3})O_3$ [118]	30	41	54	1.026
$Ba(Co_{1/3}Nb_{2/3})O_3$ [119,120]	-10	33	70	1.025
$Ba(Ni_{1/3}Nb_{2/3})O_3$ [80,121]	-5...20	35...36	35...70	1.034
$(1-x)Ba(Co_{1/3}Nb_{2/3})O_3$-$xBa(Zn_{1/3}Nb_{2/3})O_3$ [119,122]	0	34	55...97	-

Most of the research on the dielectric properties of Ba-based 1:2 ordered perovskites has been mainly focused on the improvement of processing conditions;

limited numbers of theoretical studies have been reported [123-125]. Takahashi studying the phase stability of $Ba(B'_{1/3}B''_{2/3})O_3$ (B' = Co, Mg, Mn, Ni, Zn, B" = Nb, Ta) structures performed first principle calculations [123]. He demonstrated that a difference in formation energies of 1:2 ordered-disordered structures is responsible for the microwave behavior. More stable ordered (relative to disordered) structures demonstrate larger Qxf values. While showing agreement with experimental findings for most of the considered materials, according to his calculations, $Ba(Co_{1/3}Ta_{2/3})O_3$ and $Ba(Mn_{1/3}Nb_{2/3})O_3$ materials should exist only in disordered phases, contradicting experimental results [114]. Tagantsev *et al* [126] studying losses in centrosymmetric crystals deduced that microwave losses are proportional to the second power of the dielectric constant ($\varepsilon'' \sim \varepsilon$). This explains why niobium compounds having higher dielectric constants possess low quality factors in comparison to isostructural tantalum materials.

The search for new materials suitable for microwave applications resulted in the study of dielectric properties of the 1:1 family of perovskites [93,127]. Although the reported values of their dielectric constants are close to tantalum based 1:2 ordered perovskites (ε = 20-30) and Qxf values reaching 56THz, large temperature coefficients of the resonance frequencies make this class of materials unacceptable for practical applications, requiring further research.

3.4 Origin of dielectric loss at microwave frequencies

Dielectric losses in real materials operating at microwave frequencies can be attributed to two main groups: intrinsic and extrinsic. The first type of losses, intrinsic, appears in perfect crystals as a result of the interaction of the applied a.c. electric field with phonons of the system. The origin of extrinsic losses observed in real materials is connected to phonon scattering on lattice or structural defects, like point defects, interstitials, dislocations, voids, grain boundaries and impurities.

3.5 Intrinsic losses

Intrinsic losses result from anharmonic phonon decay processes and represent the lowest losses that can be achieved in a system by material processing. Thus, the minimum losses that can be achieved in the system depend on the periodical arrangement

Table 3.2 Order-disorder transition temperatures of the barium family of 1:2 ordered perovskites.

Material	Transition temperature, °C
$Ba(Mg_{1/3}Ta_{2/3})O_3$ [129]	>1650
$Ba(Zn_{1/3}Ta_{2/3})O_3$ [130]	1600...1625
$Ba(Mg_{1/3}Nb_{2/3})O_3$ [131]	1610
$Ba(Zn_{1/3}Nb_{2/3})O_3$ [131]	1380
$Ba(Co_{1/3}Nb_{2/3})O_3$ [15]	1400

of the elements present in the structure. Schlomann demonstrated the importance of the ordered arrangement of ions in dielectric materials on dielectric losses in 1964 [128]. He predicted that a break in the periodic arrangement of charges, as a result of disorder, would increase dielectric losses. Schlomann's theory is in agreement with most experimental findings in $Ba(B'_{1/3}B''_{2/3})O_3$ perovskites [e.g. 13-15].

The studied family of 1:2 ordered perovskite type materials remains thermodynamically stable below some temperature (T_{trans}). By increasing the preparation temperature T above T_{trans}, the structure changes its symmetry and becomes disordered. Table 3.2 shows transition temperatures for some technologically important barium-based 1:2 ordered perovskites.

3.5.1 Debye losses

The problem of dielectric losses was first considered by Debye [132], who investigated losses in liquids with a permanent dipole moment. Viscous friction of rotating dipoles against the surrounding particles in an external a.c. electrical field produces losses that according to Debye are proportional to:

$$tan\delta \sim \frac{\omega\tau}{1+(\omega\tau)^2} \tag{3.5}$$

τ is a characteristic relaxation time and ω is the frequency of the alternating electric field. Debye theory was derived for polar liquids and, thus, is not valid for crystals that do not contain a permanent dipole moment. According to equation (3.5), dielectric losses tend to zero at high frequencies; this contradicts experimental observations.

Today's theory of intrinsic losses at microwave frequencies was formulated by Gurevich and Tagantsev [133,134] for all 32 symmetry groups. The starting point was the assumption that the frequency of an electromagnetic field is small in comparison to the phonon frequencies. In a harmonic approximation, the interaction of the applied field with optical vibrations has resonant character. Conservation of energy and momentum imposes limitations on phonons involved. In the microwave range, no phonon exists with frequency and wavevector being equal to those of the microwave field. Gurevich and Tagantsev considered three main lattice loss mechanisms that permit absorption of the microwave quanta and allow overcoming restrictions on the energy and quasi-momentum of phonons involved in the absorption process: a) three-quantum loss, b) four-quantum loss and c) quasi-Debye loss.

3.5.2 Three-quantum loss

During three-quantum loss, the process of absorption of electromagnetic radiation by a lattice involves two phonons. Energy and momentum conservation laws for the three-quantum loss mechanism have the following form:

$$\Omega_j(\mathbf{k}) \pm \Omega_{j1}(\mathbf{k}_1) = \omega \tag{3.6}$$

$$\mathbf{k} \pm \mathbf{k_1} = 0 \tag{3.7}$$

where Ω_j and Ω_{j1} are angular eigenfrequencies of j and $j1$ phonons, ω is the frequency of the applied field and $\mathbf{k}$ is the phonon wavevector. Restriction (3.7) on wavevectors involved in the absorption process implies that only a small region in k-space contributes to absorption. The three-quantum loss mechanism corresponds to transitions between

states of the different branches of the Brillouin zone involving small regions in k-space where branches either move toward one another so that the energy gap satisfies the condition $\Omega_j - \Omega_{j1} \sim \omega$, or overlap because of their natural linewidth.

3.5.3 Four-quantum loss

The existence of the four-quantum loss absorption process was demonstrated by Stolen and Dransfeld [135]. For this mechanism involving three phonons, the conservation laws can be represented as:

$$\Omega_j(\mathbf{k}) \pm \Omega_{j1}(\mathbf{k}_1) \pm \Omega_{j2}(\mathbf{k}_2) = \omega \tag{3.8}$$

$$\mathbf{k} \pm \mathbf{k}_1 \pm \mathbf{k}_2 = \mathbf{b} \tag{3.9}$$

where **b** is a reciprocal lattice vector. Phonon-phonon collisions causing intrinsic losses in the system are characterized by a lattice anharmonicity parameter $\mu << 1$ [133]. Although the probability of the four-quantum loss mechanism is proportional to a higher power of the lattice anharmonicity parameter in comparison to the three-quantum loss processes, less stringent restrictions imposed by the wavevector conservation law (equation (3.9)) makes contribution of both processes to the total loss in the system about equal. The four-quantum loss process corresponds to transitions between states of different branches, and because of less stringent limitations on the wavevectors of phonons involved, those transitions are uniform over k-space.

3.5.4 Quasi-Debye loss

Gurevich and Tagantsev [133] emphasized the existence of another mechanism of intrinsic loss that was previously described by Coombs and Cowley [136]: perturbation of the phonon distribution function caused by an a.c. field produces losses similar in form to equation (3.5). Those are so-called quasi-Debye losses that take place between states of the same branch because of its finite linewidth.

The importance of the theory developed by Gurevich and Tagantsev is that it predicts different frequency and temperature dependencies for systems with different symmetries. Considering two broad groups of materials (centrosymmetric and non-centrosymmetric crystal systems), the aforementioned authors concluded that for non-centrosymmetric crystals, three quantum and quasi-Debye losses are dominant, while for centrosymmetric crystals, three- and four-quantum losses prevail (Fig.3.1a and b). At high frequencies, dielectric losses of both classes of crystals behave similarly: they increase with frequency. For centrosymmetric systems, this increase is monotonous with three-quantum loss dominating at higher frequencies. In the case of non-centrosymmetric materials, the presence of the quasi-Debye mechanism produces a maximum of dielectric loss at low frequencies ($\omega \approx \Gamma$) than losses fall off and again monotonously increases due to three-quantum loss process.

3.6 Extrinsic losses

Ceramic materials typically consist of a group of grains separated by intergrain boundaries and voids. Inside of each of the grains, perfect crystallinity can be disrupted

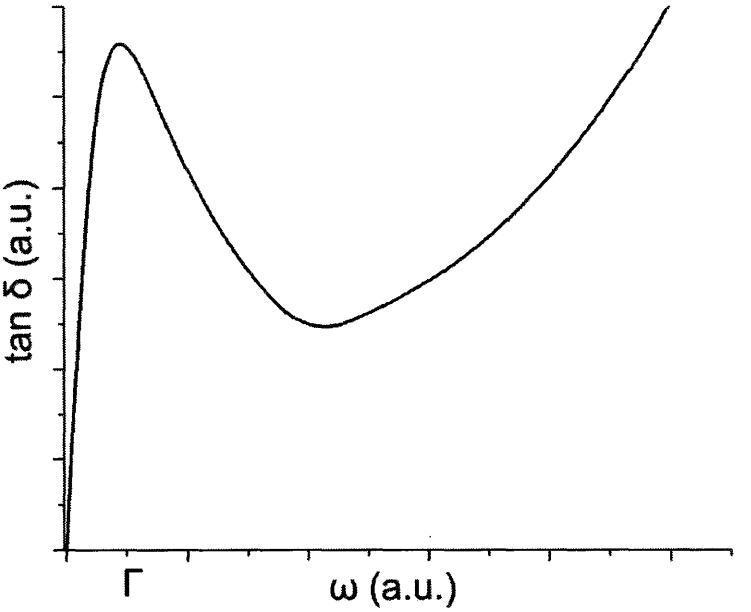

a)

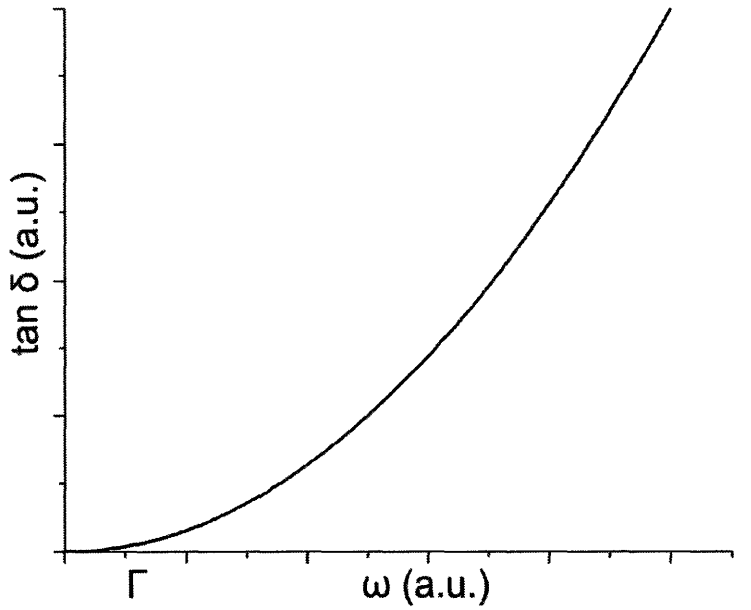

b)

Figure 3.1 Schematic diagrams of the frequency dependence of the dielectric loss (Γ is the characteristic damping for the phonons). a) Non-centrosymmetric b) centrosymmetric crystals.

by the presence of point defects, dislocations and impurities. Gurevich and Tagantsev [133] emphasized the importance of extrinsic losses in centrosymmetric materials where intrinsic losses are relatively small. The significance of extrinsic losses in the absorption process is that the defect-containing material can induce a one-phonon absorption process, while in defect free materials, one-phonon absorption processes are forbidden.

3.6.1 Crystalline defects and dopants

Considering the possibility of a one phonon absorption process in crystalline defects, Gurevich and Tagantsev calculated that for uncharged point defects $tan\delta \sim \omega^3$; for two-dimensional uncharged defects like borders between crystallites and stacking faults, $tan\delta \sim \omega$; and linear defects like dislocations have $tan\delta \sim \omega^2$ frequency dependence. The presence of charged point defects significantly changes the dielectric loss function: for charged defects with an uncorrelated position and with the average distance between defects larger than the wavelength of generated acoustic phonons, $tan\delta \sim \omega$.

In addition to direct contributions to the dielectric losses in a system, the presence of point defects can generate a local charge imbalance thereby altering the sizes of the 1:2 ordered domains responsible for microwave properties [137,138]. Yoon *et al* studying $BaWO_4$ doped $Ba(Mg_{1/3}Ta_{2/3})O_3$ perovskite observed improvements in dielectric losses which they attributed to an increase in the degree of long range 1:2 ordering through compensation of oxygen vacancies by W^{6+}[137]. Opposite results were obtained by Tamura *et al* [80] and Davies *et al* [13]. Upon studying $BaZrO_3$-doped $Ba(Zn_{1/3}Ta_{2/3})O_3$

ceramic, the authors observed an increase in the quality factor and a reduction in the size of ordered domains. The formation of a large number of small-size ordered domains increases the amount of two-dimensional defects that should inevitably result in a poor quality factor. Davies *et al* [13] attributed this inconsistency to a segregation of Zr cations at domain boundaries and stabilization of the boundary regions. The authors emphasized the importance of the substituent size: Zr^{4+} and Sn^{4+} from respective $BaZrO_4$ and $BaSnO_4$ [139] reagents improved the microwave quality factor while additions of $SrTiO_3$ to $Ba(Zn_{1/3}Ta_{2/3})O_3$ had the opposite effect [80].

3.6.2 Porosity

Porosity of a material is closely related to its density and grain sizes. The presence of voids in a sintered material - open spaces between grains which decrease the value of the dielectric constant - significantly degrade the quality factor. Grain boundaries as well as walls of voids represent terminated crystallites with broken bonds and uncompensated charges. The occurrence of broken bonds and charge misbalance can result in structure relaxation [140,141]. The change in the local ionic environment results in a change of the phonon spectrum of the surface modifying the dielectric loss function.

The presence of point defects at the grain boundaries in addition to surface relaxation can promote cation ordering. The process of ordering involves interdiffusion of B' and B" site cations [142]. In order for a B" cation to occupy a B' site, the latter should be vacant. B-site vacancies can be created by Schottky or Frenkel mechanisms, both of which depend on the ion packing density of the structure. Schottky defects form when

oppositely charged ions vacate their lattice sites creating vacancies, which are able to move within the crystal. The requirement to maintain electroneutrality restricts the formation of defects to stoichiometric units. The Frenkel mechanism involves only one atom or ion that leaves its lattice site and forms an interstitial in a nearby region, leaving a vacancy behind. The first defect type, Schottky, can be formed at the surface and then diffuse in the bulk, while the second type, Frenkel, can be formed in the bulk or near the surface. Bokov *et al* [143] investigated the ordering mechanism in $Pb_2B'B''O_6$ structures and came to the conclusion that ordering proceeds not through a nucleation mechanism but rather due to interdiffusion of cations because of inhomogeneous defect distribution within grains. In ceramics, significant inhomogeneities in the distribution of ion vacancies are usually observed, and their concentration rises from the bulk of the grain toward its boundary and from the center of the sample toward its surface [144,145]. This makes the cation diffusion coefficient different for different parts of the sample. In view of this, the characteristic time of ordering is lower in the boundary region. For example, Randall *et al* studying 1:1 ordered $Pb(Sc_{1/2}Ta_{1/2})O_3$ single crystals and ceramic materials found that the largest concentration and size of the ordered domains was in ceramic materials and in particular near grain boundaries [146].

The presence of additives can change grain size and shape distributions. For example, Wakino observed that when Fe_2O_3 was added to the $(Zr,Sn)TiO_4$ system, the grain growth rate was accelerated and the grain shape was changed in comparison to the undoped material [7]. In general, poorly prepared materials with low densities often demonstrate high dielectric losses [114,116,147].

This section provided several examples of the interconnection between intrinsic and extrinsic dielectric losses. In particular, the presence of point defects that influence extrinsic dielectric losses can promote cation ordering and decrease the intrinsic part of losses. The introduction of additives that stabilize cation ordering can change materials' microstructure and modify the overall dielectric losses. The next chapters are focused on the mechanism of ceramic formation and methods used to determine the ordering behavior of perovskite type oxides.

Chapter 4

Optical Properties

4.1 Raman Spectroscopy

As demonstrated in the previous chapter, non-harmonic lattice vibrations causing phonon-phonon collisions are responsible for the minimal, intrinsic, losses present in the system. It is generally accepted that the lattice absorption in an ideal crystal can be estimated by infrared (IR) and far-infrared (FIR) spectroscopy [148-151]. The simplest model describing intrinsic losses in the IR and FIR range is based on representing a lattice structure as a set of additive damped harmonic oscillators. The corresponding dielectric function can be represented as

$$\varepsilon(\omega) = \varepsilon_{\infty} + \sum_{j=1}^{n} \frac{S_j}{\omega_j^2 - \omega^2 - i\omega\gamma_j} \tag{4.1}$$

where S_j, ω_j and γ_j are, respectively, strength, eigenfrequency and damping of the j-th phonon mode. The summation goes over all n polar modes, which are determined by factor group analysis [152]. By extrapolating equation (4.1) down to the microwave region, losses at microwave frequencies can be estimated. The benefit of using IR and FIR spectroscopy to study dielectric losses is that unlike microwave losses, the infrared reflectivity signal from a dense material is not sensitive to the processing conditions of a sample and can be used to estimate minimal microwave losses and permittivity [153, 154]. In spite of apparent simplicity of estimating microwave losses from the IR reflection spectra, a significant problem arises from the broad vibrational peaks in the

IR region of the studied perovskite oxides, some of which significantly overlap. The Raman technique, however, which is often considered as complementary to IR reflection measurements to characterize lattice vibrations, produces spectra with sharp peaks and has been extensively used to characterize dielectric losses in perovskite materials.

4.1.1 Analysis of Raman spectra

Extensive literature data on the application of Raman spectroscopy to the study of vibrational spectra of perovskite type materials demonstrates two contrasting but not exclusive approaches. Group theory analysis predicts that ABO_3 structures are not Raman active. Substitution of several different cations on either A- or B-sites producing a complex cation arrangement should result in changes of vibrational spectra. Disordered perovskites containing two different cations and having the same space group as an ideal ABO_3 structure are expected to be Raman inactive. According to the first approach used to analyze Raman spectra, disorder leads to a break in both translational and inversion symmetries. Changes in crystal symmetry from ideal cubic to some lower one like tetragonal, orthorhombic, trigonal or monoclinic can also change selection rules allowing Raman modes [155, 156], as a result, for example, of the presence of undersized A-site cation and subsequent tilting of BO_6 octahedra. The selection rules used to predict IR and Raman activities of a material are no longer valid in such a system and contribution of light scattering from some points of the Brillouin

zone and from IR-active and silent modes becomes possible. This approach was used to explain the appearance of Raman spectra in disordered $KTa_{0.64}Nb_{0.36}O_3$ structures [157].

The second approach is based on the assumption of the existence of ordered regions with a particular symmetry that permits the appearance of Raman modes. These two approaches are not mutually exclusive and the contribution of both of them can be used to explain experimental data. For example, Bismayer *et al* used both theories to give an explanation of Raman scattering in ordered and disordered samples of $Pb(Sc_{1/2}Ta_{1/2})O_3$ perovskites [158].

4.1.2 Group theory predictions for perovskite oxides

Table 4.1 summarizes the group theoretical analysis of vibrational spectra of $A(B',B'')O_3$ complex perovskites.

Vibrations of ions inside of the lattice are described by a set of symmetry operations and represented by Mulliken symbols [159]. Depending on the symmetry of vibrations with respect to the symmetry axis of the greatest multiplicity, vibrations are classified as types A (singly degenerate symmetric vibration) or B (singly degenerate antisymmetric vibration). Doubly and triply degenerate vibrations belong to type E and F, respectively. Mulliken symbols of vibrations that are symmetric (antisymmetric) with respect to a vertical mirror plane have subscript 1 or 2, respectively. In order to characterize the symmetry of vibrations relative to the center of symmetry *g* and *u* subscripts are employed: *g* denotes symmetric and *u* antisymmetric vibration.

Table 4.1 Group theory predictions of Raman and IR spectra for several space groups.

Structure	ABO_3	$A(B'_{1/2}B''_{1/2})O_3$	$A(B'_{1/3}B''_{2/3})O_3$
Space group	Pm-3m	Fm3m	P-3m1
Raman modes	---	$A_{1g}(O)$ $E_g(O)$ $2F_{2g}(A,O)$	$4A_{1g}(A,B'',O)$ $5E_g(A,B'',O)$
IR modes	$3F_{1u}(A,B,O)$	$4F_{1u}(A,B',B'',O)$	$7A_{2u}(A,B',B'',O)$ $9E_u(A,B',B'',O)$

The above-mentioned ideal cubic structure with two undistinguishable B-sites implying complete disorder, while having three IR-active modes, is not Raman active. According to the symmetry considerations, formation of 1:1 and 1:2 ordered structures produces two different anion complexes around B' and B" cations that leads to four and nine Raman active modes, respectively.

Presently there is no consensus among the scientific community on the Raman mode assignment of complex perovskites. One of the approaches used to identify the symmetry of the structure and atoms involved in the vibration is based on the removal of the degeneracy of modes. For example, 1:1 ordered structures are expected to produce one doubly-degenerate E_g mode due to internal oxygen vibrations and two triply-degenerate modes originating from mutual vibrations of A- and O- ions (Table 4.1). The splitting of triply degenerate F_{2g} modes ($F_{2g} \rightarrow A_{1g}+E_g$) was found in $Pb(Mg_{1/2}W_{1/2})O_3$ [160] and $Ba(Y_{1/2}Ta_{1/2})O_3$ [161]. Mode splitting can be decisive

evidence for mode assignment and structure identification. The significant feature of 1:2 ordered structures, according to the group theory predictions, is the coupling of A_{1g} and E_g modes of A-, B"- and O- ions that leads to the frequency dependence of Raman active modes on the masses of usually heavy A- and B"- cations.

A typical Raman spectrum reported in literature and obtained in present research is shown on Fig. 4.1. The spectrum is characterized by the formation of four intensive modes in low (~105cm^{-1}), medium (~380 and ~430cm^{-1}) and high (~800cm^{-1}) frequency regions and weak modes in the ~175-300cm^{-1} region. The appearance of four intensive modes is a characteristic feature of both 1:1 and 1:2 ordered materials. For example, similar Raman spectra were reported for 1:2 ordered $Ba(B'_{1/3}B''_{2/3})O_3$ (B' = Mg, Zn, B"= Nb, Ta) [162-165] and 1:1 ordered $Sr(Al_{1/2}B_{1/2})O_3$ (B = Nb or Ta) [166] materials. Based on similarities of Raman spectra, in their research, Siny *et al* [167] attributed the appearance of intensive modes in the $Ba(Mg_{1/3}Ta_{2/3})O_3$ system to the formation of 1:1 ordered nanoregions. Weak "extra lines" were ascribed to 1:2 ordered domains.

Formation of 1:1 order in materials with 1:2 cation ratio was explained based on the "space-charge" model that assumes the formation of regions rich in B". Ta-rich regions, that form around 1:1 ordered domains are responsible for local distortion and splitting of triply degenerate modes observed during experiments in the BMT perovskite.

The opposite approach based on the presence of only 1:2 order and disorder was undertaken by Moreira *et al* [168] and Dias *et al* [169]. Considering materials with a

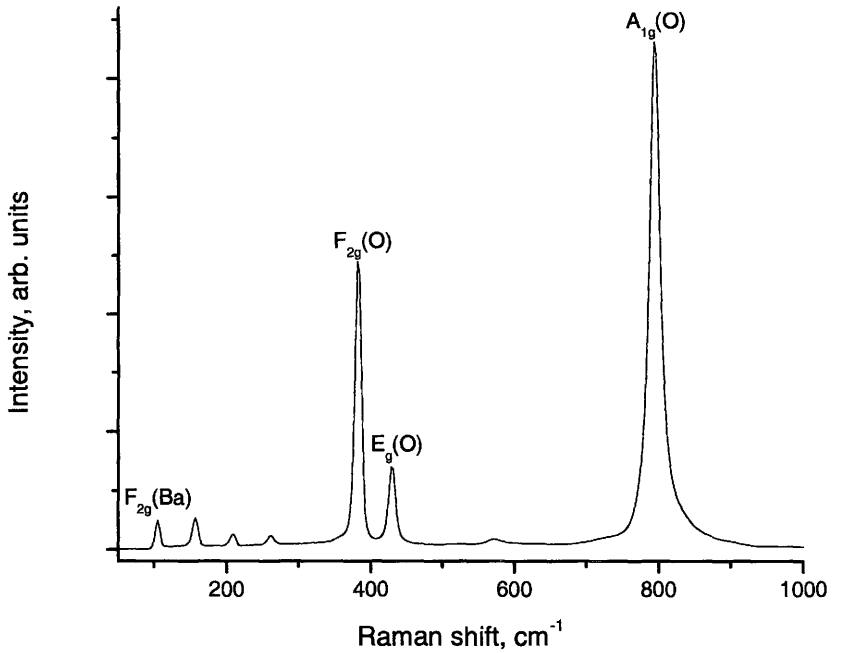

Figure 4.1 Example of a typical Raman spectrum of the 1:2 ordered $Ba(B'_{1/3}B''_{2/3})O_3$ perovskite and mode assignment according to ref. [167].

different degree of long range 1:2 order they assumed the existence of nine Raman modes in the completely ordered structure and eleven modes in structures with partial order. Mode assignment was based on the variation of intensities of Raman peaks and the expected change in 1:2 order with sintering temperature.

In spite of the disagreement on the origin of the observed Raman peaks, it has been demonstrated by several groups that the line widths of Raman peaks correlate with dielectric losses at microwave frequencies [169-172]. Lee *et al* [170] attributed the origin of the four intensive lines to the formation of 1:1 ordered phase and showed that the full width at half maximum (FWHM) of the observed modes decreases with increase in the Q-value. Chia *et al* [172] showed that the FWHM of weak Raman modes

in the ~175-300cm^{-1} frequency region also changes in the same way with the quality factor: a decrease in FWHM is accompanied by a reduction in dielectric losses. The 800cm^{-1} mode that was a characteristic feature of the most complex perovskites corresponds to a symmetric stretching mode of an oxygen octahedron formed around a B-site cation. The $A_{1g}(O)$ mode represents the collective movement of oxygen anions and was first described by Tamura *et al* [163]. The $A_{1g}(O)$ mode in highly ordered materials like $Ba(Mg_{1/3}Ta_{2/3})O_3$ is very narrow in comparison to partially ordered perovskites like $Pb(Mg_{1/3}Ta_{2/3})O_3$ and $Pb(Sr_{1/2}Ta_{1/2})O_3$ where ordering occurs on the scale of several nanometers [173]. Change in the FWHM of the oxygen octahedron breathing type mode indicates a variation in the ordering degree.

Previous discussion of dielectric losses demonstrated their dependence on intrinsic and extrinsic sources. Correlation of the line shape of Raman spectra with the microwave quality factor implies that the FWHM is an integrated value that includes the influence of both internal (crystal structure) and external (presence of defects, second phases and so on) factors. This makes the Raman technique sensitive to ceramic processing conditions.

Correlation of the Raman line shape with the quality factor at microwave frequencies is used in the present work to correlate relative changes in dielectric losses with a deviation in the nominal composition of A- and B-site cations.

4.2 Photoluminescence spectroscopy

Chapter 2 demonstrated that complex perovskites containing two dissimilar cations on the B-site are unstable. In the case of the 1:2 ratio of the B-site cations, formation of 1:2 ordered structures was observed only in materials having transition metal cations with a specific electronic configuration: the presence of empty *d*-orbitals of transition metal ions that were able to mix with ligands' orbitals was required for structure stabilization. Contrary to this, materials containing a transition metal cation with partially or completely filled *d*-orbitals that are not able to mix with ligands' orbitals crystallize in lower symmetry [174].

The transition metal-ligand interaction within a BO_n^m complex (n- number of oxygen ions and m- charge of the complex) has been studied by luminescence spectroscopy. A number of theoretical simulations demonstrated that an emission signal appearing from the considered oxygen complex is due to the electron transfer from a molecular orbital with no contribution of metal orbitals to a molecular orbital formed from metal atomic orbitals [175-177].

In a free metal atom, *d*-orbitals designated as d_{xy}, d_{xz}, d_{yz}, $d_{x^2-y^2}$ and d_{z^2} are five-fold degenerate. When a transition metal atom is introduced in a molecule, the five-fold degeneracy is removed due to interaction of atomic orbitals of the metal having different spatial distribution of electrons with orbitals of ligands. Two of the most frequently encountered cases of atomic arrangements are tetragonal and octahedral complexes. In a tetragonal structure with d_{xy}, d_{xz}, d_{yz} (triply degenerate t_{2g} orbitals in a molecule) metal orbitals pointing toward ligands and $d_{x^2-y^2}$ and d_{z^2} (double degenerate e_g

orbitals) pointing toward low ligand electron density, according to the ligand field theory, the interaction between electronic clouds results in lowering in energy of e_g and raising in energy of t_{2g} orbitals. Thus, ligands' field partially removes the degeneracy of metal *d*-orbitals. A similar scenario is observed in octahedral complexes with the difference that the t_{2g} orbitals move down and the e_g orbitals move up due to the spatial arrangement of ligands' orbitals relative to the metal ones. Lowering in symmetry from tetragonal/octahedral structures can further split t_{2g} and e_g orbitals. Centrosymmetric tetragonal distortion observed in $SrTiO_3$ at 108K demonstrated splitting of t_{2g} and e_g energy levels [178]. The effect of distortion on the energy levels' splitting is determined, once again, by the mutual orientation of metal-ligands orbitals; it is stronger for e_g orbitals.

The sensitivity of the band-gap formed between HOMO oxygen *2p* orbitals and LUMO transition metal orbitals to crystal symmetry was used to study structural distortion in a number of materials. In [179], the authors observed two luminescent bands in a A_2MWO_6 (M- metal ion) material. The appearance of two peaks was attributed to the presence of two different WO_6 emission complexes: the regular one with M- and W- cations on their own crystallographic sites, and the distorted one due to disorder on the B-site. Blasse *et al* [180] studying emission and absorption spectra of $Ba_3SrNb_2O_9$ perovskite demonstrated the presence of two NbO_6 groups having different oxygen surroundings.

Sensitivity of luminescence spectroscopy to changes in local cation environment and the absence of detailed experimental studies in this area motivated us to use the

technique to study structural distortions in complex $Ba(B'_{1/3}B''_{2/3})O_3$ perovskites caused by disorder- order phase transitions and subsequent structure stabilization. The presence of point defects like missing oxygen or transition metal ions that are responsible for charge transfer transition due to changes in materials microstructure is expected to influence the luminescence signal. The next chapter briefly describes the mechanism of ceramic formation and different types of defects accompanying the sintering process.

Chapter 5

Microstructure

The microstructure of materials determines many physical properties of ceramics, like optical activity through formation of emission/absorption centers or conducting/dielectric properties that depend on the presence of point defects that facilitate charge transfer. That is why the influence of microstructure on the optical and dielectric properties of perovskite type materials is a main aspect addressed in the present work.

5.1 Sintering Process

Ceramic preparation involves compacting of powders and then firing them at elevated temperatures. During the firing process, changes occur because of decomposition and phase transformations. The sintering process can generally be considered as consisting of two stages: primary and secondary recrystallization. The first one includes nucleation and growth of strain free grains, while secondary recrystallization implies abnormal grain growth of several larger grains at the expense of smaller ones.

5.1.1 Primary recrystallization

The first part of the primary recrystallization process is nucleation or formation of embryos that takes place on inhomogeneities present in powder. The formation and

growth of new particles involves an increase in the surface area having energy different from the bulk of the material. An increase in the size of a particle is accompanied by an increase in the surface energy. The surface to volume energy ratio defines the growth process. For a nucleus having a high surface to volume ratio, the necessity to overcome surface tension makes the growth process unstable. Formation of embryos is random and independent of initial preparation conditions for the given compacts. The nucleation rate has exponential temperature dependence:

$$\frac{dN}{dt} = N_0 exp\left(-\frac{\Delta G}{RT}\right) \tag{5.1}$$

where N is the number of nuclei, N_0 is the number of potential nucleation sites, ΔG is the Gibbs free energy for nucleation, R is the gas constant, T is the temperature of the process and t is time.

The grain growth process during primary recrystallization has its driving force from the increase in energy of the deformed matrix. The stored energy that is usually 0.5-1 cal/g is sufficient to affect grain-boundary movement [181]. At this stage the grain growth rate at constant temperature is given by:

$$U = \frac{d}{t - t_0} \tag{5.2}$$

where d is the size of the grain, t- time and t_0- induction period (time required for the nucleation process). Grain growth occurs due to jumping of an atom from one site of a boundary to the other and resembles the atomic diffusion process. Similarities in those two processes define the temperature dependence of the grain growth rate:

$$U = U_0 exp\left(-\frac{E_a}{RT}\right) \tag{5.3}$$

where E_a is the activation energy.

The constant driving force at a given temperature that is equal to the difference in energy between strained and strain free materials makes the growth rate constant over time, enabling control over the grain growth rate by exerting different initial strains in the matrix or sintering material for a longer time. During the primary recrystallization process, grain growth occurs until grains start to impinge on one another. So, the final grain size will be determined by both the number of nuclei and the initial energy supplied to a material.

5.1.2 Secondary recrystallization

The surface of a grain is a region of high energy in comparison to the bulk of the material. Any inclusion, such as a secondary phase present in the system, tries to occupy a position minimizing the surface energy. The low surface energy component attempts to concentrate on the surface of the grain and, contrary, the high surface tension components are usually found in the bulk of the grain. Interface energy, the energy between two surfaces (either between two grains of the same material or between two different phases) is always less than the sum of two separate surface energies. Thus, it is energetically more favorable to have contact between either two solids or between solid and liquid. Sintering in the presence of a wetting phase is based on the lowering of interfacial energy in comparison to the surface energy of the material.

The driving force for the grain growth that is accompanied by an increase in the surface area is the free energy difference across a curved surface formed by the grain boundary:

$$\Delta G \sim \gamma \frac{1}{r} \tag{5.4}$$

where γ is the boundary energy or surface tension, and r is the radius of curvature. The free energy difference makes the boundary move toward its center of curvature with a rate proportional to the boundary's curvature. The difference in the initial, after primary recrystallization, grain shape defines whether the grain will shrink and disappear or grow. Considering the two-dimensional picture of a material's surface, grains having six sides are the most stable and those with less than six sides tend to become smaller and disappear.

In addition to the influence of secondary phases found randomly near grain boundaries, the size of the final grain depends on the presence of different impurities. During the growing process, grain boundary impinging on impurity particles decreases its surface energy by an amount proportional to the cross-section of the impurity. Further grain growth requires increasing the boundary energy to pull the particle away.

Random distribution of impurity atoms as well as secondary phases can significantly change the distribution of grain sizes forming ceramics with extremely large grains (on the order of the size of the sample) surrounded by fine grains.

Grain coarsening has often been observed in materials containing angular grains or grains with a faceted interface. For example, $BaTiO_3$ [182] and Al_2O_3 [183] oxides belong to those materials exhibiting abnormal grain growth. Park *et al* [26], on the

example of $Ba(Ni_{1/3}Nb_{2/3})O_3$, demonstrated that the grain growth process can be controlled by varying the stoichiometry on barium and niobium sites.

5.2 Microstructure of complex double perovskites

The growth of grains with a large diameter is accompanied by elimination of grain boundaries and voids that are often found between grains. Formation of ordered phases occurs through cation diffusion between adjacent sites. Cation "swapping" can be more easily realized if one of the sites is vacant or if the lattice potential is distorted due to the presence of lattice defects.

5.2.1 Positron annihilation spectroscopy

Positron annihilation spectroscopy has been proven to be sensitive to the change in electron density caused by the presence of defects (like vacancies, vacancy agglomerates, dislocations, grain boundaries) or impurities [184]. The theory of the positron interaction with solids and basics of different positron annihilation techniques are extensively reviewed in the literature [e.g. 185, 186]. Positron lifetime spectroscopy (PLS), considered here, is based on the interaction of a positron with the repulsive potential of the nuclei and attractive potential of defects created by missing nuclei. In a defect free structure where the atomic position is periodic the probability for positrons to be found at the center of the atom is the smallest and peaking in the interstitial regions where the influence of the positive charge of the nuclei is minimal. The characteristic lifetime (called the bulk lifetime (τ_b)) that a positron exists in a defect-

free material is determined by the average electron density of the material, that is, by the electronic configuration of constituent atoms and the lattice parameters of material:

$$\tau^{-1} = \pi r_0 c \int g(0, n_+, n_-) n_-(r) n_+(r) dr \quad (5.5)$$

where r_0 and c are the classical electron radius and the speed of light, n_- and n_+ are electron and positron densities and g is the enhancement factor that takes into account the change in the electron density caused by the presence of the positron.

Formation of different defect types is often characterized by reduced electron density. So, positrons trapped in defects have longer lifetimes (called defect lifetime, τ_d) in comparison with the lifetime of positrons annihilating in the defect-free material.

Positron lifetime spectroscopy has been applied to the study of defect formation in perovskite type materials [187-190]. Based on the theoretical calculations of the bulk and defect lifetimes in $LaCoO_3$, $BaTiO_3$ and $PbTiO_3$ perovskites Ghosh *et al* [187] demonstrated formation of oxygen vacancies and defect complexes (consisting of metal and oxygen vacancies) in $La_{1-x}Sr_xCoO_3$ material. Their results confirmed the appearance of Ba vacancies in ferroelectric $BaTiO_3$ previously reported in [189]. Results of Keeble *et al* [190] on $PbTiO_3$ and $Pb(Zr_{0.42}Ti_{0.58})O_3$ perovskites revealed formation of A- (A = Pb) and B- site (B = Zr and Ti) vacancies as well as metal-oxygen vacancy complexes.

5.2.2 Transmission electron microscopy

The appearance of different types of order has been extensively studied by transmission electron microscopy (TEM) and was usually found near grain boundaries

or structural imperfections [191]. The ordering process involves the respective cation arrangement along the [111] direction of the perovskite cubic unit cell. Cubic symmetry of the initial disordered system enables four equivalent directions for the ordering process. The possibility of cation ordering to happen along any of the four equivalent directions of the cubic cell produces several types of planar defects: antiphase (translational) domain boundaries formed between regions of materials that nucleated out of phase on the same set of (111) planes, domains formed by a structure that nucleated in phase but on a different set of (111) planes that usually form 71/109° angles, domain boundaries formed by areas that nucleated out of phase and on a different set of (111) planes. In electron diffraction patterns, formation of the 1:2 ordered structure creates superlattice reflections that do not correspond to reciprocal lattice points for the cubic cell. So, in addition to {h,k,l} reflections from the fundamental perovskite cell, 1:2 ordering produces weaker reflections at {h±1/3,k±1/3,l±1/3}.

1:1 order with a double perovskite unit cell reveals itself in an electron diffraction pattern as superlattice reflections at the positions {h±1/2, k±1/2, l±1/2}. It should be mentioned that some systems exhibiting antiphase tilting of an oxygen octahedron could also produce the same set of reflections. In case of Ba-based perovskites with the tolerance factors $t > 1$, tilting of the oxygen octahedron does not occur [53, 85] and the appearance of {h±1/2,k±1/2,l±1/2} reflections is unambiguous evidence of the 1:1 ordered structure.

Chapter 6

Experimental Procedure

6.1 Compositions of studied samples

All samples used in the present work were prepared by the conventional mixed oxide method from powders of metal oxides and metal carbonates. The direct sintering route, which is mixing of two corresponding metal oxides with barium carbonate, usually requires higher temperatures (e.g. formation of a single-phase $BaMg_{1/3}Ta_{2/3}O_3$ perovskite was observed only after 10h sintering at 1400°C, while the columbite route, which involves a different pathway through sintering of a BNb_2O_6 compound, led to the formation of single-phase material after 2h heating at 1000°C [192]) and results in the formation of perovskite materials having inferior microwave properties and containing different secondary phases. Contrary to the direct sintering method, columbite route produces perovskite ceramics with a better microwave quality factor and higher ceramic density. In addition, the columbite route can be followed at lower temperatures (1100-1300°C) preventing evaporation of volatile oxides and decreasing the amount of secondary phases.

Grain growth of sintered samples occurs through vapor transport from one grain boundary to another one. The rate of grain growth depends on the presence of impurities and vapor pressure of the constituent elements. The latter in its turn depends on the size of the raw particle powder: fine powder leads to a high grain growth rate.

Table 6.1 shows the purities of initial metal oxides and barium carbonate according to manufacturers' specifications.

Table 6.1 Raw chemicals, purity and manufacturers.

Material	Purity	Manufacturer
ZnO	99.9%	Cerac
Co_3O_4	99.5%	Cerac
Nb_2O_5	99.998%	Cerac
$BaCO_3$	99.9%	Cerac

Table 6.2 Compositions of $Ba_{3+3x}B_{1+y}Nb_2O_9$ (B = Zn or Co) perovskite materials.

Material	3+3x	1+y
$Ba_{3+3x}Zn_{1+y}Nb_2O_9$	2.7	0.93
	2.88	1
	2.94	1.005
	3	
	3.015	
$Ba_{3+3x}Co_{1+y}Nb_2O_9$	2.7	0.93
	2.88	1
	2.94	1.03
	3	
	3.015	

This thesis deals with the near stoichiometric compositions of perovskite type oxides. The summary of compositions considered in the present research is presented in Table 6.2.

In addition to the materials listed in Table 6.2 materials, several sets of $Ba_{3+3x}B_{1+y}Nb_2O_9$ (B = Zn or Co) perovskites with similar nonstoichiometry ranges as well as a stoichiometric $Ba_3MgNb_2O_9$ sample were obtained from the V.I.Vernadskii Institute of General and Inorganic Chemistry NAS of Ukraine. Differences in the preparation process between samples obtained from the Ukrainian group and those prepared at McMaster University will be emphasized later in this chapter.

Two sets of stoichiometric $Ba_3MgNb_2O_9$ and $Ba_3MgTa_2O_9$ samples were obtained from Dr. T. Kolodiazhnyi, National Institute for Materials Science, Tsukuba, Japan. According to the provided specification, $Ba_3MgNb_2O_9$ and $Ba_3MgTa_2O_9$ samples were sintered in air at 1460°C and 1650°C, respectively. One sample from each set was subsequently annealed in H_2 at 1350°C.

The following reactions show the mechanism of samples' preparation used.

Columbite samples:

a) nonstoichiometry on Ba-site

$$ZnO + Nb_2O_5 \rightarrow ZnNb_2O_6 \quad (6.1)$$

$$3Co_3O_4 + 6Nb_2O_5 \rightarrow 6CoNb_2O_6 + O_2 \quad (6.2)$$

b) nonstoichiometry on Zn/Co site

$$2(1+y)ZnO + 2Nb_2O_5 \rightarrow 2Zn_{1+y}Nb_2O_6 + yO_2 \quad (6.3)$$

$$2(1+y)Co_3O_4 + 6Nb_2O_5 \rightarrow 6Co_{1+y}Nb_2O_6 + (1+4y)O_2 \quad (6.4)$$

During the perovskite stage, a proper amount of barium carbonate was added to the columbite samples:

a) nonstoichiometry on Ba site

$$2ZnNb_2O_6 + 6(1+x)BaCO_3 \rightarrow 2Ba_{3+3x}ZnNb_2O_9 + 6(1+x)CO_2 + 3xO_2 \quad (6.5)$$

$$2CoNb_2O_6 + 6(1+x)BaCO_3 \rightarrow 2Ba_{3+3x}CoNb_2O_9 + 6(1+x)CO_2 + 3xO_2 \quad (6.6)$$

b) nonstoichiometry on Zn/Co site

$$Zn_{1+y}Nb_2O_6 + 3BaCO_3 \rightarrow Ba_3Zn_{1+y}Nb_2O_9 + 3CO_2 \quad (6.7)$$

$$Co_{1+y}Nb_2O_6 + 3BaCO_3 \rightarrow Ba_3Co_{1+y}Nb_2O_9 + 3CO_2 \quad (6.8)$$

So, according to the above provided reaction mechanisms, the following preparation processes were used.

6.2 Sample preparation

6.2.1 Weighing of reagents

Prior to weighing of the required amount of raw chemicals, the starting powders were placed in an oven at 100°C for 12h in order to remove adsorbed water. Weighing of large volumes of the appropriate amounts of powders was done on Precisa 1600 that allows ±0.05g accuracy. For compositions containing a small number of samples and requiring more precise weighing of chemicals, a Mettler Toledo AB204-S scale with 10^{-4}g accuracy was used.

6.2.2 Mixing and ball milling

After weighing of the corresponding amounts of raw materials, powders were placed in polyethylene bottles filled with ethanol and yttria stabilized zirconia grinding balls in order to obtain a homogeneous mixture. Vibromilling was done in a Fritsch Pulverisette 6. The duration of mixing was kept constant at 1h with 250rpm. The homogenization process was repeated after the sintering of columbite samples with addition of barium carbonate powder and after the calcination steps prior to final sintering. By using several vibromilling steps, one can break particle agglomerates and increase the surface activity of powders.

6.2.3 Columbite samples

The slurries of mixed metal oxides were placed in coarse porcelain dishes covered with glaze. According to manufacturer specifications, the glaze should not influence the purity of materials until 1200°C. The initial evaporation of ethanol was done under an IR lamp and subsequent drying in the oven at 100°C for at least 10h. Powders were pressed into pellets in a one inch diameter dye with 600kg/cm^2 of pressure. Sintering of columbite samples was performed at 1150°C and 1000°C, respectively for cobalt and zinc columbites. Prior to the sintering process, samples were placed on a high alumina ceramic covered with the corresponding columbite powder. At this stage it was found that the application of alumina firebrick as a holder for columbite pellets was not appropriate because of the increased reaction rate between alumina firebrick and columbite powder used as a substrate. During the columbite preparation

stage, the heating rates were kept constant at 100°C/h, the soaking time was four hours. After sintering at high temperatures, the furnace was turned off and samples were naturally cooled to room temperature.

According to the provided specifications sintering of columbite samples obtained from the V.I.Vernadskii Institute of General and Inorganic Chemistry NAS of Ukraine was performed in the same temperature range.

6.2.4 Calcination

A homogenized mixture of columbite materials and barium carbonate was pressed in one inch pellets (200kg/cm^2) and heated in a furnace at 1300°C (24h) and 1150°C (10h), respectively for cobalt and zinc materials. Lower calcination temperatures with shorter soaking times of zinc samples is required due to their lower stability because of a high evaporation rate of zinc oxide. Application of barium carbonate as a source of barium cations requires the releasing of carbon dioxide (according to reactions 6.5-6.8). In order to provide an escape route for CO_2, lower pressures for pellet preparation were used. Calcination of powdered materials, an alternative to the pelletized samples method, was rejected due to observed reactions during the columbite step between columbite precursors and samples' holders, as well as high calcination temperatures requiring stable containers.

6.2.5 Pressing of perovskite precursors

After the calcination step, homogenized perovskite precursor powder was uniaxially pressed on a laboratory press (Model C, Fred. S Carver Inc., Wis. USA) at a

pressure of 1200kg/cm^2 in ½" diameter discs. In order to obtain a homogeneous pressure distribution within the bulk of the sample, samples were left under pressure for at least one minute. In contrast to the samples prepared at McMaster University, samples provided by the Ukrainian group were pressed at a lower pressure (500-800kg/cm^2). The difference in applied pressures influences reactivity and grain growth rates of perovskite materials.

6.2.6 Sintering of perovskite materials

Pressed tablets were placed on their own powder in order to prevent cross contamination between perovskite materials and the alumina ceramic used as the samples' holder. Zinc perovskites were covered in their own powder and placed under an alumina crucible in order to minimize ZnO evaporation. Sintering was performed in air in the 1250-1500°C temperature range with eight hours of soaking time. The heating and cooling rates were the same as during the columbite step.

Perovskite ceramics obtained from the V.I.Vernadskii Institute of General and Inorganic Chemistry NAS of Ukraine and used in the present studies were sintered for 8h at 1445°C and 1470°C, respectively for the zinc and cobalt perovskites.

6.3 Density measurements

Samples sintered at different temperatures and having different compositions demonstrated different shrinkage and obvious differences in densities. Initial density measurements using the Archimedes method demonstrated that samples having a fragile structure and lower shrinkage have higher density in contrast to those with higher

shrinkage and more robust structures. Because of the obvious difference in porosity and different liquid absorption rates during the Archimedes method, density measurements were done by the usual volumetric method:

$$\rho = \frac{m}{V} \tag{6.9}$$

That is, the volume of the tablet sample was measured by a caliper and then the mass/volume ratio was found. The density of only selected sets of perovskite samples that demonstrated high densification rates were measured by the Archimedes method by using a pycnometer with distilled water as the immersion liquid. The value of the density was found according to:

$$\rho = \frac{m_S \rho_W}{m_S + m_W - m_{S+W}} \tag{6.10}$$

where ρ_W is the density of water, m_S is the weight of the sample, m_W is the weight of water in the pycnometer without the sample and m_{S+W} is the weight of the sample and water when both are in the pycnometer.

6.4 Porosity measurements

The influence of secondary phases found in nonstoichiometric perovskites on the microstructure of samples has been studied by porosity measurements. A piece of material from each sample having approximately similar shape and weight was placed in a beaker filled with toluene. Liquid was forced into pores by placing the beaker in a dessicator connected to a vacuum pump and evacuating the system for 2.5h. The

difference in the mass of samples prior and after submersion in the liquid indicates the relative change in the level of porosity with stoichiometry and sintering temperature.

6.5 Crystallographic and microstructure analysis

6.5.1 Crystallographic analysis

In order to eliminate the influence of the surface layer having a different composition because of the evaporation of oxides, the surfaces of all samples were polished prior to measurements. For X-ray diffraction analysis, the sintered samples were first ground in an agate mortar. The phase composition and crystal lattice parameters of sintered ceramics were examined at room temperature in the $2\theta = 10\text{-}45^0$ range by a PANalytical X'pert Pro diffractometer with an X'Celerator detector and Cu $K_{\alpha 1}$ radiation. The scanning step was 0.008^0.

6.5.2 Transmission electron microscopy and electron diffraction analysis

For transmission electron microscopy (TEM) measurements, disks with a thickness of 300μm were cut from the corresponding samples and subsequently mechanically ground using SiC paper to a thickness of 100μm. Prior to further processing, samples were mounted on molybdenum rings. Dimpling to the thickness of 30μm was done on a Gatan dimpling apparatus. Further thinning of the central part of the samples was obtained by Ar^+ ion milling in a Gatan Precision Ion Polishing System,

Model 691. The milling was performed at an accelerating voltage of 4kV and a tilt angle of 4°. In order to avoid charging effects observed during initial TEM measurements, samples were carbon coated. The TEM investigation and electron diffraction experiments were done on a Philips CM12 system operating at 120kV and equipped with a double-tilt sample holder.

6.5.3 Scanning electron microscope analysis

The microstructure and the chemical composition of selected samples were analyzed by a scanning electron microscope (SEM, JSM-7000F) equipped with an Energy Dispersive Spectrometer (EDS, Oxford Instruments). Some of the measurements were done on the cracked surfaces of samples. The others were performed on polished and thermally etched samples. Polishing of sections of the samples was done stepwise by 9μm, 3μm and 1μm diamond paste followed by thermal etching for two hours at temperatures 200°C below the sintering temperature. Surfaces of all samples were coated with a thin layer of carbon.

6.6 Positron lifetime spectroscopy

The defect structure of perovskite samples obtained from the V.I.Vernadskii Institute of General and Inorganic Chemistry NAS of Ukraine was analyzed by positron lifetime spectroscopy (PLS) during the course of work for the degree of Master of Applied Science [184].

The source of positrons (^{22}Na) was sandwiched between two identical samples that were thick enough to guarantee that all annihilation occurs in the material of the samples. Positron lifetimes were detected by measuring the time difference between the 1.27MeV (indicating the birth of positron in the source) and one of the annihilation 511keV γ-quanta. A schematic of the PLS experimental setup is given in fig.5.1.

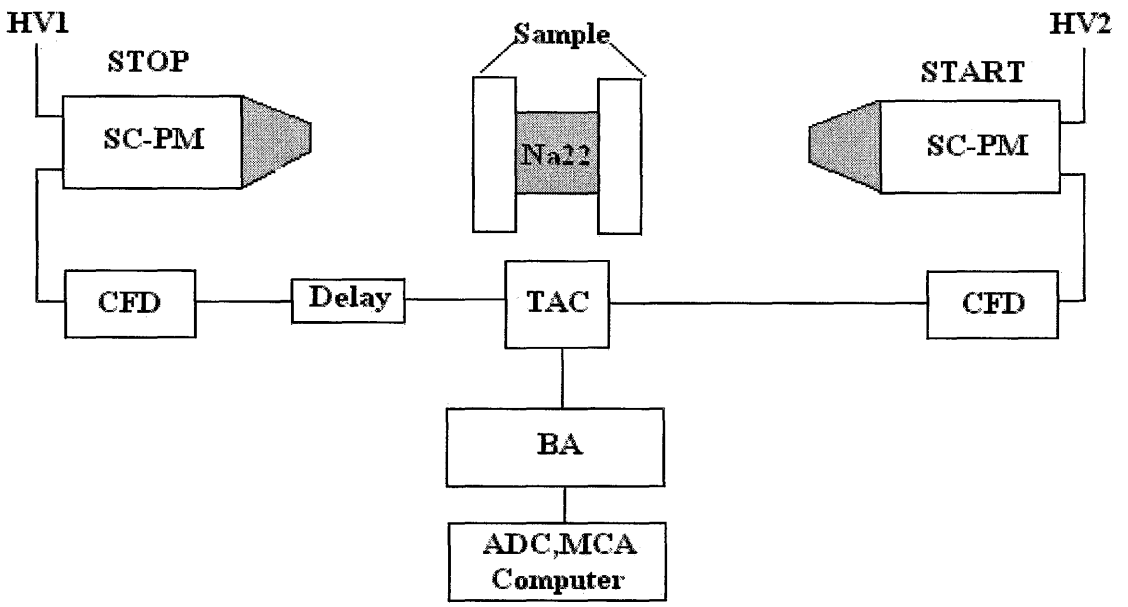

Figure 6.1 Positron lifetime experimental setup (HV- high-voltage power supply, SC-PM - scintillator photomultiplier assembly, CFD- constant fraction discriminator, TAC- time- to- amplitude converter, Delay- delay line, BA- biased amplifier, ADC- analog-to-digital converter, MCA- multichannel analyzer) [184].

For each pair of samples at least three spectra containing six million counts were recorded. The source strength was $20\mu Ci$ and the system resolution was $280ps$. PATFIT88 was used to analyze experimental spectra [193]. After source correction (155 and $256ps$ with intensities 28 and 72%, respectively and total intensity of 9.6%) and background subtraction the spectra were decomposed into two components having

lifetime values τ_1, τ_2 and relative intensities I_1, I_2. Any attempt to separate additional components in the measured spectra close to theoretically predicted values resulted in increases of chi-squared value or unphysical (*e.g.* negative) intensity values. Based on the presence of only one defect type, the one defect trapping model was used to calculate experimental bulk lifetimes [185].

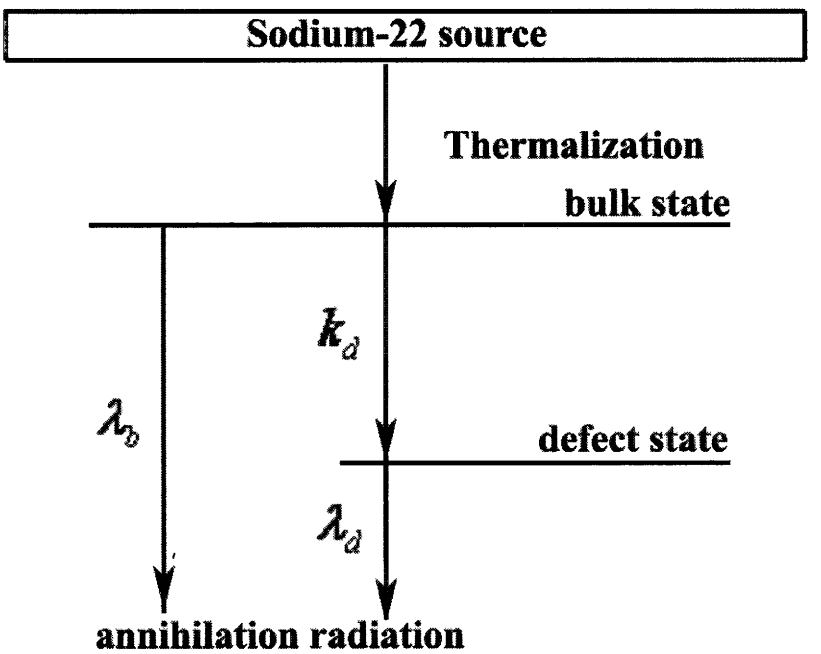

Figure 6.2 One defect trapping model [184].

According to the one defect trapping model (Fig.5.2), after thermalization at $t = 0$ the positron can exist in only one state, which is bulk state. From this state the positron can either annihilate or be trapped. The rate of positron trapping in vacancy defects depends on the defects' concentration and results in reduction of the

experimentally observed bulk lifetime (the so-called reduced bulk lifetime τ_1). In this case the bulk lifetime can be found as:

$$\tau_b = \left(\frac{I_1}{\tau_1} + \frac{I_2}{\tau_2}\right)^{-1} \tag{6.11}$$

Here I_1 and I_2 are the probabilities of a positron to be annihilating from the delocalized bulk or localized defect states, respectively, and τ_1 and τ_2 are the reduced bulk and defect lifetimes.

6.7 Conductivity measurements

The formation of the 1:1 ordered structure in perovskite oxides containing a 1:2 ratio of the B-site cations was explained based on "random site" or "space charge" models. The former model assumes the formation of a homogeneous "uncharged" material, while the latter assumes the appearance of oxygen defects that can change the electrical characteristics of the material. In the present research, we are interested in the relative changes in conductivity (but not in the absolute values) with nonstoichiometry. DC conductivity measurements were done at elevated temperatures (20-430°C) by placing furnace-heated samples in a quartz tube filled with argon. The temperature was controlled by a platinum thermocouple positioned 5mm from the sample. In order to avoid formation of a Schottky barrier on the interface, metal-dielectric silver paste was deposited on the surface of samples, followed by annealing at 500°C. Formation of ohmic contacts was confirmed by measuring the current-voltage characteristics of the

studied materials at high temperatures. To eliminate the influence of sample geometry, specimens of the same dimensions were cut from the sintered samples.

6.8 Optical characterization

Optical characterization of perovskite oxides was performed by means of the Raman technique and photoluminescence spectroscopies. Optical measurements involved registration of reflected/scattered light that constituted a small portion of an incident signal. For optical characterizations, surfaces of materials were polished to enhance intensities of the reflected/scattered signal.

6.8.1 Photoluminescence measurements

For photoluminescence (PL) measurements, a He-Cd laser (Kimmon Electric Co, Ltd.) with 325nm light was used as a pump source. The PL signal from samples was collected by a pair of achromatic lenses and transmitted to a spectrometer through a multimode step index optical fiber (Ocean Optics, model QP600-2-VIS-NIR). The spectrum was analyzed in a spectrometer (Ocean Optics, S2000) consisting of a grating and an array CCD detector. The grating had 600 lines/mm and provided a large spectral window (~350÷1000nm). The PL signals of perovskite samples were normalized by using a spectrometer calibration curve obtained by measuring the output of a lamp of standard irradiance (Ocean Optics, LS-1-CAL).

6.8.2 Raman measurements

Raman measurements were done at room temperature on a Renishaw 2000 spectrometer by using a 514nm Ar^+ ion laser with 25mW output power as an excitation source. Laser light was focused on the surface of the sample through objectives with different magnifications. The choice of the objective was based on the area of the sample used to collect the signal. Because of the presence of secondary phases found dispersed in some samples, the objective with the highest magnification (50x, lowest light spot on the surface of the sample) was chosen in order to collect data from the area adjacent to secondary phases and eliminate the signal from the secondary phases themselves. The scattered signal constituted a small fraction of the incident laser light. The presence of a filter used to separate the signal from the sample from that of the laser limited the spectral range of systems at lower frequencies. During measurements, the intensity of the low energy mode at approximately $100cm^{-1}$ was significantly reduced in comparison to the literature data. Prior to every set of measurements, the system was calibrated by using a silicon crystal with a Raman line at $520.5cm^{-1}$.

Chapter 7

Crystallographic Characterization of Nonstoichiometric $Ba(B'_{1/3}Nb_{2/3})O_3$ (B' = Co or Zn) Materials

7.1 Some aspects of the synthesis of nonstoichiometric perovskite oxides

One of the goals of the present research is to study the influence of nonstoichiometry at cation sites in $Ba(B'_{1/3}Nb_{2/3})O_3$ (B' = Co or Zn) perovskites on the 1:2 ordering process and ceramic densification. Solid state sintering of oxides having perovskite structure can be accomplished by either mixing of metal oxides with barium carbonate and sintering of the perovskite precursor, or by taking advantage of the so-called columbite method described in the experimental section (Chapter 6) that involves sintering of the intermediate columbite phase. In spite of the apparent simplicity of the direct first method that avoids double sintering, and as a result reduces processing time, it has been reported that the direct sintering route produces a number of secondary phases (e.g. in the case of the sintering of $Ba_3MgTa_2O_9$ perovskite, formation of secondary phases like $Ba_4Ta_2O_9$, $Ba_3Ta_5O_{15}$, and $Ba_5Ta_4O_{15}$ has been reported [192]). The presence of several metal oxides makes some alternative reaction pathways possible. For example, the following reactions can occur:

$$5BaO + 2Ta_2O_5 \rightarrow Ba_5Ta_4O_{15} \quad (7.1)$$

$$3BaO + Ba_5Ta_4O_{15} \rightarrow 2Ba_4Ta_2O_9 \quad (7.2)$$

These phases appear at low temperatures and remain stable in a large temperature range, impeding the formation of a single-phase perovskite structure and reducing the microwave quality factor [192]. In order to eliminate the presence of "extra" phases, prolonged heating at high temperatures exceeding 1400°C is required. Lee *et al* [170] employed the direct sintering method of perovskite precursors with a double-calcination procedure. Increased homogeneity resulted from the regrinding of the perovskite precursor after the first calcination and significantly enhanced the 1:2 ordering process in comparison to the single-calcinated samples.

Application of the columbite route that involves mixing of barium carbonate with the already sintered columbite phase allows the formation of a single-phase material with superior microwave properties through avoiding alternative reaction pathways and stabilization of volatile components (like Zn atom) during low temperature columbite sintering [121, 194]. In order to separate the influence of secondary phases as a result of the deviation from the stoichiometric composition on cation sites from those that appeared because of the availability of several reaction pathways during the sintering process, the columbite preparation method was employed to produce perovskite materials in the present research.

7.2 $Ba_3Co_{1+y}Nb_2O_9$ perovskites

The XRD patterns of cobalt perovskite samples prepared by using 500-800kg/cm^2 pressures during the pressing of the perovskite precursor powder and sintered at 1470°C with the nonstoichiometry on the cobalt site are presented in Fig.7.1. As revealed by

XRD analysis, the stoichiometric composition of BCN perovskite represents a single-phase material. According to the measured XRD pattern, a sample containing an excess of cobalt (1+y = 1.03) has the same phase composition as the stoichiometric sample. Within the sensitivity of the experimental apparatus used, no evidence of the formation of an "extra" phase was found. The decrease in the cobalt content from the

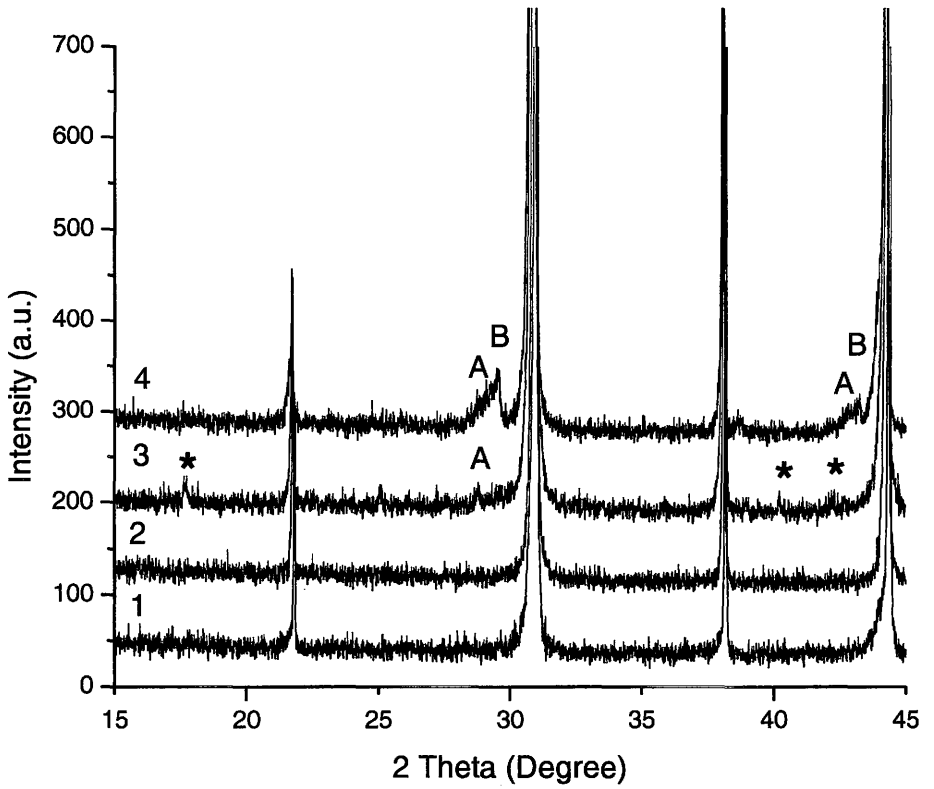

Figure 7.1 XRD patterns of $Ba_3Co_{1+y}Nb_2O_9$ perovskites prepared by applying 500-800kg/cm^2 pressures during the perovskite stage and sintered at 1470°C. 1) 1+y = 1.03, 2) 1+y = 1, 3) 1+y = 0.93, 4) 1+y = 0.85. *- 1:2 ordered structure, A- $Ba_5Nb_4O_{15}$, B- $Ba_8CoNb_6O_{24}$.

nominal value results in the appearance of a number of additional diffraction peaks. Samples with small barium deficiencies (1+y = 0.93) revealed the formation of the 1:2

ordered phase (characterized by the presence of the XRD peak at $2\theta = 17.76°$) and the appearance of peaks ascribed to the appearance of the Nb-rich $Ba_5Nb_4O_{15}$ phase. Further reduction in the cobalt content ($1+y = 0.85$) results in an increase in the concentration of

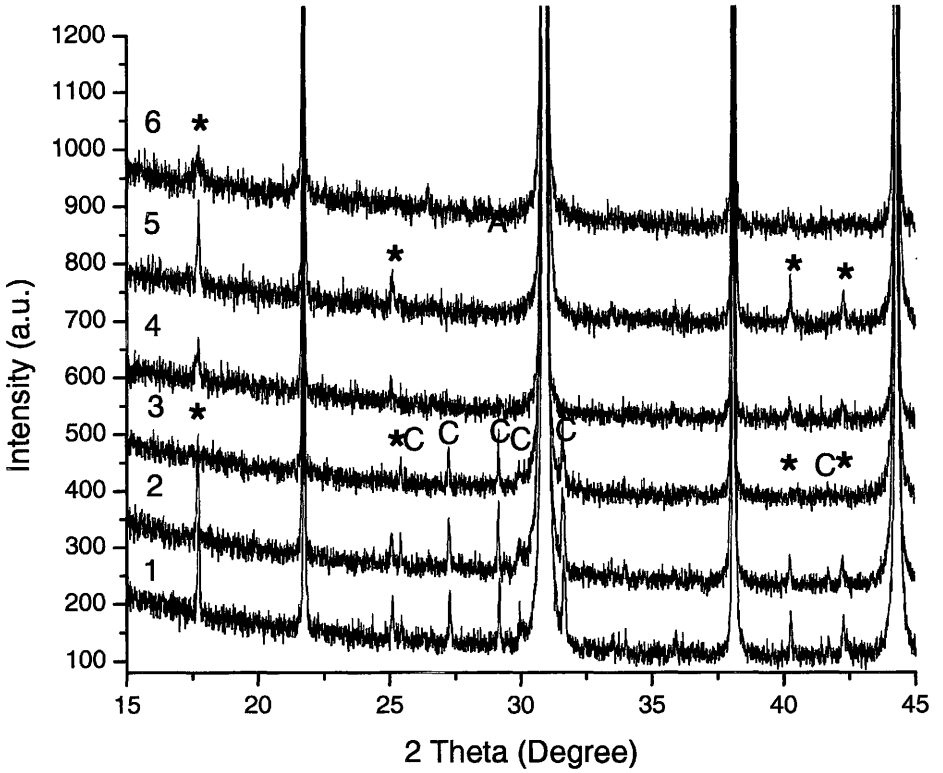

Figure 7.2 XRD patterns of $Ba_3Co_{1+y}Nb_2O_9$ perovskites prepared by applying 1200kg/cm^2 pressures during the perovskite stage and sintered at the 1300-1500°C temperature range. 1) $1+y = 1.03$, 1300°C, 2) $1+y = 1.03$, 1400°C, 3) $1+y = 1.03$, 1500°C, 4) $1+y = 1$, 1300C°, 5) $1+y = 1$, 1400C°, 6) $1+y = 1$, 1500C°. *- 1:2 ordered structure, C- $Ba_6CoNb_9O_{30}$.

the $Ba_5Nb_4O_{15}$ phase and the appearance of XRD lines attributed to the cobalt deficient (in comparison to the main material) $Ba_8CoNb_6O_{24}$ phase. The formation of secondary phases in the samples with large cobalt deficiencies ($1+y = 0.85$) is paralleled by the disappearance of the 1:2 ordered structure.

Fig.7.2 presents XRD patterns of $Ba_3Co_{1+y}Nb_2O_9$ perovskites prepared under 1200kg/cm^2 pressures during the pressing of the perovskite precursor powder and sintered at different temperatures. Modification in the preparation process through the introduction of different degrees of strain in the matrix produces different driving forces for the growth of the perovskite structure (Section 5.1.1). The influence of the different driving forces during sintering on the microstructure and optical properties of perovskites will be considered in subsequent chapters. XRD patterns of samples having higher strain before sintering are characterized by the appearance of additional lines in samples with excess of cobalt (1+y = 1.03) attributed to the Nb-rich $Ba_6CoNb_9O_{30}$ phase. In contrast to the low strain samples, high strain samples with a stoichiometric composition and those containing cobalt in excess demonstrate the presence of the 1:2 ordered phase. Intensities of the XRD peaks in both the 1+y = 1 and 1+y = 1.03 sets of samples originating from the ordering process are a maximum at 1400°C and decrease with increasing sintering temperature, indicating that the 1:2 ordered structure remains thermodynamically stable below some temperature T_{trans} and changes its symmetry by sintering at temperatures T > T_{trans}. The observed order-disorder transition temperature (T_{trans} ~ 1400°C) is in agreement with that reported in [15]. By comparing the stoichiometric composition of the BCN perovskite prepared by inducing low and high strains, one can notice that the high strain sample sintered at 1500°C still demonstrates the presence of cation ordering in spite of a slightly larger sintering temperature (1470°C *vs.* 1500°C), in comparison to the low strain sample. Thus, changes in the initial system energy stored in the strained

material that influence the diffusion of atoms and grain growth also modify the microstructure of ceramics, facilitating an ordering process.

Fig.7.3 shows relative changes in the integrated intensity of the most intense XRD peak originating from the presence of the $Ba_6CoNb_9O_{30}$ phase *vs* different sintering temperatures.

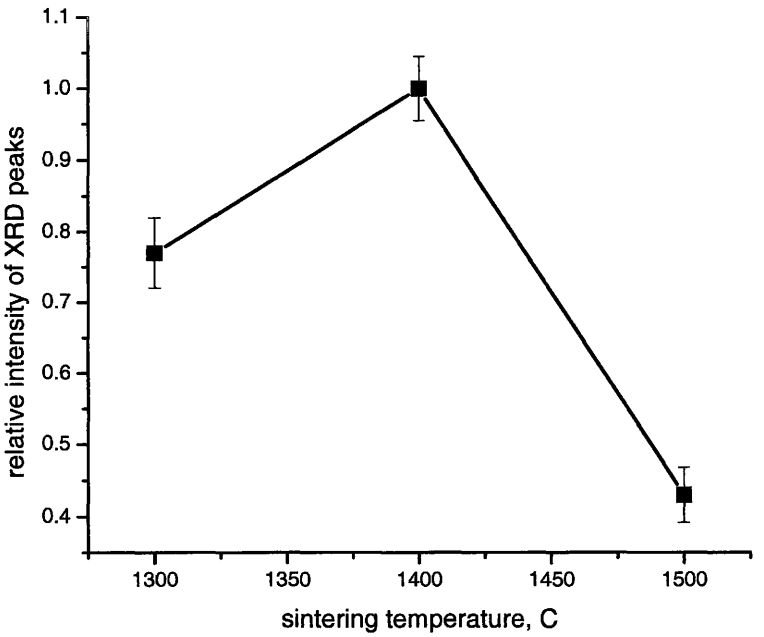

Figure 7.3 Relative intensity of XRD peaks originating from the $Ba_6CoNb_9O_{30}$ phase found in $Ba_3Co_{1+y}Nb_2O_9$ perovskites containing excess cobalt *vs* sintering temperature.

The intensity of the X-ray diffraction peaks of the $Ba_6CoNb_9O_{30}$ phase increases for the samples sintered at 1400°C and decreases towards high temperature sintered samples (1500°C). It is worth to note that formation of the 1:1 ordered phase found in the family of perovskite materials having a 1:2 mixture of the B-site cations [*e.g.* 53, 75] is characterized by doubling of the primitive cubic unit cell and appearance of a low angle

XRD peak from the [111] plane at $2\theta = 19°$. Close examination of the obtained X-ray diffraction patterns did not reveal any evidence of 1:1 B-site cation ordering. This may be the case because of the small size of the 1:1 ordered domains caused by the charge imbalance within a unit cell [27] that makes X-ray diffraction techniques insensitive to the present type of cation order.

In summary, reduction in the Co content from the nominal, stoichiometric value is accompanied by the formation of the 1:2 ordered phase, the amount of which is defined by the order-disorder transition temperature and the initial strain present in the matrix. The dependence of the intensities of the XRD peaks from the ordered structure on the preparation history of the samples indicates the influence of the microstructure of samples on the ordering process. Further decreases in the amount of cobalt result in the formation of cobalt deficient phases and the disappearance of the ordered structure.

7.2.1 Secondary phases

The $Ba_5Nb_4O_{15}$ phase, having the same space group as the 1:2 ordered structure (i.e. P-3m1), belongs to the group of $A_nB_{n-1}O_{3n}$ perovskites with n = 5 and represents infinite layers of corner sharing NbO_6 octahedra with n-1 thickness, followed by the ordered arrangement of cation vacancies (Fig.7.4) [195]. The reported crystallographic data indicates that Ba-O bonds inside of the layers are significantly compressed and Nb-O bonds are stretched, demonstrating discrepancy in the ionic radii of cations composing the structure. The presence of the layer with cation vacancies significantly distorts

coordination spheres around both Nb and Ba cations, relieving strain in cation-anion bonds.

The $Ba_8CoNb_6O_{24}$ material has been reported to be comprised of a layered structure with the same space group (P-3m1) as the $Ba_5Nb_4O_{15}$ material, but in contrast to this material, the $Ba_8CoNb_6O_{24}$ structure is formed by the ordered arrangement of seven layers of corner-sharing BO_6 octahedra followed by a face-shared layer occupied by cation vacancies (Fig.7.5) [196]. The presence of different cations with dissimilar ionic radii produces stresses and strains in cation-anion bonds that are relieved near the layer containing cation vacancies.

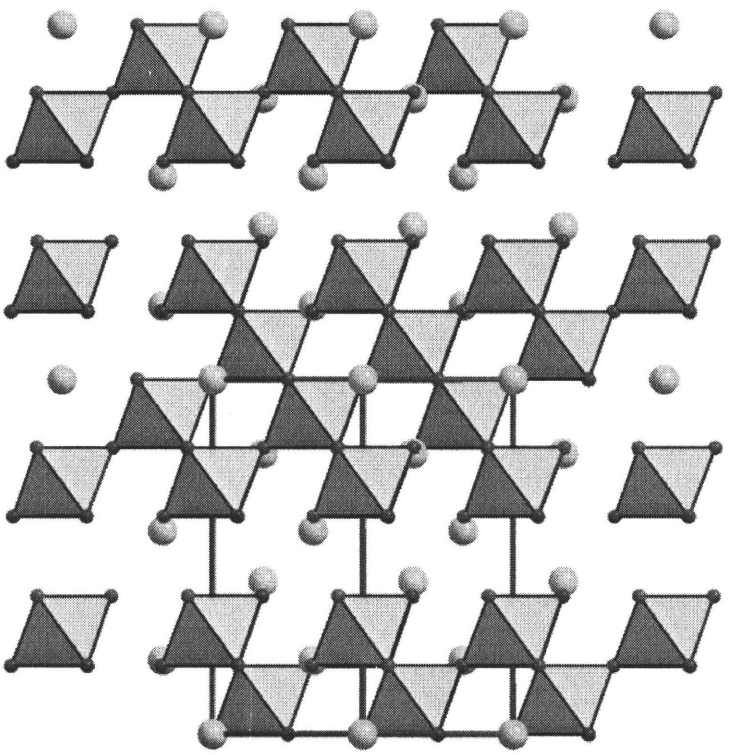

Figure 7.4 The structure of $Ba_5Nb_4O_{15}$ viewed along the [110] direction. The filled octahedra four layers thick and occupied by Nb^{5+} cations are followed by a face-shared layer containing cation vacancies.

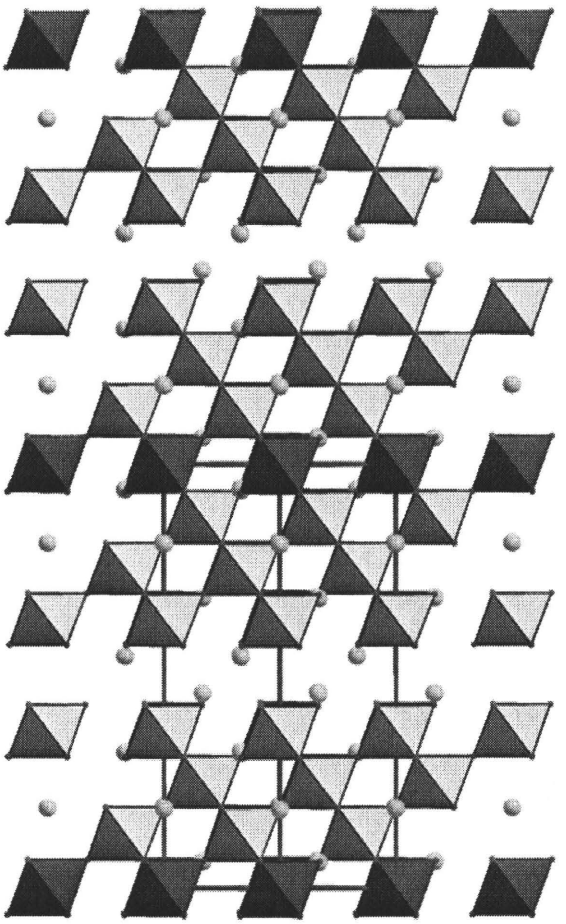

Figure 7.5 The structure of $Ba_8CoNb_6O_{24}$ viewed along the [110] direction. Cobalt and niobium containing octahedra are shown in dark gray and light gray, respectively. The seven-layer thick slab is followed by the face-shared layer of oxygen octahedra occupied by cation vacancies.

The $Ba_6CoNb_9O_{30}$ phase found in the present research in highly strained nonstoichiometric materials has the tungsten-bronze-type structure with the P4bm space group [197]. Table 7.1 shows the atomic fraction of atoms composing the main material, as well as secondary phases found in perovskite systems. According to Table 7.1, $Ba_6CoNb_9O_{30}$ contains an excess of niobium cations in comparison to the main phase and low concentrations of barium and cobalt ions. $Ba_5Nb_4O_{15}$ and $Ba_8CoNb_6O_{24}$ are both

deficient in cobalt and have slightly larger concentrations of niobium than the main material.

Table 7.1. Theoretically calculated atomic fractions (%) of elements composing stoichiometric perovskite oxides and secondary phases found in nonstoichiometric systems.

	Ba	Co	Nb	O
$Ba_3CoNb_2O_9$	20.0	6.6	13.3	60.0
$Ba_6CoNb_9O_{30}$	13.0	2.1	19.5	65.2
$Ba_5Nb_4O_{15}$	20.8	---	16.6	62.5
$Ba_8CoNb_6O_{24}$	20.5	2.5	15.3	61.5

7.3 $Ba_{3+3x}CoNb_2O_9$ perovskites

During research on two sets of samples prepared by inducing low and high strains on the perovskite precursor powder, no difference (except for the stronger X-ray diffraction peaks originating from the 1:2 ordered structure in the highly strained samples) in phase compositions between samples with the same stoichiometry was found. XRD patterns of cobalt perovskites with nonstoichiometry on the Ba-site prepared by inducing larger strain and sintered at 1500°C are presented in Fig.7.6. The sample containing an excess of barium cations (3+3x = 3.015) contains small traces of a

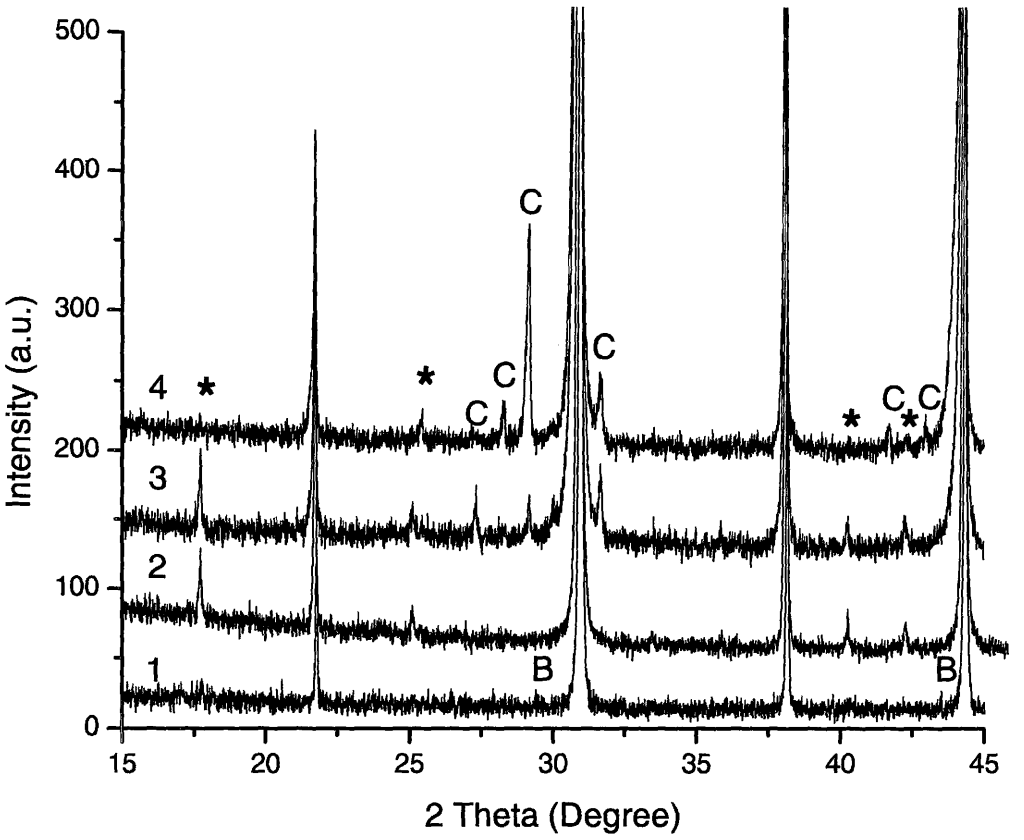

Figure 7.6 XRD patterns of $Ba_{3+3x}CoNb_2O_9$ perovskites prepared by applying 1200kg/cm^2 pressure during the perovskite stage and sintered at 1500°C. 1) 3+3x =3.015, 2) 3+3x = 3, 3) 3+3x = 2.94, 4) 3+3x = 2.7. *- 1:2 ordered structure, B-$Ba_8CoNb_6O_{24}$, C-$Ba_6CoNb_9O_{30}$.

secondary phase that were attributed to the $Ba_8CoNb_6O_{24}$ structure. The stoichiometric sample is characterized by the absence of any evidence of secondary phase formation and the appearance of X-ray diffraction peaks from the 1:2 ordered structure. Reduction in the Ba content results in the intensification of superstructure diffraction peaks, the intensity of which is at a maximum for 3+3x = 2.94 and reduces with further deviation of Ba content from the nominal value. For 3+3x = 2.7, no evidence of the ordered structure was found. An intermediate value of nonstoichiometries on the Ba-site (3+3x = 2.94) that is

characterized by the strongest X-ray diffraction peaks from the ordered structure results in formation of the tungsten-bronze-type $Ba_6CoNb_9O_{30}$ phase, the concentration of which increases with further deviation from the stoichiometry.

Deviation from the stoichiometry in $Ba_{3+3x}CoNb_2O_9$ perovskites toward negative x values (that is, introduction of barium deficiencies) leads to the formation of the 1:2 ordered phase and the simultaneous appearance of small traces of the tungsten-bronze structure. An increase in the concentration of the $Ba_6CoNb_9O_{30}$ phase with further deviation from stoichiometry results in the disappearance of the ordered arrangement of the B-site cations.

7.4 $Ba_3Zn_{1+y}Nb_2O_9$ perovskites

The influence of nonstoichiometry on the Zn-site in $Ba_3Zn_{1+y}Nb_2O_9$ perovskites is analogous to the cobalt system. The samples sintered at 1445°C and containing an excess (1+y = 1.005) or nominal composition of Zn form single-phase material with a disordered arrangement of cations on the B-site (Fig.7.7). In contrast to the cobalt system where an intermediate value of the nonstoichiometry on the cobalt sublattice produced X-ray diffraction peaks from the ordered structure and small traces of the $Ba_5Nb_4O_{15}$ phase, the zinc system revealed the formation of a large amount of the $Ba_5Nb_4O_{15}$ material and a phase isostructural to $Ba_8CoNb_6O_{24}$. No evidence of the ordering process was found.

In order to check for the influence of the zinc-deficient secondary phases resulting from the volatility of ZnO during the preparation process and the order-disorder phase transition temperature that is on the order of 1380°C [131], two sets of samples were

prepared by applying higher formation pressures and sintering at temperatures above the order-disorder transition temperature, by covering perovskites in their own powder or

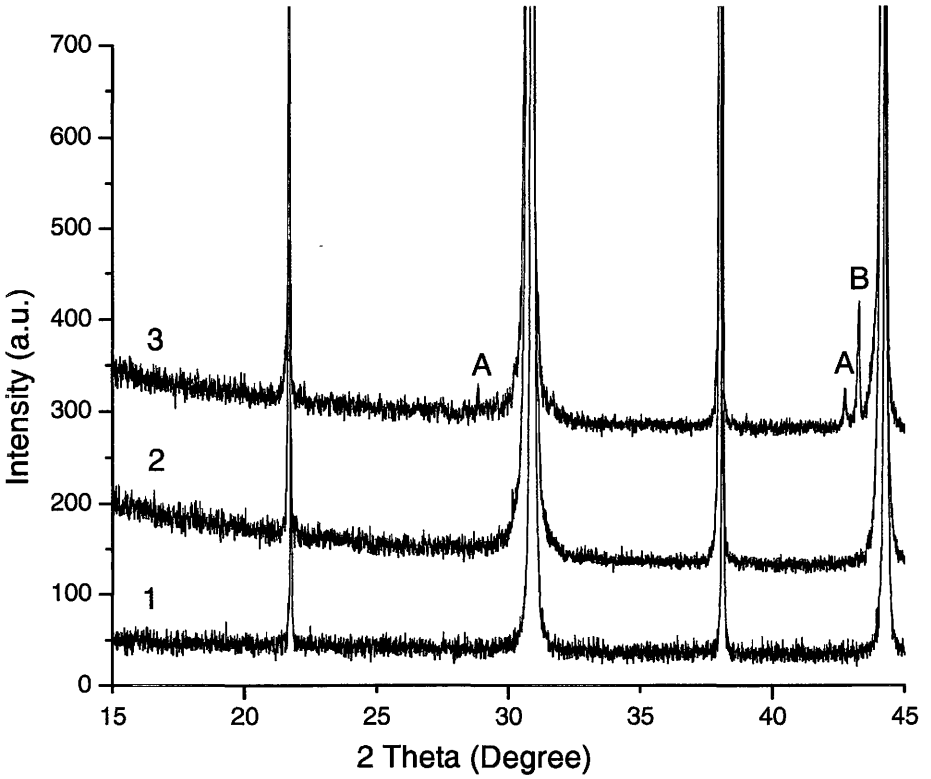

Figure 7.7 XRD patterns of $Ba_3Zn_{1+y}Nb_2O_9$ perovskites prepared by applying 500-800kg/cm^2 pressures during the perovskite stage and sintered at 1445°C. 1) 1+y = 1.005, 2) 1+y = 1, 3) 1+y = 0.93. *- 1:2 ordered structure, A- $Ba_5Nb_4O_{15}$, B- $Ba_8ZnNb_6O_{24}$.

without any cover during the sintering process. The results of XRD characterization are shown in Fig.7.8. As one could expect, sintering of "unsealed" zinc-containing perovskites resulted in significant zinc loss and formation of the zinc-deficient $Ba_8ZnNb_6O_{24}$ phase. Simultaneously, the appearance of a phase with lower (in comparison to the main material) zinc content led to the disappearance of the XRD peaks originating from the 1:2 cation ordering process.

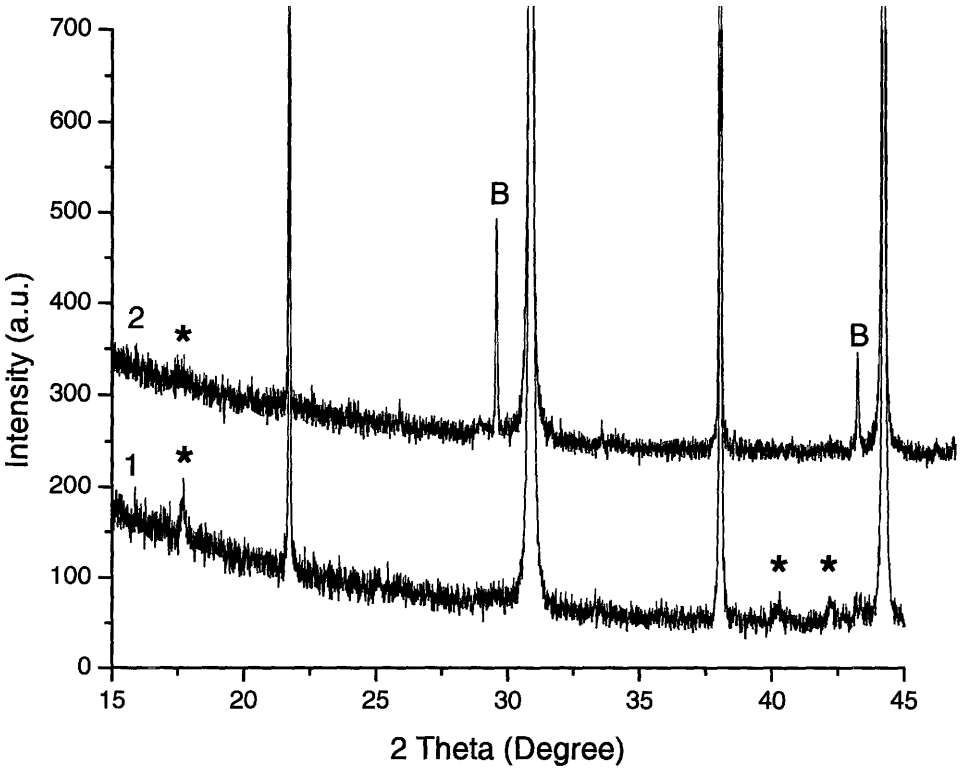

Figure 7.8 XRD patterns of $Ba_3ZnNb_2O_9$ perovskites prepared by applying 1200kg/cm^2 pressure during the perovskite stage. 1) covered in perovskite powder, 2) uncovered. *- 1:2 ordered structure, B- $Ba_8ZnNb_6O_{24}$.

7.5 $Ba_{3+3x}ZnNb_2O_9$ perovskites

Deviation from the nominal value on the Ba-site in $Ba_{3+3x}ZnNb_2O_9$ perovskites (Fig.7.9) results in the formation of the 1:2 ordered structure (3+3x = 2.985), the amount of which decreases with further reduction in the Ba content (3+3x = 2.94) and the appearance of the tungsten-bronze type $Ba_6ZnNb_9O_{30}$ phase. Similar to the cobalt system with barium nonstoichiometry, the formation and increase in the concentration of the $Ba_6ZnNb_9O_{30}$ structure leads to the reduction in cation ordering on the B-sublattice.

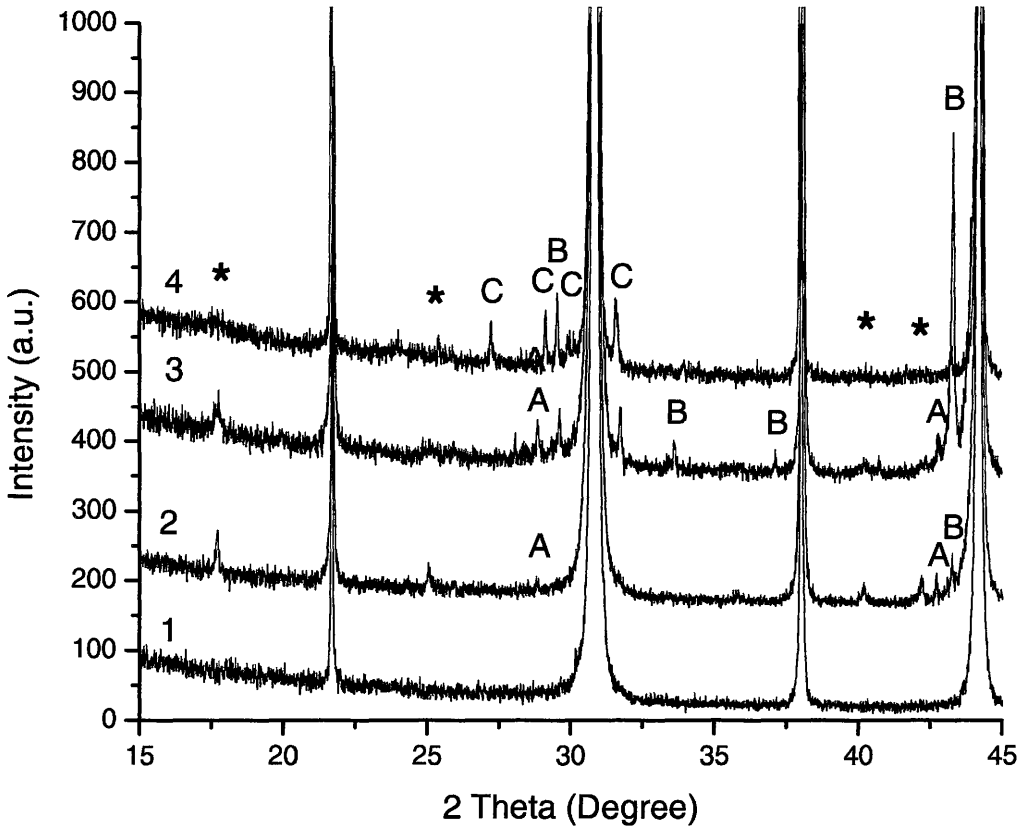

Figure 7.9 XRD patterns of $Ba_{3+3x}ZnNb_2O_9$ perovskites prepared by applying 500-800kg/cm^2 pressures during the perovskite stage and sintered at 1445°C. 1) 3+3x = 3, 2) 3+3x = 2.985, 3) 3+3x = 2.94, 4) 3+3x = 2.7. *- 1:2 ordered structure, A- $Ba_5Nb_4O_{15}$, B- $Ba_8ZnNb_6O_{24}$ C- $Ba_6ZnNb_9O_{30}$.

Evaporation of zinc oxide from the surface results in the formation of the Zn-deficient secondary phases. The cation ordering process observed at small values of Ba-nonstoichiometries is paralleled by the appearance of the $Ba_5Nb_4O_{15}$ phase. The concentration of this Zn-free phase increases towards lower values of the barium amount. For 3+3x = 2.94, the considered perovskites also contain some amount of the $Ba_8ZnNb_6O_{24}$ material.

7.6 Positron lifetime spectroscopy

Results of theoretical calculations reported in [184,198] for the bulk and defect lifetimes in $Ba_3BNb_2O_9$ (B=Mg, Co or Zn) perovskite structures are presented in Table 7.2.

Table 7.2 Theoretically calculated bulk and defect (vacancy) lifetimes in $Ba_3BNb_2O_9$ perovskites.

Material	$Ba_3MgNb_2O_9$	$Ba_3MgNb_2O_9$	$Ba_3CoNb_2O_9$	$Ba_3ZnNb_2O_9$
Space group	*Pm-3m*	*P3m1*	*Pm-3m*	*Pm-3m*
τ_b, ps	195	237	194	193
τ_{Ba}, ps	321		322	321
τ_B, ps	264		264	260
τ_{Nb}, ps	265		265	262
τ_O, ps	197		195	194

According to simulations described in [184,198] the presence of Ba-vacancies in the disordered phase will give a defect lifetime of 320*ps*. The introduction of B-site vacancies will result in a lifetime component around 260*ps*. From the decomposed experimental spectra the so-called "reduced" bulk lifetime component and a component arising from the annihilation in defects were observed. Typical values of the reduced and defect lifetimes as well as their relative intensities for stoichiometric compositions of $Ba_3BNb_2O_9$ oxides (B=Mg, Zn or Co) are presented in Table 7.3. Ceramic materials considered here consist of grains having intergranular spaces. Grain boundaries represent

Table 7.3 Experimentally observed positron lifetimes and intensities for stoichiometric $Ba_3BNb_2O_9$ perovskites.

	$Ba_3MgNb_2O_9$	$Ba_3CoNb_2O_9$	$Ba_3ZnNb_2O_9$
τ_1, ps	178±1	164±1	204±2
τ_2, ps	336±5	294±5	355±7
$I_1, \%$	75±2	71±2	74±2
$I_2, \%$	25±1	29±1	26±2

regions in samples with reduced electron density. The latter component, with intensities of 24-40% for different stoichiometric and non-stoichiometric $Ba_3BNb_2O_9$ perovskites (B=Mg, Zn or Co) and lifetime values of around $300ps$, was attributed to positrons annihilating inside of intergranular spaces. Variations in the values of the defect lifetimes and their probabilities can be related to the difference in the ceramics' microstructure. The results of the X-ray measurements demonstrated formation of $Ba_5Nb_4O_{15}$ and $Ba_8BNb_6O_{24}$ secondary phases containing ordered arrangement of B-site cation vacancies. Any attempt to separate additional components (including those having lifetime values corresponding to the theoretically predicted defect lifetimes in case of the formation of B-site cation vacancies) in the experimental lifetime spectra did not give physically meaningful lifetime values. This probably indicates that either the concentration of the point defects is so small that it is beyond the sensitivity of the setup used in the present studies or the resolution of the experimental setup is not sufficient to

separate closely spaced components. This fact validates the application of the one defect trapping model described in the experimental section.

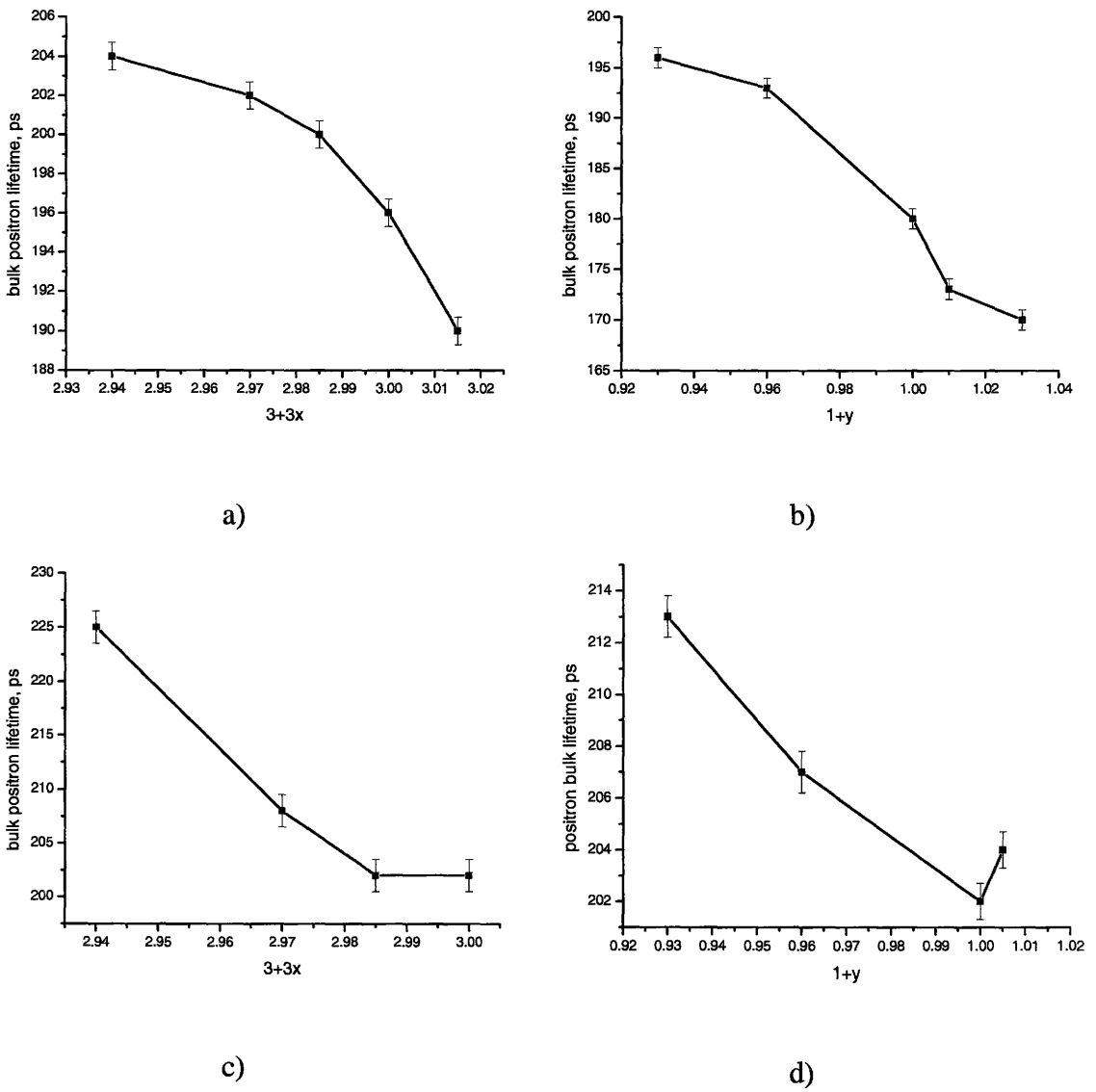

Figure 7.10 Dependence of the positron bulk lifetime on the cation composition in $Ba_{3+3x}B_{1+y}Nb_2O_9$. a) $Ba_{3+3x}CoNb_2O_9$, b) $Ba_3Co_{1+y}Nb_2O_9$, c) $Ba_{3+3x}ZnNb_2O_9$, d) $Ba_3Zn_{1+y}Nb_2O_9$.

The dependence of the positron bulk lifetime on the value of nonstoichiometry for perovskite materials prepared by applying low pressure (500-800kg/cm^2) is presented in Figure 7.10.

The preceding sections demonstrated that deviation from stoichiometry results in the appearance of secondary phases that according to [184,198] have bulk lifetime values significantly exceeding the corresponding lifetime values of the main material. In particular, the expected bulk lifetime for $Ba_6BNb_9O_{30}$ material is 353*ps*. The calculated positron bulk lifetime in $Ba_5Nb_4O_{15}$ structure is 426*ps*. $Ba_8BNb_6O_{24}$ is anticipated to produce lifetimes longer than that of the main material.

7.7 Discussion

Deviation from the stoichiometry on the Ba- and B- (B = Co or Zn) sites results in the appearance of several Ba- and B-site deficient phases and changes in the cation ordering degree. The appearance of the cation deficient phases for some of the compositions can be described by the following reactions:

$$100Ba_3B_{0.93}Nb_2O_9 \rightarrow 90Ba_3BNb_2O_9 + 6Ba_5Nb_4O_{15} \quad (7.3)$$

$$100Ba_3B_{1.03}Nb_2O_9 \rightarrow 98Ba_3BNb_2O_9 + Ba_6BNb_9O_{30} \quad (7.4)$$

$$100Ba_{2.94}BNb_2O_9 \rightarrow 94Ba_3BNb_2O_9 + 2Ba_6BNb_9O_{30} \quad (7.5)$$

$$100Ba_{3.015}BNb_2O_9 \rightarrow 96.5Ba_3BNb_2O_9 + 1.5Ba_8BNb_6O_{24} \quad (7.6)$$

The formation of secondary phases in nonstoichiometric perovskite oxide can be understood based on the tolerance of the perovskite structure to different cation substitutions. $Ba_3BNb_2O_9$ perovskites having the Pm-3m space group and disordered

cation arrangements on the B-sublattice have cubic unit cells formed by Ba^{2+} cations located at the corners of the cell, O^{2-} anions positioned at the faces, and B^{2+}/Nb^{5+} cations randomly occupying the center of the cell in the 1:2 ratio. The tolerance factor defined as $t = (R_A + R_O)/\sqrt{2}(R_B + R_O)$ for the ABO_3 structure shows geometrical compatibility of different ions. For the considered perovskite materials the tolerance factor is 1.025 (BCN) and 1.027 (BZN) and shows the presence of the oversized A cation and undersized B cations. Introduction of an extra Ba^{2+} (with ionic radius R_i = 1.61Å) or B^{2+} (with ionic radius R_i = 0.745Å for Co^{2+} and 0.74Å for Zn^{2+}) is energetically unfavorable because of the close packing of the structure. The presence of an excess of cations can be accommodated only by expansion of the unit cell. So, the introduction of cations above the stoichiometric amount leads to precipitation and formation of secondary phases described by equations (7.4) and (7.6). For the studied values of nonstoichiometries, the amount of secondary phases is limited to only several percent. Introduction of vacancies on the cation sites shortens the effective ionic radii of cations, changing the value of the tolerance factor. In particular, for the BCN perovskite with 1+y = 0.85 or 3+3x = 2.7, the tolerance factor is equal to 1.044 and 0.97, respectively. The upper limit of the tolerance factor approaches the value of 1.06, above which no stable perovskite structure can exist as has been pointed out by Zhang *et al* [86]. Decreasing *t* below unity should inevitably result in structure destabilization and rotation of oxygen octahedra [83,84]. Values of the tolerance factor obtained for the studied stoichiometries of perovskites are much different than unity, and on the verge of the range defining stability of the perovskite structure. Stabilization for the large values of nonstoichiometries is achieved by precipitation of

excess of ions from the main phase and the formation of secondary phases described by equations (7.3) and (7.5). Intermediate values of nonstoichiometries can be accommodated by changing the local anion environment.

As has been demonstrated by the results of the XRD measurements, deviation from stoichiometry involving cation deficiencies is accompanied by the B-site cation ordering process, the degree of which depends on the appearance of secondary phases. Formation of the ordered structure requires exchange of the B-site cation between two crystallographically equivalent positions. In order for the two cations to diffuse between two crystallographic sites they have to overcome the repulsive potential of Ba^{2+} forming a lattice cage and the repulsive potential of each other. The cation diffusion process involving "swapping" of two ions can be significantly enhanced by either introduction of vacancies on the B-site or distortion of the periodical potential formed by barium ions.

Positron lifetime spectroscopy being sensitive to the presence of point defects [185] failed to reveal formation of cation vacancies in $Ba_3BNb_2O_9$ materials due to the complex nature of the latter. Variations in the experimentally observed bulk lifetimes with nonstoichiometries (Fig. 7.10 a-d) are due to the change in concentration of secondary phases as well as disorder-1:2 order phase transition. For example, introduction of deficiencies on the Ba-site results at first in the formation of the 1:2 ordered phase (having bulk lifetime longer than the disordered structure: ~240*ps vs* ~195*ps*) that gives place to $Ba_6BNb_9O_{30}$ secondary phase (353*ps)* with further reduction in the amount of barium. An interesting aspect is the observed decrease of τ_b below the theoretically predicted value for the completely disordered structure (e.g. $Ba_{3.015}CoNb_2O_9$

in Fig. 7.10 a and $Ba_3Co_{1.03}Nb_2O_9$ in Fig. 7.10 b). This decrease below the τ_b of the disordered phase cannot be explained by formation of a secondary phase and will be addressed further in the chapter looking at the variation in microstructure with nonstoichiometry.

Sintering of ceramic materials with a 1:2 ratio of the B-site cations above the order-disorder phase transition temperatures will produce a material with higher density but containing a lower degree of cation ordering. Small values of B-site cation deficiencies caused by a deviation from stoichiometry create vacancies on the B-sublattice. The activation energy of the process that involves cation diffusion towards an empty crystallographic site is significantly less than that requiring "swapping" of two cations between identical crystallographic positions. So, the appearance of the ordered phase was observed at small amounts of B-site cation deficiencies where the tolerance factor is still within stability limits. Large values of nonstoichiometries result in formation of $Ba_5Nb_4O_{15}$ and $Ba_8BNb_6O_{24}$ (B = Co or Zn) phases that contain an ordered arrangement of B-site cation vacancies. An increase in the concentration of B-site deficient phases leads to the reduction of the B-site cation vacancies in the main material available for the cation diffusion degrading diffusion process. In the cobalt system, formation of the cobalt deficient secondary phases starts for a cobalt concentration of 1+y= 0.93 (Fig.7.1), further degrading the ordering process while in zinc perovskites evaporation of zinc oxide produced a significant amount of the zinc deficient phase, suppressing the ordering process (Fig.7.8).

The tolerance factor of a perovskite containing a barium cation on the A-site is greater than unity, indicating the presence of the oversized Ba^{2+} cation that forms the frame of the structure. The introduction of vacancies on the Ba-site distorts the latter, changing periodical repulsive for the lattice potential of the B-site cations. A small value of lattice distortion enhances B-site cation diffusion, leading to the formation of the ordered phase. A decrease in the ordering process is accompanied by the appearance of the $Ba_6BNb_9O_{30}$ (B = Co or Zn) phase that degrades the B-site cation diffusion process. This barium deficient phase has been found in samples with deficiencies on the Ba-site as well as those prepared by applying higher formation pressures prior to sintering, and containing an excess of the B-site cations (Fig.7.2).

Initial energy stored in the strained matrix leads to a larger grain growth rate because of the reduced interface energy between two solids in comparison to the solid-air interface energy and it has been observed from the experiment results in the enhancement of the ordering process. The latter can be explained by formation of lattice imperfections like point defects or dislocations caused by the large growth rate. Fast grain growth leading to a larger degree of the B-site cation ordering can have a deleterious effect on dielectric losses, since it has been predicted by Gurevich and Tagantsev [133] that the presence of lattice defects can induce one-phonon absorption processes at microwave frequencies.

7.8 Conclusions

Deviations from stoichiometry in the studied $Ba_{3+3x}B_{1+y}Nb_2O_9$ perovskites result in structure destabilization and precipitation of cation deficient phases. It has been observed that small values of cation deficiencies enhance the ordering process through introduction of vacant lattice sites on the B-sublattice in materials with nonstoichiometry on the B-site, and a distortion of the repulsive lattice potential caused by the vacant Ba-sites in perovskites with Ba-site nonstoichiometry. The appearance of secondary phases always results in the degradation of the ordering process. In the case of B-site deficient phases, reduction in the ordering process has been ascribed to the formation of the ordered arrangement of the B-site cation vacancies that decrease the overall amount of the B-site cation vacancies within the main material. The influence of the barium deficient phase can be elucidated after considering the changes in the microstructure of the nonstoichiometric materials.

Chapter 8

Microstructure of Ceramics

Sintering of perovskite materials above the transition temperature is often justified by attempts to obtain materials with low porosity and high density. Densification of ceramic materials having a grained structure can be achieved by the elimination of pores present between grains and imperfections in the lattice structure caused by the presence of point defects and defect agglomerations forming voids inside of the grains. The present chapter considers the influence of cation deficient phases found in the nonstoichiometric perovskite oxides on the process of ceramic densification.

8.1 Density of $Ba_{3+3x}B_{1+y}Nb_2O_9$ perovskites

The previous chapter demonstrated that deviation from the stoichiometry results in the appearance of a number of cation deficient phases. The small dimensions of additional phases limit the sensitivity of the XRD technique to their presence. That is why the rigorous determination of phase concentrations from the X-ray diffraction patterns and their influence on the final ceramic density can be inaccurate. Here, we consider the relative change in the density of materials with nonstoichiometry. Typical density variations found in the considered perovskites sintered at low and intermediate temperatures with nonstoichiometries on the B-site are presented in Figure 8.1.

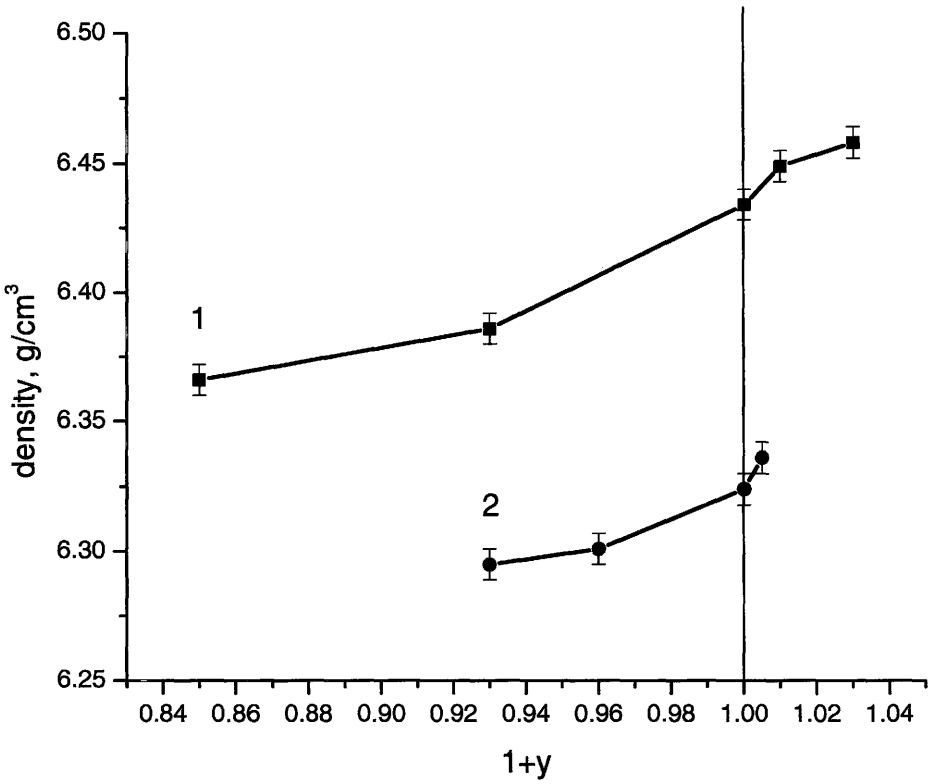

Figure 8.1 Typical changes in the density found by the volumetric method in the $Ba_3B_{1+y}Nb_2O_9$ perovskites prepared by applying 1200kg/cm^2 pressure during the perovskite stage and sintered at the 1300-1400°C temperature range. 1- $Ba_3Co_{1+y}Nb_2O_9$, 2- $Ba_3Zn_{1+y}Nb_2O_9$.

Variation in the amount of the B-site cations results in a gradual decrease in the density from the samples containing an excess of the B-site ions towards the B-site deficient samples (Fig. 8.1). Changes in the monotonic density variation of the B-site nonstoichiometric samples have been found in materials sintered at high temperatures (around 1500°C); perovskites containing an excess of the B-site cation showed a drop in density. Figure 8.2 shows the measured density on the example of the cobalt system for

samples with cobalt concentrations of 1+y = 0.93 and 1.03 and sintered in the 1300-1500°C temperature range.

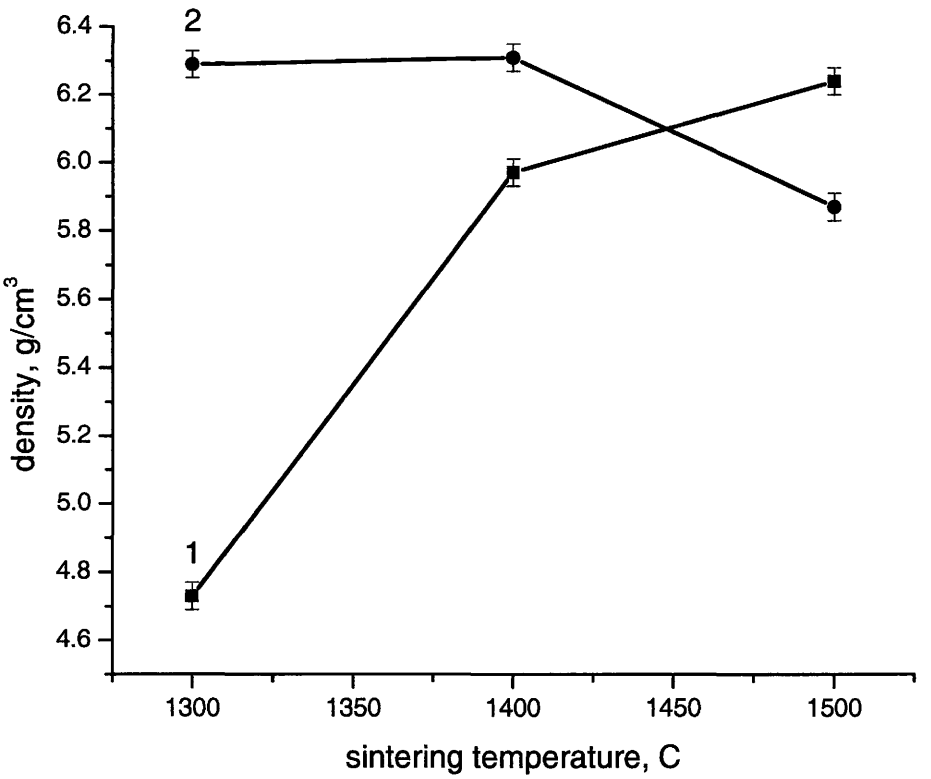

Figure 8.2 Variation in the density measured by the volumetric method of the B-site nonstoichiometric perovskites prepared by applying 1200kg/cm^2 pressure during the perovskite stage with the sintering temperature for: 1-$Ba_3Co_{0.93}Nb_2O_9$, 2-$Ba_3Co_{1.03}Nb_2O_9$

It can be seen from Figure 8.2 that samples containing an excess of the B-site cation and sintered at low and intermediate temperatures have higher densities. By increasing the sintering temperature to 1500°C, the measured density of the B-site rich samples decreases. Samples having deficiencies on the B-site show an increase in the density with sintering temperature.

Variations in the density with the nonstoichiometry on the Ba-site are shown in Figures 8.3 and 8.4. Sintering of ceramics with an excess of Ba^{2+} ions at low and intermediate temperatures always produces low-density materials.

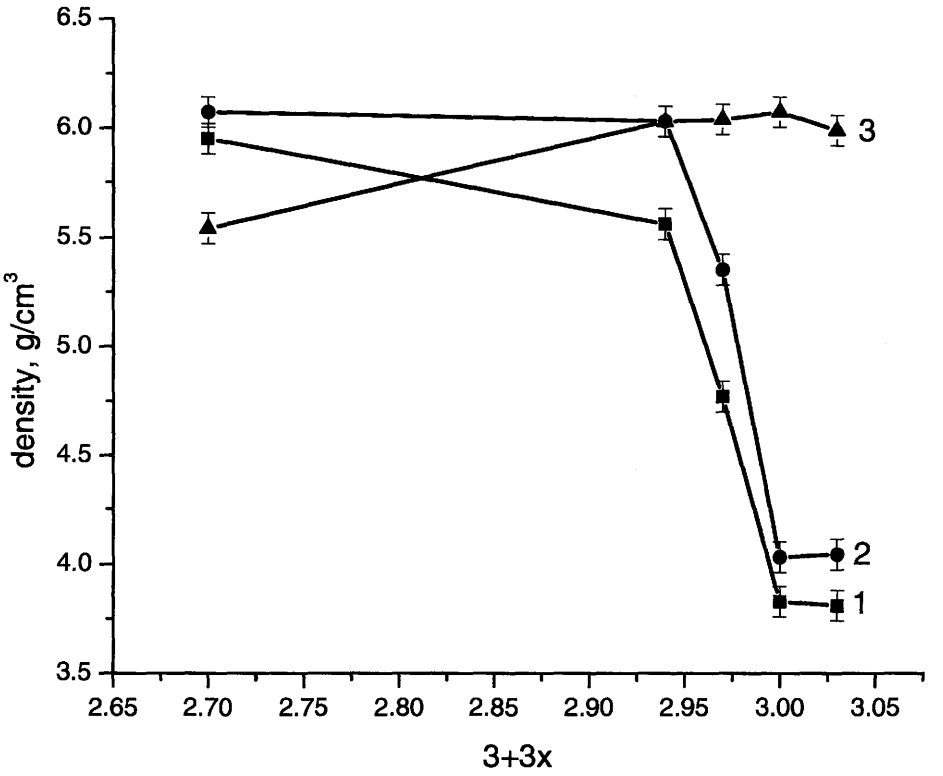

Figure 8.3 Changes in the density measured by the volumetric method of $Ba_{3+3x}CoNb_2O_9$ perovskites prepared by applying 1200kg/cm^2 pressure during the perovskite stage. 1- 1300°C, 2- 1425°C, 3- 1500°C.

When decreasing the barium content, the measured density of ceramics sintered at low and intermediate temperatures increases. Similar to the B-site nonstoichiometric perovskites (Figure 8.2), oxides containing a large amount of Ba-deficiencies and

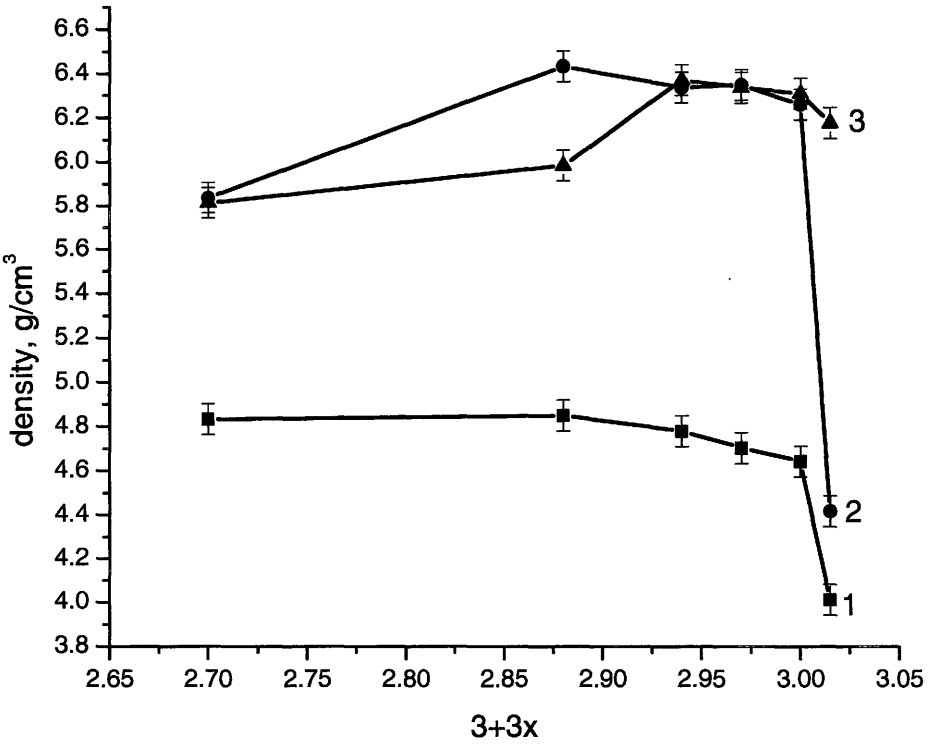

Figure 8.4 Changes in the density measured by the volumetric method of $Ba_{3+3x}ZnNb_2O_9$ perovskites prepared by applying 1200kg/cm^2 pressure during the perovskite stage. 1- 1250°C, 2- 1350°C, 3- 1450°C.

sintered at high temperatures demonstrate a drop in the density (Figures 8.3 and 8.4).

The previous chapter demonstrated that near-stoichiometric compositions represent multiple-phase systems consisting of 1:2 ordered domains within the disordered matrix as well as B- and Ba-site deficient phases. In order to explain the density changes found in the considered oxides, we calculated the densities of the main phase having a disordered cation arrangement, 1:2 ordered structures, and cation deficient secondary phases. Tables 8.1 and 8.2 contain calculated densities and lattice parameters of the main

materials and secondary phases. For the calculation of densities of the disordered cubic phases of $Ba_3BNb_2O_9$ (B = Co, Zn) perovskites, lattice parameters obtained from the measured X-ray diffraction patterns were taken. Because of the weak ordering of the considered perovskite materials, the lattice parameters of the completely ordered 1:2 structures were obtained by SPuDS modeling software [199]. Lattice parameters used for the calculation of the densities of the secondary phases were adopted from ref. [195-197].

Table 8.1 Calculated densities of disordered and completely ordered perovskite materials.

Formula	$Ba_3CoNb_2O_9$	$Ba_3CoNb_2O_9$	$Ba_3ZnNb_2O_9$	$Ba_3ZnNb_2O_9$
Space group	Pm-3m	P-3m1	Pm-3m	P-3m1
a, Å	4.088	5.829	4.070	5.835
b, Å		5.829		5.835
c, Å		7.145		7.142
ρ, g/cm^3	6.488	6.325	6.627	6.365

The calculated densities provided in Table 8.1 demonstrate that the transition from the completely disordered structure to the completely ordered one produces small density changes of 2.5% and 4% for the cobalt and zinc perovskites, respectively. Formation of the $Ba_5Nb_4O_{15}$ and $Ba_8BNb_6O_{24}$ (B = Co or Zn) phases having theoretical densities close to the densities of the completely ordered niobium perovskites is expected to produce a similar influence on the density of materials as B-site cation ordering. The largest impact on the total density can be expected from the appearance of the

$Ba_6BNb_9O_{30}$ (B = Co or Zn) phase having 11.4% density variation from the main material.

Table 8.2 Calculated densities of secondary phases found in the near-stoichiometric compositions of perovskite type material.

Formula	$Ba_5Nb_4O_{15}$	$Ba_8CoNb_6O_{24}$	$Ba_6CoNb_9O_{30}$
Space group	P-3m1	P-3m1	P4bm
a, Å	5.788	5.789	12.589
b, Å	5.788	5.789	12.589
c, Å	11.788	18.893	4.009
ρ, g/cm^3	6.346	6.357	5.747

Formation of perovskite ceramics with deficiencies on the B-sublattice is accompanied by a disorder-order phase transition for the intermediate values of the B-site deficiencies that changes with the appearance of B-site deficient secondary phases, the concentration of which increases with further deviation from the nominal concentration of the B-cation (equation 7.3). The appearance of a structure having an ordered cation arrangement and B-site deficient secondary phases with a lower density in comparison to the density of the main material causes a decrease in the measured density demonstrated in Figure 8.1. Similar behavior is observed in the case of materials having an excess of the Ba-cation where according to equation (7.6), the $Ba_8BNb_6O_{24}$ phase is formed. Formation of the Ba-deficient phases in Ba-deficient and B-site rich materials (equations 7.4 and 7.5) with significantly lower theoretical densities should result in the reduction of

the total density. This contradicts the results of density measurements presented in Figures 8.1, 8.3, and 8.4, where an increase in the density of samples of the mentioned compositions was observed.

During the preparation process it was noticed that sintering of samples, that represent tablet of diameter d and height h, having Ba-site deficiencies and an excess of

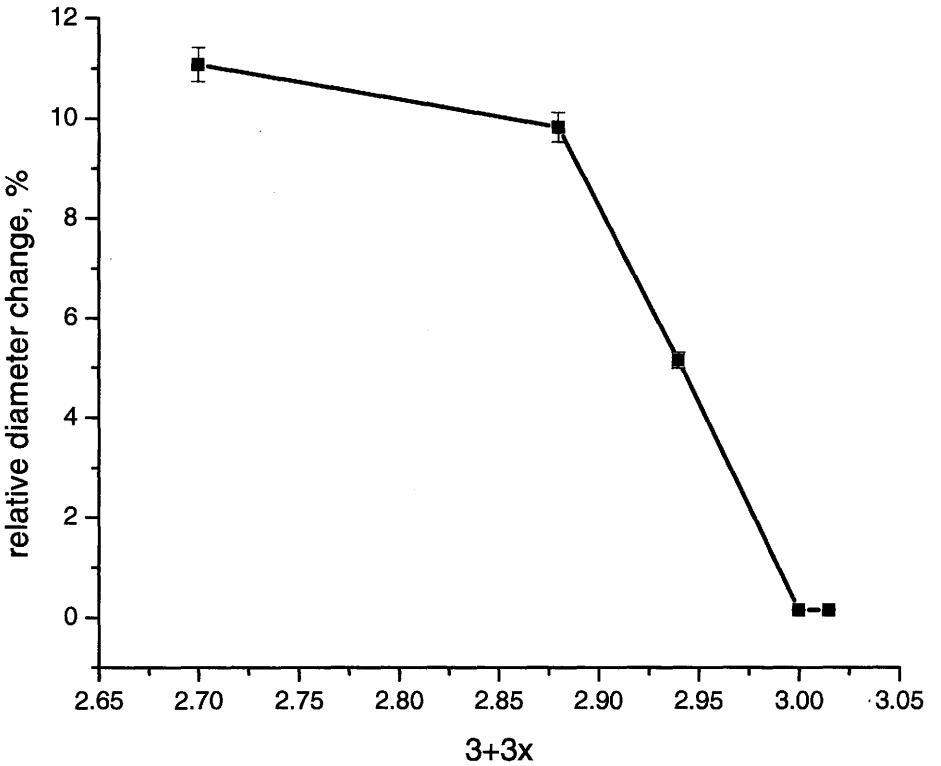

Figure 8.5 Relative changes in the diameter of samples with Ba-site nonstoichiometry after sintering with respect to the diameter of the samples before sintering.

the B-site cation always results in significant shrinkage of samples, while no noticeable variation in the dimensions of samples with deficiencies on the B-site were observed. Figure 8.5 demonstrates relative changes of the diameter of sintered samples with Ba-

nonstoichiometry with respect to the diameter of samples before sintering for intermediate sintering temperatures. Stoichiometric samples as well as samples with an excess of barium did not exhibit a significant variation in the size of samples at the same time as the relative change in the diameter of ceramic samples with 3+3x = 2.7 is on the order of 10%. Ceramic materials consisting of grains of different shapes and dimensions inevitably contain some amount of porous spaces influencing their densities. The observed increase in the total measured density accompanied by the formation of the low-density secondary phase can be explained by changes in the porosity of samples influenced by the secondary phase. Figure 8.6 shows changes in the porosity of samples defined as the volume of the toluene absorbed by the material to the total sample's volume. $Ba_{3+3x}B_{1+y}Nb_2O_9$ samples with 3+3x = 2.7 and 1+y= 1.03 sintered at 1300°C and 1400°C, where the $Ba_6BNb_9O_{30}$ phase was found, demonstrate a low porosity level, while those with a nominal composition, an excess of barium and B-site deficiencies have some amount of pores, the total volume of which decreases with increasing sintering temperature. An increase in the preparation temperature to 1500°C leads to zero porosity (within the accuracy of the measuring technique) of samples with stoichiometric composition and with B-site deficiencies, and a simultaneous increase in the porosity level of samples containing the $Ba_6BNb_9O_{30}$ phase. No liquid absorption was observed in samples prepared by applying lower (500-800kg/cm^2) formation pressures.

So, densification observed in Ba-site deficient and B-site rich materials is due to: a) formation of the low-density $Ba_6BNb_9O_{30}$ phase and b) elimination of pores present between grains. The mutual influence of those two processes results in the increase of the

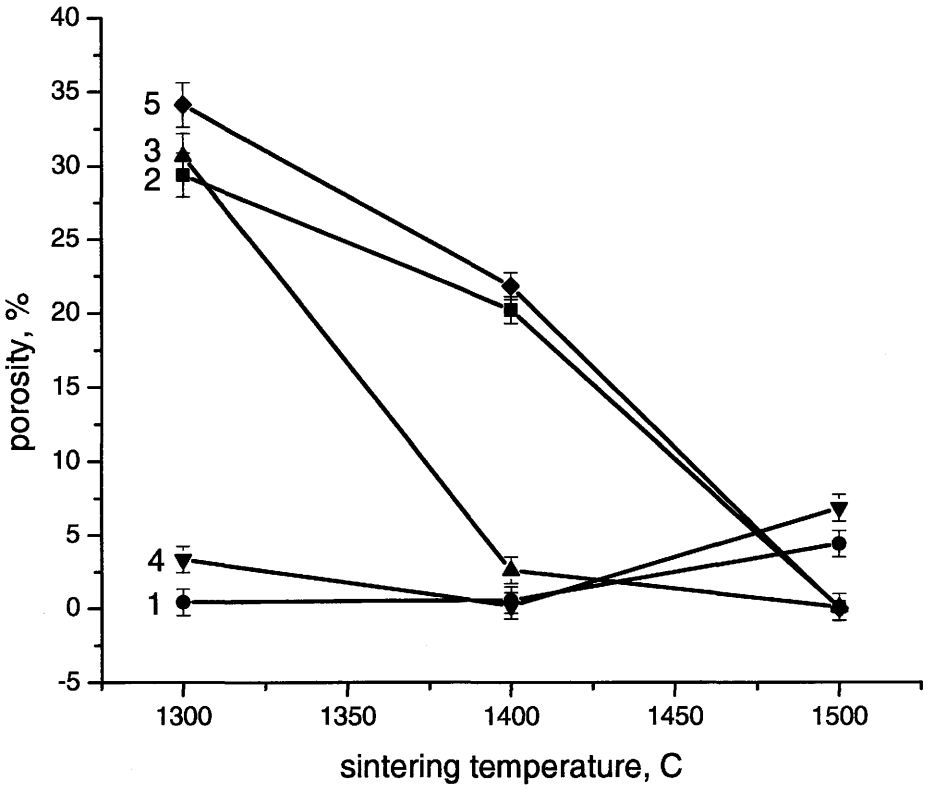

Figure 8.6 Variation in the porosity level caused by deviation from the stoichiometry on the cation sites. 1- $Ba_3B_{1.03}Nb_2O_9$, 2- $Ba_3BNb_2O_9$, 3- $Ba_3B_{0.93}Nb_2O_9$, 4- $Ba_{2.7}BNb_2O_9$, 5- $Ba_{3.015}BNb_2O_9$.

total density of the considered samples. The density drop observed in, for example, $Ba_{2.7}ZnNb_2O_9$ sintered at 1350°C and 1450°C (Figure 8.4) and $Ba_3Co_{1.03}Nb_2O_9$ sintered at 1500°C (Figure 8.2) materials is due to the increased porosity caused possibly by the presence of the Ba-deficient $Ba_6BNb_9O_{30}$ phase. In order to eliminate the role of the Ba-deficient phase, the microstructure of the studied materials should be considered, and is presented in the next section.

8.2 Microstructure of $Ba_{3+3x}B_{1+y}Nb_2O_9$ perovskites

The results of SEM measurements of the cracked surface of zinc and cobalt perovskite samples prepared by applying higher pressure and sintered at 1250°C and 1300°C, respectively, with nominal composition, and those containing cation deficiencies are presented in Figure 8.7. Samples sintered at low temperatures are characterized by high porosity levels and formation of agglomerations of grains with the diameter of grains ranging from 0.5μm to 1μm. Close observation of the barium deficient perovskites (Figure 8.7 d and f) revealed the formation of randomly distributed grains having sizes exceeding the average diameter of the grains: the grain size of the overgrown grains ranges from 1-2μm to 10-20μm. (Note that Figure 8.7 d was recorded at larger magnification. Thus, the volume of voids is exaggerated in comparison to the other images provided). The presence of grains having sizes almost one order of magnitude larger than the average grain size decreases the porosity of a material, thereby increasing its density.

Figure 8.8 shows the microstructure of $Ba_{3+3x}B_{1+y}Nb_2O_9$ perovskites sintered at 1425°C and 1500°C, respectively for Zn and Co cations on the B-sublattice. The stoichiometric composition of perovskite oxides sintered at high temperatures (Figure 8.8

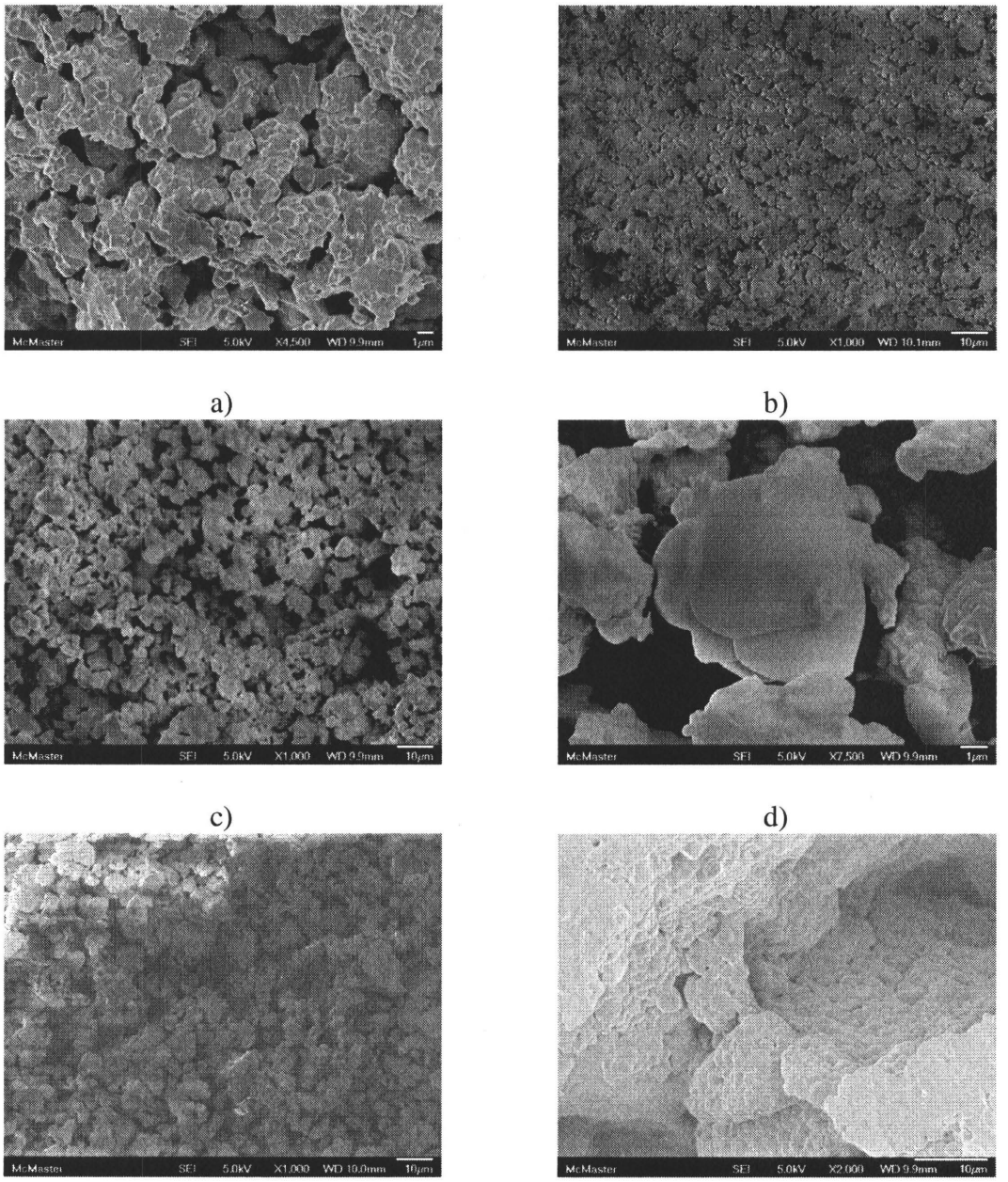

Figure 8.7 SEM images of cracked surfaces of $Ba_{3+3x}B_{1+y}Nb_2O_9$ perovskites prepared by applying higher pressures. a) $Ba_3ZnNb_2O_9$ 1250°C, b) $Ba_3Zn_{0.93}Nb_2O_9$ 1250°C, c) $Ba_{2.7}ZnNb_2O_9$ 1250°C, d) $Ba_{2.7}ZnNb_2O_9$ 1250°C, e) $Ba_3CoNb_2O_9$ 1300°C, f) $Ba_{2.7}CoNb_2O_9$ 1300°C.

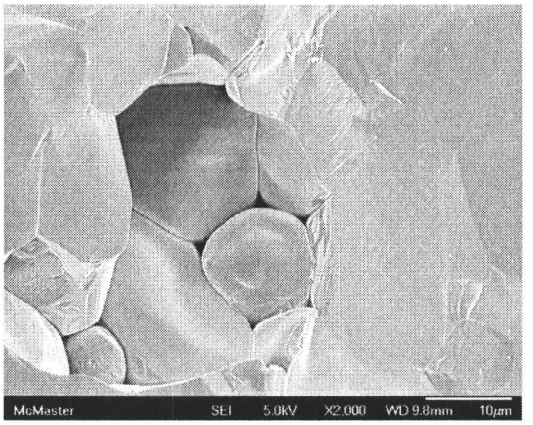

a)

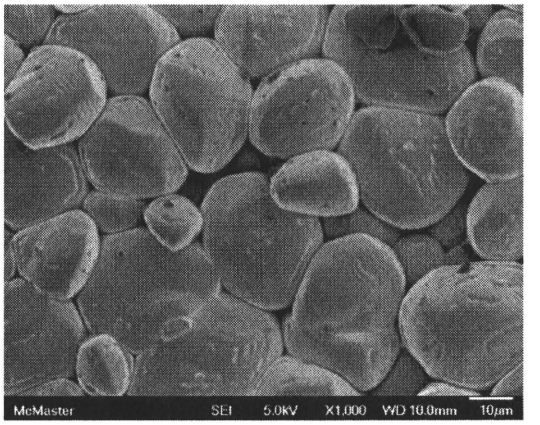

b)

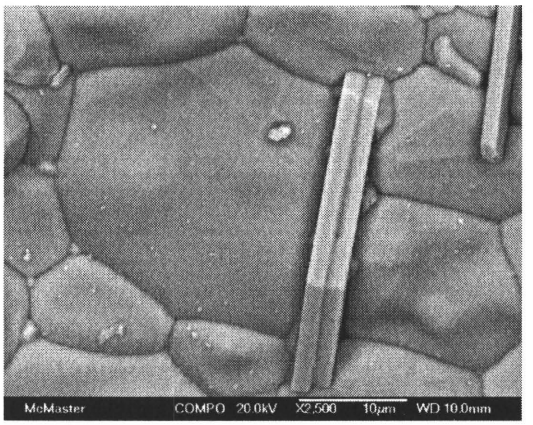

c)

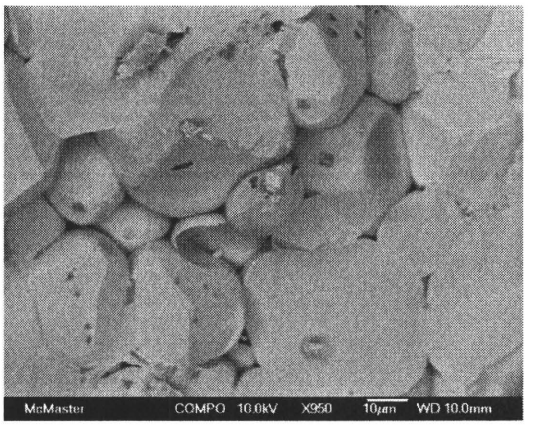

d)

Figure 8.8 SEM images of cracked surfaces of $Ba_{3+3x}B_{1+y}Nb_2O_9$ perovskites. a) $Ba_3ZnNb_2O_9$ 1425°C, b) $Ba_{2.7}ZnNb_2O_9$ 1425°C, c) $Ba_3Co_{0.85}Nb_2O_9$ 1500°C, d) $Ba_{2.7}CoNb_2O_9$ 1500°C.

a) is characterized by low porosity levels. The introduction of the B-site cation vacancies (Figure 8.8 c) does not change the porosity level. Samples having barium deficiencies (figure 8.8 b and d) demonstrate void formation inside of grains and the increase of spaces between grains. It should be noted that cobalt-containing perovskites with barium

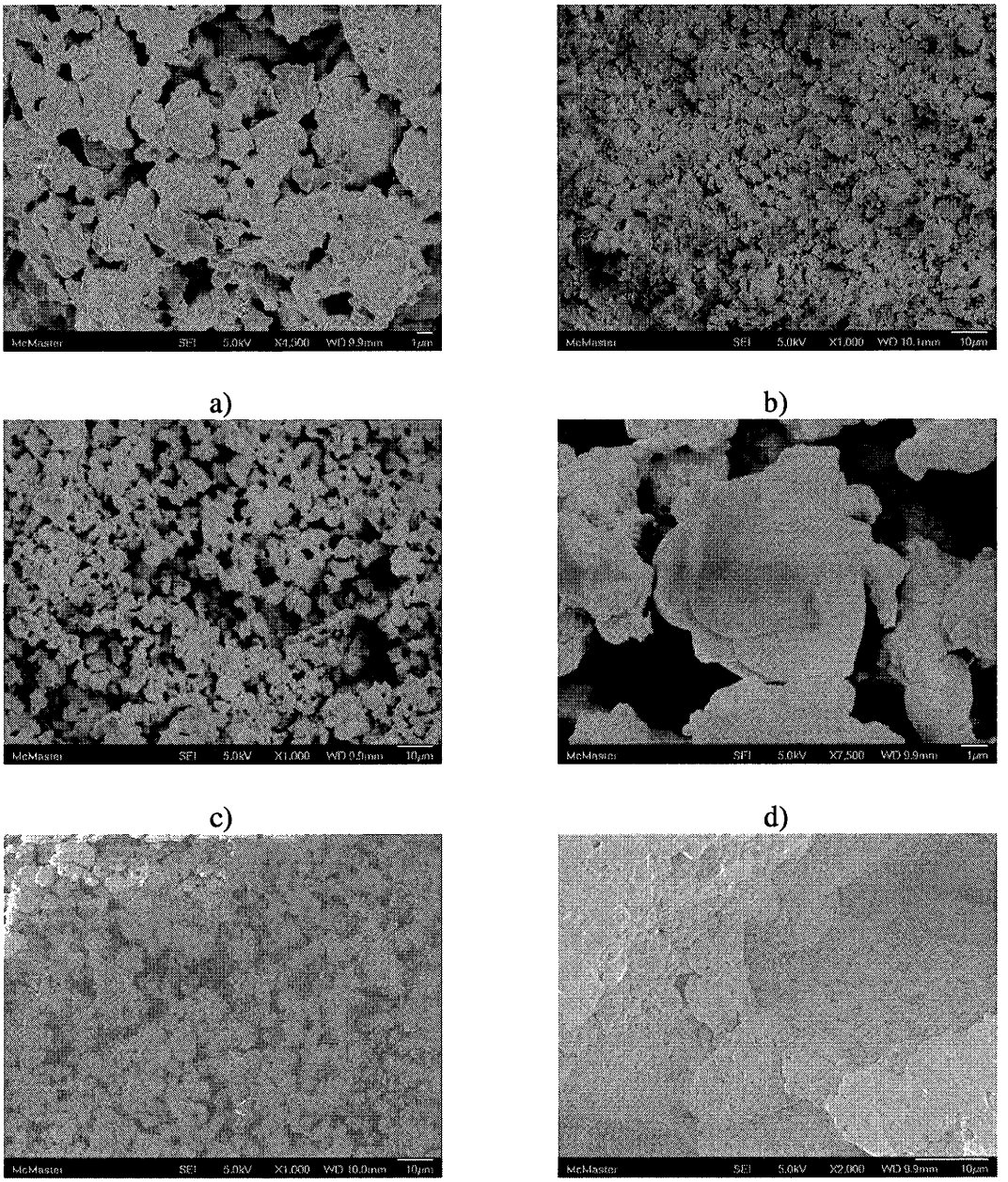

Figure 8.7 SEM images of cracked surfaces of $Ba_{3+3x}B_{1+y}Nb_2O_9$ perovskites prepared by applying higher pressures. a) $Ba_3ZnNb_2O_9$ 1250°C, b) $Ba_3Zn_{0.93}Nb_2O_9$ 1250°C, c) $Ba_{2.7}ZnNb_2O_9$ 1250°C, d) $Ba_{2.7}ZnNb_2O_9$ 1250°C, e) $Ba_3CoNb_2O_9$ 1300°C, f) $Ba_{2.7}CoNb_2O_9$ 1300°C.

deficiencies showed a significant amount of grains having "egg-shell" structure; the inner part of the grain is filled with air and covered with a layer of the perovskite material.

The presence of deficiencies on the barium site, in addition to the higher porosity level, modifies the average grain size; the average grain size in the barium deficient samples, where a significant concentration of the $Ba_6BNb_9O_{30}$ phase was observed, increases. Figure 8.8 d shows the presence of a secondary phase formed between grains. The result of the EDS analysis (Table 8.3) demonstrates that the chemical composition of the material found between grains is close to that of the $Ba_6CoNb_9O_{30}$ phase. Formation of the barium deficient phase found between grains could reduce the surface energy, increasing the grain growth rate. The presence of the $Ba_6BNb_9O_{30}$ structure in the low temperature sintered oxides could be the reason of the abnormal grain growth found in samples with barium deficiencies.

Table 8.3. Atomic fraction (%) of elements composing phase found between grains in barium deficient perovskites.

Element	Atomic fraction, %
Ba	12.6 ± 0.2
Co	2.1 ± 0.2
Nb	21.1 ± 0.3
O	64.2 ± 1.9

TEM images of cobalt perovskites prepared by applying lower pressures are shown in Figure 8.9. The average size of grains composing the material for samples prepared by applying lower pressures is smaller in comparison to their higher-pressure counterparts. Cobalt deficient perovskites (Figure 8.9 a) have a homogeneous distribution

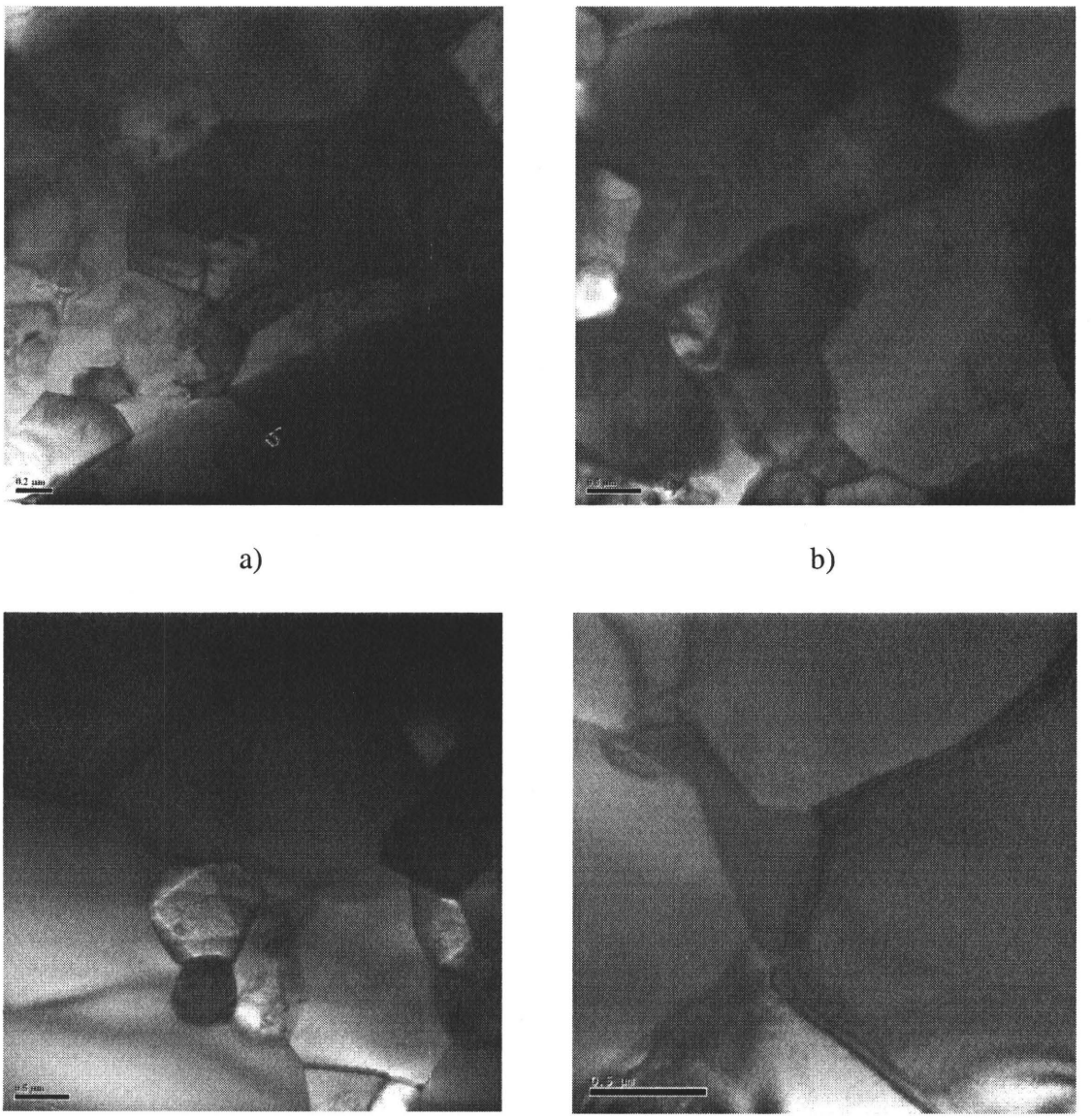

a) b)

c) d)

Figure 8.9 TEM images of $Ba_3B_{1+y}Nb_2O_9$ perovskites. a) $Ba_3Co_{0.93}Nb_2O_9$, b) $Ba_3CoNb_2O_9$, c) $Ba_3Co_{1.03}Nb_2O_9$, d) $Ba_3Co_{1.03}Nb_2O_9$.

of grain size, with the size of about 0.5μm. By increasing the cobalt content, the distribution of the grain sizes changes; samples having an excess of cobalt show the presence of grains exceeding 1μm in size that neighbor with smaller-size grains. The $Ba_3Co_{1.03}Nb_2O_9$ perovskite (Figure 8.9 d) also exhibits formation of a secondary phase between grains. The small amount of the phase made it impossible to measure its chemical composition. However, according to equation (7.2) that describes the formation of a secondary phase in nonstoichiometric perovskites having an excess of the B-site cation, and the results of the X-ray diffraction analysis on the high-pressure cobalt perovskites, we believe that this phase is $Ba_6CoNb_9O_{30}$.

8.3 Discussion

Numerous studies on the microwave properties of perovskite type oxides indicated that superior microwave properties could be realized only in highly dense materials having low porosity levels [11, 116, 147]. The level of porosity depends on the number and size of the grains composing the structure. While nucleation, that is, formation of new grains, is a random process in the sense that new embryos appear randomly on different inhomogeneities present in the system (like impurity atoms), and cannot be efficiently controlled, the grain growth rate is influenced by several factors: a) initial energy stored in the strained matrix during the preparation process of samples, b) energy supplied during the sintering process, c) lowering in the surface energy caused by the presence of the barium deficient phase. Following nucleation, grain growth involves atomic diffusion or jumping from one neighboring site of crystal to the other.

The efficiency of the atomic diffusion is influenced by the external energy supplied to the system, that is, the sintering temperature, and the distance the atoms have to travel. By applying higher pressures during the process of sample formation, one can achieve a smaller space between precursor oxides, decreasing the distance atoms have to travel. This causes a higher grain growth rate observed in perovskites prepared by using higher pressures for compacting the perovskite precursor powder.

Perovskite oxides sintered at lower temperatures are characterized by the formation of agglomerations of grains. Within each group, grain sizes vary from 0.5μm to 1μm. The presence of the barium deficient phase found between grains reduces the surface energy of grains, promoting their growth (Figure 8.7 d and f). For materials sintered at lower temperatures, the appearance of grains with extra large sizes leads to reduced porosity, and as a result, increases the total density of the sample in spite of the presence of the low density secondary phase. The influence of the $Ba_6BNb_9O_{30}$ phase was found in samples containing an excess of the B-site cations, and those with large deficiencies on the barium position. As demonstrated by Prokopalo [144,145], the concentration of defects that is responsible for the cation diffusion and the B-site ordering process in ceramic materials increases from the center of the grain towards its surface. The increase in the size of grains reduces the surface area, thereby decreasing the number of available defect sites. The large grain growth rate caused by the presence of the barium deficient phase can be responsible for the decrease in the B-site cation ordering found in the previous chapter in perovskites containing large values of barium deficiencies and an excess of B-site cations.

By increasing the sintering temperature and leaving the rest of the factors unchanged, one promotes faster grain growth. During primary recrystallization, the number of grains does not change and grain growth occurs at the expense of voids found between agglomerations of grains. This stage is characterized by a reduced porosity found in perovskites sintered at intermediate temperatures. The fact that no significant difference in the grain size of samples containing the $Ba_6BNb_9O_{30}$ phase and sintered at high temperatures was found, indicates that the growth of the "abnormally grown" grains discontinues and densification of ceramics containing the barium deficient phase occurs at expense of normally grown grains.

A further increase in the sintering temperature leads to the so-called secondary recrystallization, when grains impinge on each other and larger grains absorb grains having a smaller than average size. The absorption of grains by each other represents the grain boundary diffusion process and is affected by inclusions present in the system: during surface migration, an inclusion encountered by the grain could be displaced, decreasing the energy available for grain growth. Pores that exist between grains represent inclusions. During the fast growing process, the surface of some grains cannot effectively push away pores, forcing them inside of the bulk and creating voids. Lowering in the surface tension due to the presence of the $Ba_6BNb_9O_{30}$ phase accompanied by the high sintering temperature and large initial strain present in the system creates conditions for fast grain growth and subsequent appearance of voids and "egg-shell" formations in the structure observed in Figures 8.8 b and d. An increase in porosity of perovskite materials containing a large amount of the barium deficient phase

and sintered at high temperatures reduces the density of ceramic. Contrary to the highly strained samples, low strained materials do not exhibit the formation of voids due to the slower grain growth rate (Figure 8.9 c).

Changes in the grain size with the sintering temperature influence the size and distribution of the barium deficient phase. Assuming that there is no loss in the material during the sintering process (this is the case of the $Ba_3Co_{1+y}Nb_2O_9$ perovskite, where no evaporation of material was observed) and since no other phase was found with an increase in sintering temperature, the amount of the $Ba_6BNb_9O_{30}$ material should stay the same. The small amount and dimensions of the secondary phase limit the sensitivity of the X-ray diffraction technique used for crystallographic analysis: reducing the size of the particle below some critical value broadens diffraction peaks and lowers the signal to noise ratio. By increasing the sintering temperature and promoting grain growth, one decreases the space between grains, modifying the size of the barium deficient phase. This could be the reason that $Ba_6CoNb_9O_{30}$ could not be detected in low-strained $Ba_3Co_{1.03}Nb_2O_9$ perovskite that has smaller (in comparison to the high-strained oxides) grains, limiting the size of the secondary phase.

Formation of the B-site deficient secondary phases found in the studied perovskites did not produce noticeable changes in the porosity of ceramics, and only influenced the material density because of the reduced density of secondary phases in comparison to the main disordered material. Ceramics sintered at high temperatures demonstrate the formation of void-free grains.

8.4 Conclusions

Deviation from stoichiometry results in the formation of cation deficient phases having theoretical densities smaller than the density of the main disordered structure. Change in the density of the considered nonstoichiometric oxides is due to the variation in the amount of porosity and concentrations of secondary phases. The appearance of B-cation deficient secondary phases in perovskites with B-site deficiencies and an excess of cations on the Ba site did not produce changes in the amount of porosity of ceramics, reducing the overall system density. Variation in the density of materials containing the $Ba_6BNb_9O_{30}$ phase is the result of two processes: the increase in the amount of the secondary phase with a significantly smaller theoretical density and changes in the porosity of the material influenced by the $Ba_6BNb_9O_{30}$ phase. Formation of the barium deficient structure increases the density of the material at low and intermediate temperatures due to the lower porosity level, and leads to larger porosity at high temperatures.

Chapter 9

Optical Characterization of Nonstoichiometric $Ba(B_{1/3}Nb_{2/3})O_3$ (B = Co or Zn)

Previous chapters demonstrated that $Ba_{3+3x}B_{1+y}Nb_2O_9$ (B = Co or Zn) materials having perovskite structure are stable in a narrow range of nonstoichiometries. Small cation deficiencies on either Ba- or B-sites result in enhanced cation diffusion producing 1:2 ordering. Further deviation of cation concentrations from the nominal values leads to structure destabilization and precipitation of secondary phases. In the case of cation deficiencies on barium sites and cation excesses on B-sites, the formation of barium deficient $Ba_6BNb_9O_{30}$ phases influencing densification process through variation in the porosity level of ceramics has been observed. Appearance of the B-cation deficient phases did not produce any noticeable changes in the porosity of ceramics. The value of the dielectric losses at microwave frequencies is an integral value that depends on the presence of secondary phases, porosity level and the degree of cation ordering. Correlation between the peak shape of Raman modes and the quality factor at microwave frequencies has been demonstrated by several authors [170,172]. Here we present results of Raman measurements of the studied perovskite oxides and compare them with the microwave quality factor obtained by Belous *et al* [200].

9.1 Raman spectroscopy

Group theoretical analysis predicts that the phase transition from the complete cation disorder on the B-site to the full 1:2 cation order produces nine Raman active modes while no appearance of Raman modes is expected for the disordered structure. An important feature of the group theory prediction for the Raman spectrum of $A(B'_{1/3}B''_{2/3})O_3$ perovskites with long range 1:2 order making it distinct from the 1:1 cation order is the dependence of Raman modes on the mass of the B″ cation [167]. $Ba(Mg_{1/3}Nb_{2/3})O_3$ and $Ba(Mg_{1/3}Ta_{2/3})O_3$ perovskites having two cations on the B-site with large mass difference exhibit a high tendency for cation ordering. Figure 9.1 shows X-ray diffraction patterns of BMN and BMT materials. Both ceramics are characterized by the appearance of intensive diffraction peaks originating from the 1:2 order. Measured Raman spectra of BMN and BMT perovskites are presented in Figure 9.2. Recent first principles calculations [124] of the Raman spectra of the 1:2 ordered BZN and BMN perovskites demonstrated that all observed modes are due to the formation of the 1:2 ordered phase rather than a mixture of 1:2 and 1:1 ordered structures supported by a number of publications [150,167,172]. Close examination of the measured Raman spectra (Figure 9.2) indicates that all modes (except for the high frequency mode) in perovskites containing heavier Ta^{5+} cation oxides are shifted toward lower energies in comparison to the Nb- counterpart. The dependence of peaks' position on the mass of the heavier Ta^{5+} cation confirms the validity of the origin of the observed modes. According to the work by Dai *et al* [124] the mode assignment is as follows. The low frequency mode at

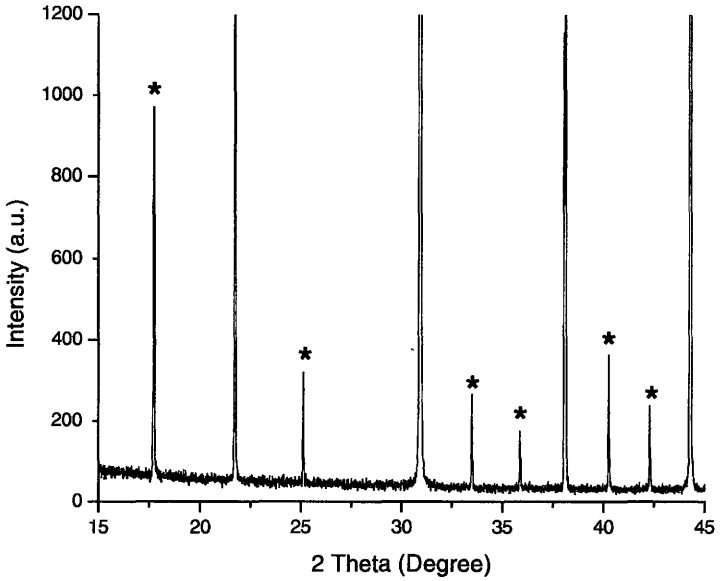

a)

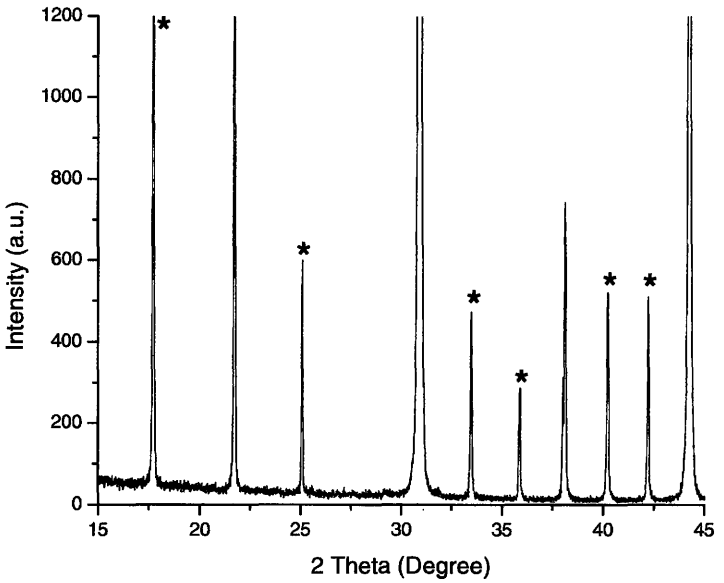

b)

Figure 9.1 XRD patterns of a) $Ba(Mg_{1/3}Nb_{2/3})O_3$ and b) $Ba(Mg_{1/3}Ta_{2/3})O_3$ perovskites. *- 1:2 ordered structure.

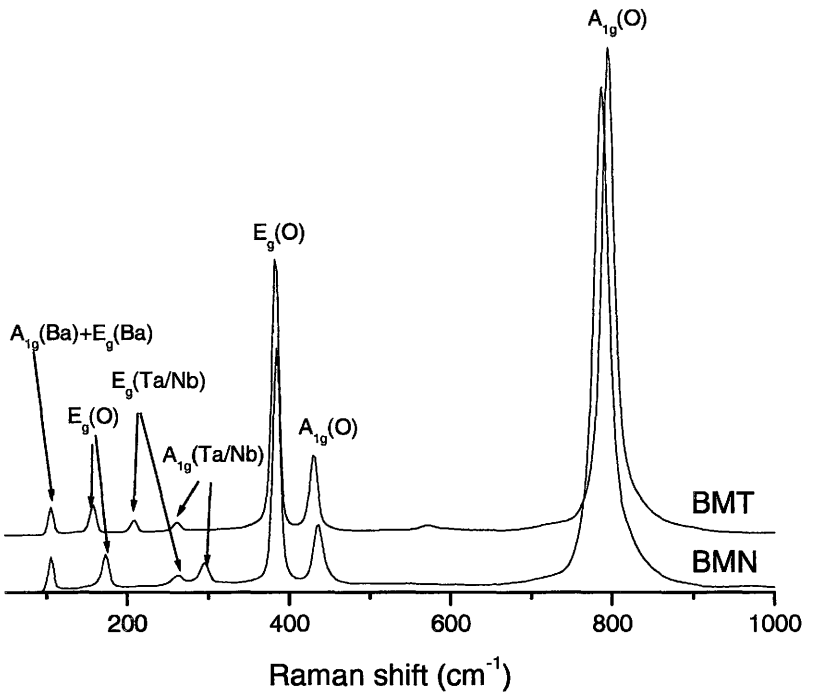

Figure 9.2 Raman spectra of stoichiometric $Ba(Mg_{1/3}Nb_{2/3})O_3$ and $Ba(Mg_{1/3}Ta_{2/3})O_3$ perovskites.

$105cm^{-1}$ is assigned to the $A_{1g}+E_g$ Ba vibrations. The mode at 157 and $174cm^{-1}$, respectively for BMT and BMN samples corresponds to the internal oxygen vibration E_g. Low intensity modes at $209cm^{-1}$ and $262cm^{-1}$ in BMT perovskites that shift to higher energy values of $262cm^{-1}$ and $295cm^{-1}$ with substitution of the heavier Ta atom for Nb, correspond to the E_g and A_{1g} vibrations of Ta/Nb. $383cm^{-1}$ and $430cm^{-1}$ modes are assigned to E_g and A_{1g} internal oxygen vibrations. The most intense A_{1g} mode around $800cm^{-1}$ is due to the collective oxygen-breathing type motions. Raman spectra of $Ba_3B_{1+y}Nb_2O_9$ (B = Co or Zn) prepared by applying low pressure are presented in Figures

9.3 and 9.4. In comparison to the BMN and BMT perovskites where seven distinct sharp modes were observed, Raman spectra of cobalt and zinc containing perovskites are diffuse. Generally, cobalt and zinc containing perovskites exhibit a lower tendency for cation ordering than their magnesium analogues because of the small mass difference between cations on the B-sublattice. The appearance of diffuse Raman active modes is a result of the small range of 1:2 cation ordering and in accordance with the previously made assumption about the origin of Raman modes.

According to the results presented in Figure 9.4, deviation from stoichiometry in $Ba_3Zn_{1+y}Nb_2O_9$ oxides produced Raman spectra that are similar in shape and position

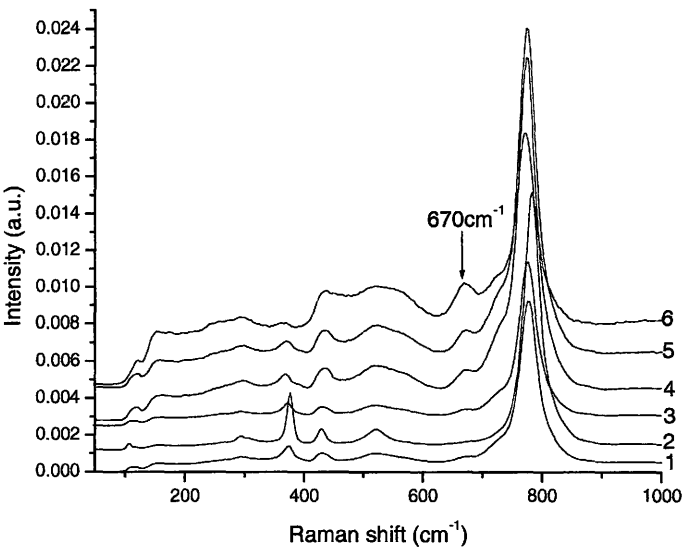

Figure 9.3 Raman spectra of $Ba_3Co_{1+y}Nb_2O_9$ prepared by applying 500-800kg/cm^2 pressures during the perovskite stage and sintered at 1470°C. 1) 1+y= 0.85, 2) 1+y= 0.93, 3) 1+y = 0.96, 4) 1+y = 1, 5) 1+y = 1.01, 6) 1+y = 1.03.

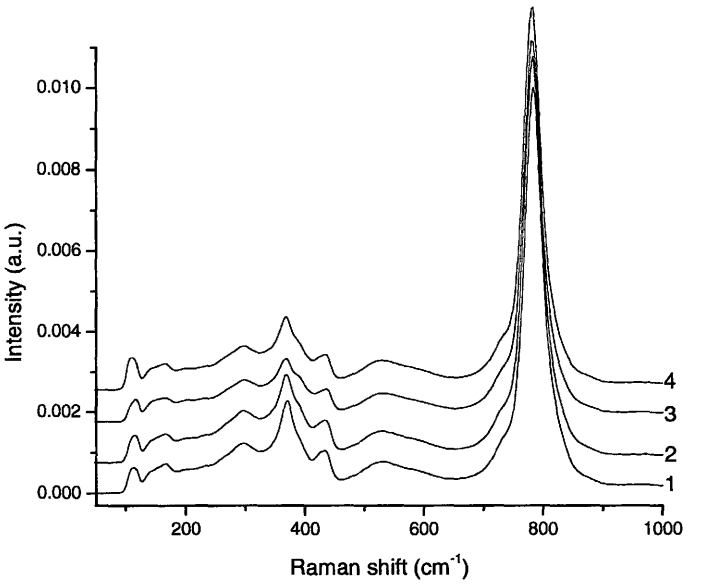

Figure 9.4 Raman spectra of $Ba_3Zn_{1+y}Nb_2O_9$ prepared by applying 500-800kg/cm^2 pressures during the perovskite stage and sintered at 1445°C. 1) 1+y= 0.93, 2) 1+y= 0.96, 3) 1+y = 1, 4) 1+y = 1.005.

of modes while in the case of the cobalt system a variation in cobalt content significantly modifies the Raman spectra. Samples containing an excess of cobalt cations have diffuse peaks. By decreasing the cobalt content Raman modes at first become sharp (1+y = 0.93) and then have tendency to disperse (1+y = 0.85). This mode behavior is in agreement with the results of X-ray diffraction. In Chapter 7 it was found that zinc nonstoichiometry produced zinc deficient secondary phases preventing the 1:2 ordering process whereas variation in cobalt content at first promoted ordering behavior for intermediate nonstoichiometries (1+y = 0.93) and then degraded the ordering process due to the formation of $Ba_6CoNb_9O_{30}$ phase. Thus, a change in the shape of the Raman active

modes with nonstoichiometries on the B-sites in $Ba_3Co_{1+y}Nb_2O_9$ perovskites is due to the formation of the 1:2 ordered structure.

Raman spectra of $Ba_{3+3x}BNb_2O_9$ (B = Co or Zn) are presented in Figures 9.5 and 9.6. Samples containing large values of barium deficiencies (Figure 9.5, graph 1) are characterized by diffuse Raman modes that become sharp for intermediate values of barium deficiencies (3+3x = 2.94, Figure 9.5, graph 2 and Figure 9.6, graph 1). Further increase in the amount of barium leads to a smearing out of the Raman spectra in both sets of samples. X-ray diffraction demonstrated that small values of nonstoichiometry on the barium site promoted 1:2 cation ordering, but additional decreases in the amount of

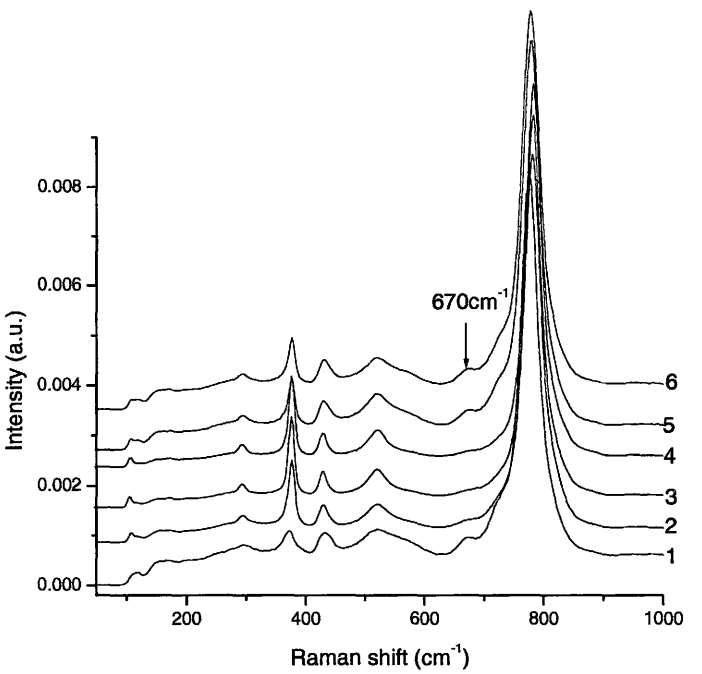

Figure 9.5 Raman spectra of $Ba_{3+3x}CoNb_2O_9$ prepared by applying 500-800kg/cm^2 pressures during the perovskite stage and sintered at 1470°C. 1) 3+3x=2.7, 2) 3+3x=2.94, 3) 3+3x = 2.97, 4) 3+3x = 2.98, 5) 3+3x = 3, 6) 3+3x = 3.015.

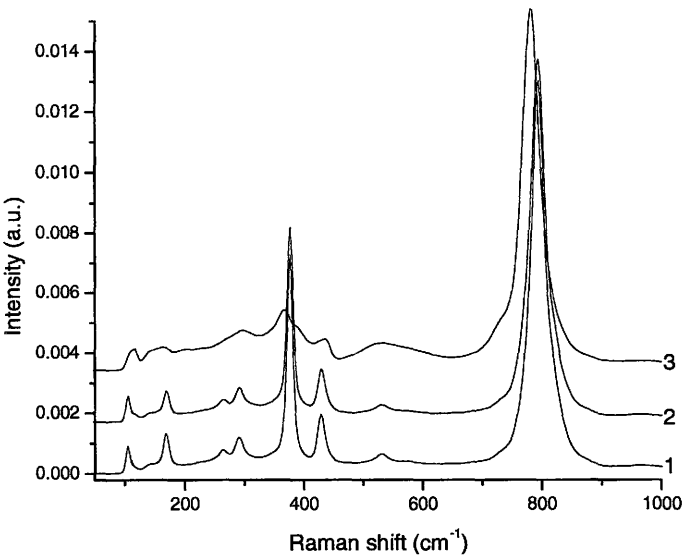

Figure 9.6 Raman spectra of $Ba_{3+3x}ZnNb_2O_9$ prepared by applying 500-800kg/cm^2 pressures during the perovskite stage and sintered at 1445°C. 1)3+3x = 2.94, 2)3+3x = 2.985, 3)3+3x = 3.

barium below 3+3x = 2.94 resulted in the precipitation of barium deficient $Ba_6BNb_9O_{30}$ phase degrading ordering process. As in the case of B-site nonstoichiometry, the shape of the Raman spectra of perovskites with Ba-nonstoichiometries is governed by formation of the ordered structure.

The characteristic feature of the most complex perovskites is the appearance of a mode around 800cm^{-1} that was attributed to the collective motion of oxygen anions, resembling a breathing-type vibration [167]. This mode has been observed in both 1:1 and 1:2 ordered perovskites [166,201,202]. Lee *et al* [170] and Chia *et al* [172] correlated changes in the shape of $A_{1g}(O)$ mode with the quality factor at microwave frequencies: materials demonstrating a large quality factor have strong oxygen breathing-type modes

that is, with increasing Qxf value the full width at half maximum (FWHM) of the $A_{1g}(O)$ mode decreases. Figure 9.7 shows the FWHM of the $A_{1g}(O)$ mode of the studied perovskites. The dependence of the FWHM on the cation nonstoichiometries on both B-

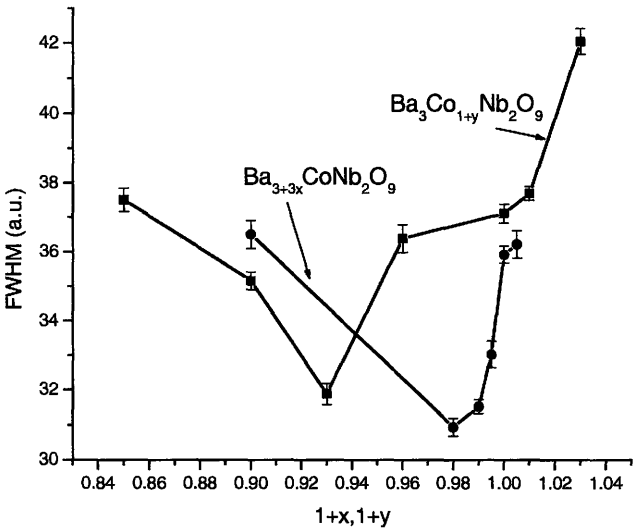

a)

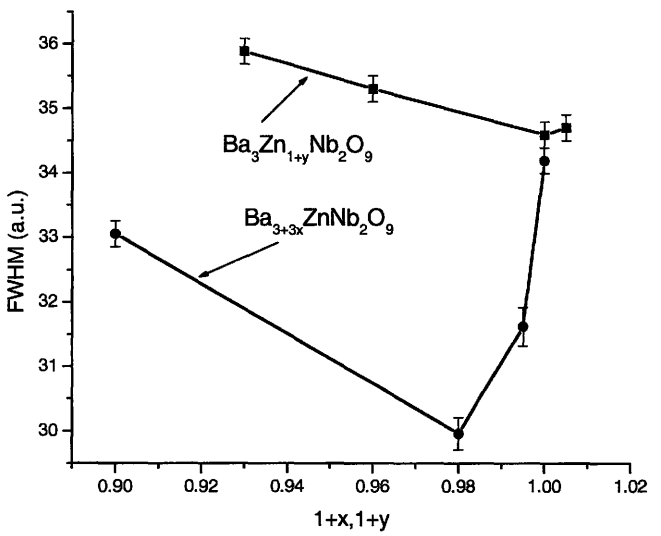

b)

Figure 9.7 FWHM of $A_{1g}(O)$ mode in perovskites prepared by applying 500-800kg/cm^2 pressures during the perovskite stage. a) $Ba_{3+3x}Co_{1+y}Nb_2O_9$, b) $Ba_{3+3x}Zn_{1+y}Nb_2O_9$.

and Ba- sites is analogous to the variation in the Qxf value reported by Belous *et al* [200]. Thus, the FWHM of the mode originating from the collective motion of oxygen anions can be used to trace changes in the dielectric losses influenced by crystal symmetry and microstructure of materials. In addition to having a different line shape, deviation from stoichiometry results in different positions of the $A_{1g}(O)$ mode (Figures 9.8 and 9.9): perovskites having lower FWHM (high Qxf value) exhibit a shift of the breathing-type modes toward higher energies. In the case of $Ba_3Zn_{1+y}Nb_2O_9$ where no variation in the FWHM as well as the Qxf value was found, the position of the $A_{1g}(O)$ peak remains unchanged with zinc content. The only discrepancy was found in the $Ba_{3+3x}CoNb_2O_9$ system, where the higher energy $A_{1g}(O)$ mode was observed for 3+3x = 2.98 (in contrast, the FWHM reaches a minimum value for 3+3x = 2.94). This inconsistency can be related to inhomogeneities in the sample's microstructure within the sample. Comparison of Raman spectra from perovskite materials prepared by applying higher formation pressure (1200kg/cm^2) prior to sintering to respective samples obtained by using lower pressure (500-800kg/cm^2) demonstrates shift of $A_{1g}(O)$ vibration toward higher energies (Figure 9.10).

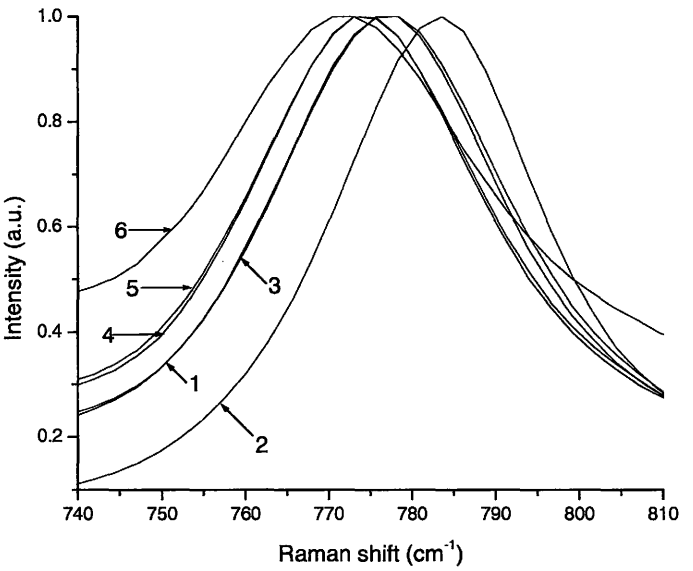

a)

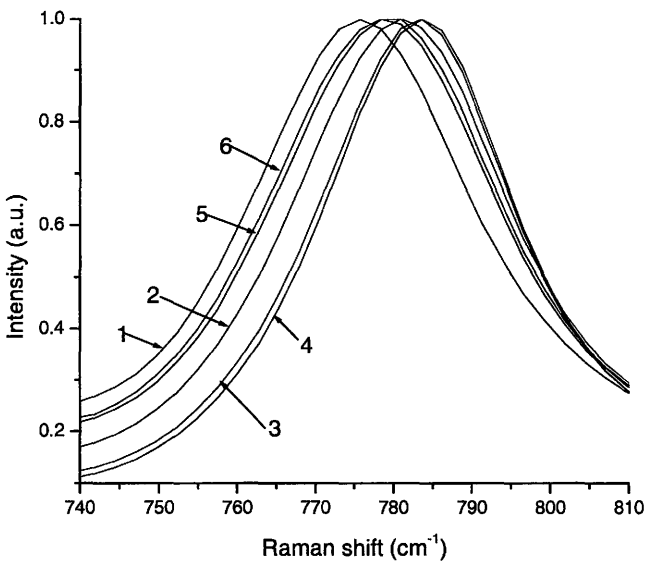

b)

Figure 9.8 Dependence of position of $A_{1g}(O)$ mode on stoichiometry in a) $Ba_3Co_{1+y}Nb_2O_9$: 1) 1+y = 0.85, 2) 1+y = 0.93, 3) 1+y = 0.96, 4) 1+y = 1, 5) 1+y = 1.01, 6) 1+y = 1.03; b) $Ba_{3+3x}CoNb_2O_9$: 1) 3+3x = 2.7, 2) 3+3x = 2.94, 3) 3+3x = 2.97, 4) 3+3x= 2.98, 5) 3+3x=3, 6) 3+3x=3.015 perovskites prepared by applying 500-800kg/cm^2 pressures during the perovskite stage and sintered at 1470°C.

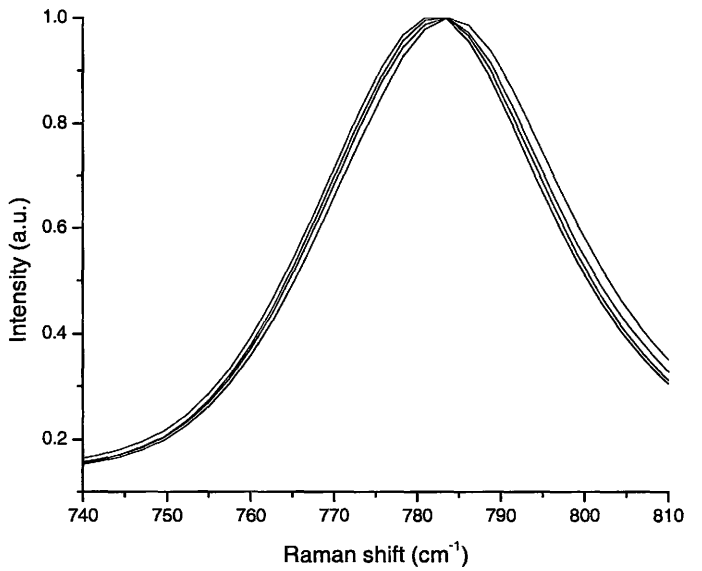

a)

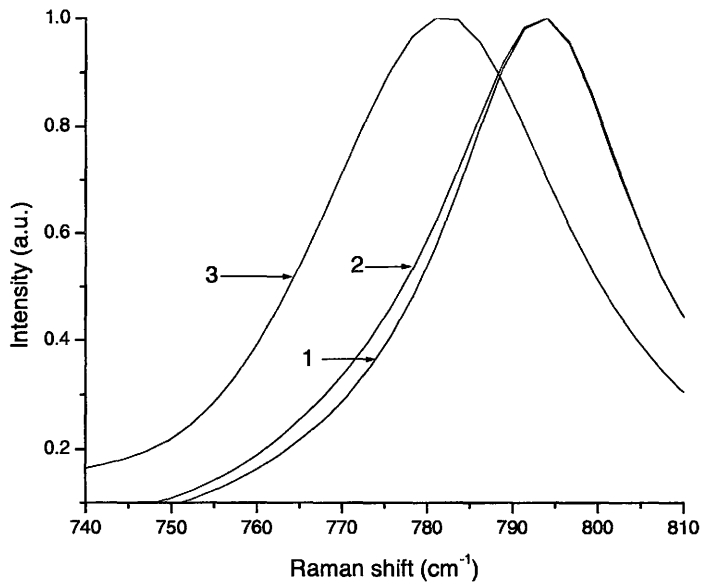

b)

Figure 9.9 Dependence of position of $A_{1g}(O)$ mode on stoichiometry in a) $Ba_3Zn_{1+y}Nb_2O_9$; b) $Ba_{3+3x}ZnNb_2O_9$: 1) 3+3x = 2.94, 2) 3+3x = 2.985, 3) 3+3x = 3 perovskites prepared by applying 500-800kg/cm^2 pressures during the perovskite stage and sintered at 1445°C.

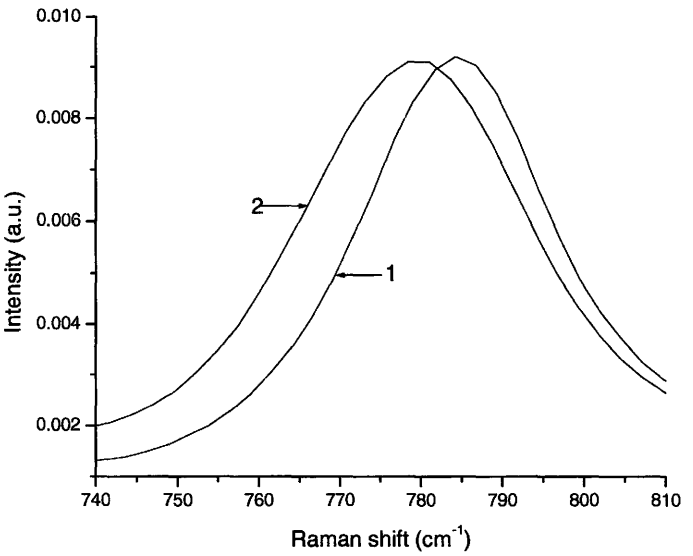

Figure 9.10 Change in position of $A_{1g}(O)$ mode for samples prepared by applying different formation pressure on the example of stoichiometric $Ba_3BNb_2O_9$ (B = Co or Zn) composition. 1- 1200kg/cm^2, 2- 500-800kg/cm^2.

9.2 Raman spectroscopy: coexistence of 1:2 and 1:1 order

It has been demonstrated by several research groups [27,53,76,79] that formation of the 1:2 ordered structure could be accompanied by the appearance of 1:1 order in a narrow range of doping concentrations or under certain preparation conditions. As has been discussed in section 2.4.3, formation of the 1:1 ordered structure in perovskite oxides containing 1:2 ratio of cations on B-site can be explained based on the "random-site" or "space-charge" models. The latter has been successfully applied to explain the appearance of 1:1 order in $Pb(B'_{1/3}B''_{2/3})O_3$ perovskites [27,69].

One of the most intensive oxygen breathing-type $A_{1g}(O)$ modes has been a characteristic feature of perovskites containing 1:2 and 1:1 ordered cation arrangements [160,166,167,172]. Examination of presently measured Raman spectra (Figures 9.3 and 9.5) revealed the formation of an "extra" mode close to the $A_{1g}(O)$ vibration of a 1:2 ordered structure ($670cm^{-1}$ *vs* $780cm^{-1}$). The appearance of the additional mode was also observed in BMN and BMT perovskites (Figure 9.11) annealed in H_2. We attribute the appearance of the $670cm^{-1}$ mode to the $A_{1g}(O)$ vibration originating from the formation of the 1:1 cation order in the $Ba(B'_{1/3}B''_{2/3})O_3$ structure. Annealing in oxygen deficient environments introduces oxygen deficiencies that facilitate the 1:1 cation ordering

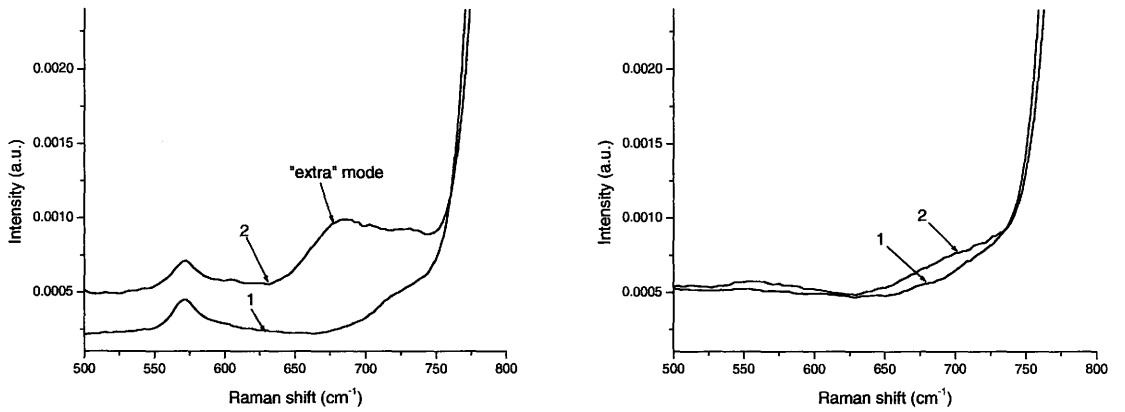

a) b)

Figure 9.11 Appearance of the 670cm^{-1} mode in hydrogen-annealed a) BMT and b) BMN samples. 1- as sintered, 2- after annealing in H_2.

processes in materials containing 1:2 ratio of cations on the B-site due to the internal charge compensation. The $Ba_3Co_{1+y}Nb_2O_9$ group of samples with nonstoichiometry on the cobalt position (Figure 9.3) contains the most intense 670cm^{-1} peak. Selected area electron diffraction (SAED) has been used to check for the presence of a 1:1 cation order. Samples with cobalt concentrations 1+y = 0.85, 0.93 and 1.03 were examined and the SAED results are shown in Figure 9.12. As revealed by electron diffraction, $Ba_3Co_{0.85}Nb_2O_9$ and $Ba_3Co_{1.03}Nb_2O_9$ are characterized by the appearance of {h±1/2,k±1/2,l±1/2} lattice reflections. In the absence of tilting of BO_6 oxygen octahedra (which is the case for perovskites with Ba^{2+} on the A-site having tolerance factor t > 1) {h±1/2,k±1/2,l±1/2} diffraction spots signify formation of 1:1 cation order. The $Ba_3Co_{0.93}Nb_2O_9$ sample shows {h±1/3,k±1/3,l±1/3} reflections attributed to the 1:2 order.

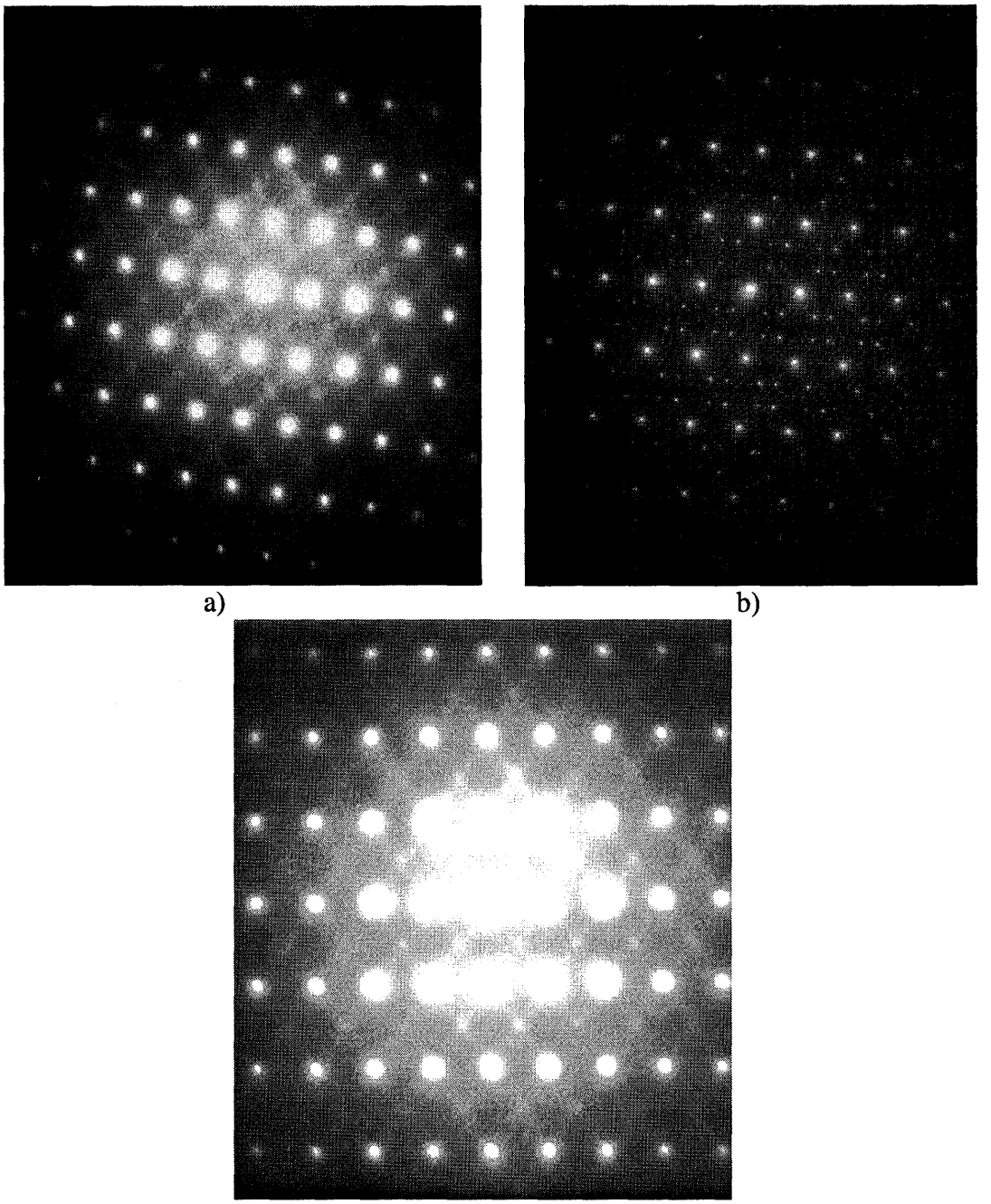

Figure 9.12 SAED of $Ba_3Co_{1+y}Nb_2O_9$ along [110] direction showing {h±1/2,k±1/2,l±1/2} and {h±1/3,k±1/3,l±1/3} lattice reflections. a)1+y = 0.85, b)1+y = 0.93, c)1+y = 1.03.

A 670cm^{-1} Raman peak was found in zinc perovskites sintered at low temperatures and cobalt containing perovskites. It has been demonstrated that the sintering of $Ba_{3+3x}Zn_{1+y}Nb_2O_9$ ceramic materials at high temperatures always results in ZnO evaporation further increasing the Nb/Zn ratio. This explains the formation of the 1:1 order in zinc perovskites only at lower temperatures where zinc oxide loss is minimal. The intensity of the $A_{1g}(O)$ mode from 1:1 ordered structure changes with stoichiometry and correlates with the amount of a 1:2 ordered structure: increase in the concentration of one type of order results in a decrease in the concentration of the second one and *vice versa*. Thus, the largest concentrations of 1:1 ordered structures were observed in samples containing excess of Ba^{2+} and B^{2+} as well as large deficiencies of both types of cations. Intermediate values of nonstoichiometries where large concentrations of 1:2 ordered structures were found are characterized by the disappearance of Raman peaks around 670cm^{-1} and hence the 1:1 ordered structure.

We described formation of the 1:1 ordered structure using the "space-charge" model. In order to verify the validity of the selected model that is characterized by formation of domains having excess negative charge due to the 1:1 ratio of B-cations rather than 1:2 of the main material that can be compensated by formation of oxygen vacancies, we performed resistivity measurements of two sets of samples: one that does not contain 1:1 cation order and a second one that contains a large amount of 1:1 ordered structure. Results of the measurements are shown in Figure 9.13. According to the presented data, the presence of 1:1 cation order results in lower resistivity values confirming the applicability of the "space-charge" model.

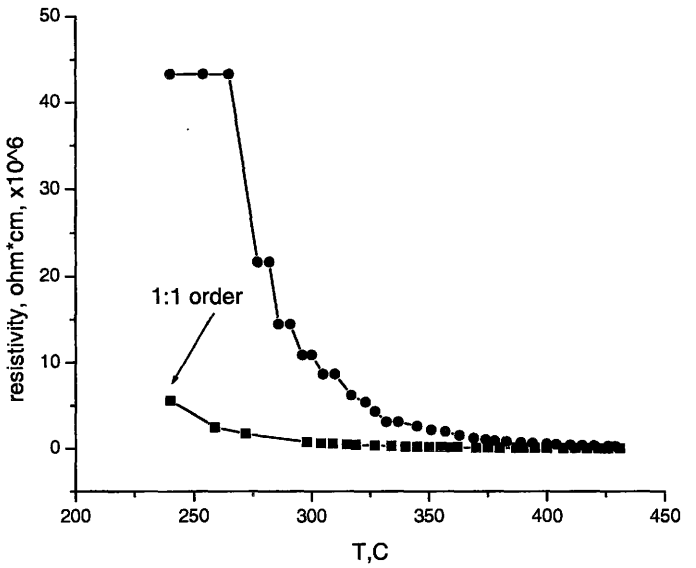

Figure 9.13 Comparison of resistivity measurements at different temperatures of a sample without 1:1 ordered cation arrangement and one containing the 1:1 ordered structure.

9.3 Discussion of Raman results

The appearance of Raman modes in nonstoichiometric perovskite materials has been ascribed to the formation of a 1:2 ordered structure based on group theory predictions of the dependence of Raman modes on the mass of heavier cations on the B-site as well as changes in the mode shapes with different degrees of cation ordering. In particular, Raman spectra of BMN and BMT perovskites demonstrating larger tendencies for cation ordering are sharp while those of BCN and BZN materials having lower degree of 1:2 order are diffuse and show a tendency to disappear. Increase in the degree of 1:2 cation order, as revealed by X-ray diffraction, leads to intensification of Raman modes and a change in the overall shape of the spectra. It has been shown that the dependence of the FWHM of the oxygen breathing-type mode on nonstoichiometry correlates with the

previously measured dielectric losses [200] indicating that a 1:2 cation ordering process caused by deviation from stoichiometry and mediated by changes in microstructure is responsible for the microwave losses in the considered materials. Crystallographic distortion along the [111] direction increases the average B-O bond length raising the bond's energy. The oxygen breathing-type mode can be represented by a simple harmonic oscillator model with frequency ω defined as:

$$\omega = \sqrt{\frac{k}{m^*}} \tag{9.1}$$

where m^* is the reduced mass of the $A_{1g}(O)$ mode and k is the force constant related to O-B and O-O bond strength. An increase in the energy of the $A_{1g}(O)$ mode caused by deviation from the nominal amounts of cations on either Ba- or B-sites according to the harmonic oscillator model indicates an increase in the bond stiffness. So, the appearance of the 1:2 ordered phase leads to formation of more rigid BO_6 octahedra. According to the Raman data showing a blue-shift of $A_{1g}(O)$ modes with an increase in formation pressure prior to sintering (Figure 9.10), changes in the grain growth rate induced by initial strain in materials and leading to higher cation ordering degree should result in lower microwave losses.

The formation of 1:1 cation order can be considered as an initial stage of the 1:2 ordering processes and often has been found to accompany 1:2 cation order [53,170]. It has been observed that an increase in the concentration of one type of order results in a decrease in the concentration of the other. Formation of oxygen vacancies that are necessary to maintain charge balance inside of 1:1 ordered domains is expected to

destabilize the structure leading to the red-shift of the $A_{1g}(O)$ mode. This explains the appearance of oxygen breathing-type modes from 1:1 cation order at lower energies to the respective mode from 1:2 cation order. Siny *et al* [167] correlated the position of the $A_{1g}(O)$ mode in $A(B',B'')O_3$ perovskites containing 1:1 and 1:2 cation order with the unit cell size. The authors demonstrated that materials having 1:1 order have an oxygen breathing-type mode at higher energies in contrast to the presently reported results. This is due to the difference in structural stability: materials containing 1:1 ratio of cations on the B-site and forming 1:1 order are more stable as opposed to those having 1:2 cation ratio and requiring charge compensation.

Results of positron lifetime spectroscopy presented in Chapter 7 for samples prepared by applying lower pressures (500-800kg/cm^2) demonstrated a decrease in the value of the bulk lifetime below theoretically predicted values for a disordered structure. In addition to changes in B-O bond strength, formation of excess negative charge inside of 1:1 nanoregions would create strong electric fields between ordered domains and the rest of the material [198]. Wang *et al* [203] observed changes in the positron migration characteristics in AlGaN/GaN heterostructures caused by the presence of a strong intrinsic electric field in the AlGaN layer that tends to move positrons from the hetero-interface toward the surface of AlGaN. Internal fields between the 1:1 ordered domains and regions rich in the Nb-cations can create conditions for the preferential annihilation of positrons in parts of the sample containing the 1:1 ordered domains. The presence of an excess of small Nb-cations with high electron density increases the average electron

density, in comparison to the main composition, at the interface between the 1:1 ordered domains and Nb-rich regions, thereby decreasing positron bulk lifetime.

9.4 Conclusions

Measured Raman active modes in $Ba(B'_{1/3}B''_{2/3})O_3$ (B′ = Mg,Co or Zn, B″ = Nb or Ta) have been ascribed to the 1:2 cation order based on the changes in the ordering degree (revealed by XRD) and predicted mode dependence on the mass of B-cation. The FWHM of the most intense $A_{1g}(O)$ mode representing collective motion of oxygen anions correlates with microwave losses previously measured by another research group. As has been demonstrated by Raman spectroscopy, 1:2 cation ordering process in addition to decreasing FWHM of $A_{1g}(O)$ mode results in formation of rigid BO_6 octahedra with the perovskite structure. Comparing different growth rates resulting from variations in preparation conditions used, it could be concluded that perovskite oxides sintered by applying higher formation pressure should possess lower microwave losses primarily due to increased degree of cation ordering. This demonstrates the possibility of further exploring modifications in the preparation process in order to optimize microwave properties of ceramic materials having perovskite structure.

Reduction in the amount of 1:2 order resulted in the formation of 1:1 cation order described by the "space-charge" model. The presence of oxygen vacancies within 1:1 ordered domains creates conditions for the preferential positron annihilation near 1:1 ordered domains surrounded by Nb-rich regions having larger electron density than the

rest of the material. It also leads to "softening" of oxygen octahedra and shifting of the $A_{1g}(O)$ vibration from 1:1 ordered structure toward lower energies.

9.5 Photoluminescence spectroscopy

Structural distortions in nonstoichiometric perovskites have also been studied by photoluminescence (PL) spectroscopy. The typical PL signals of stoichiometric

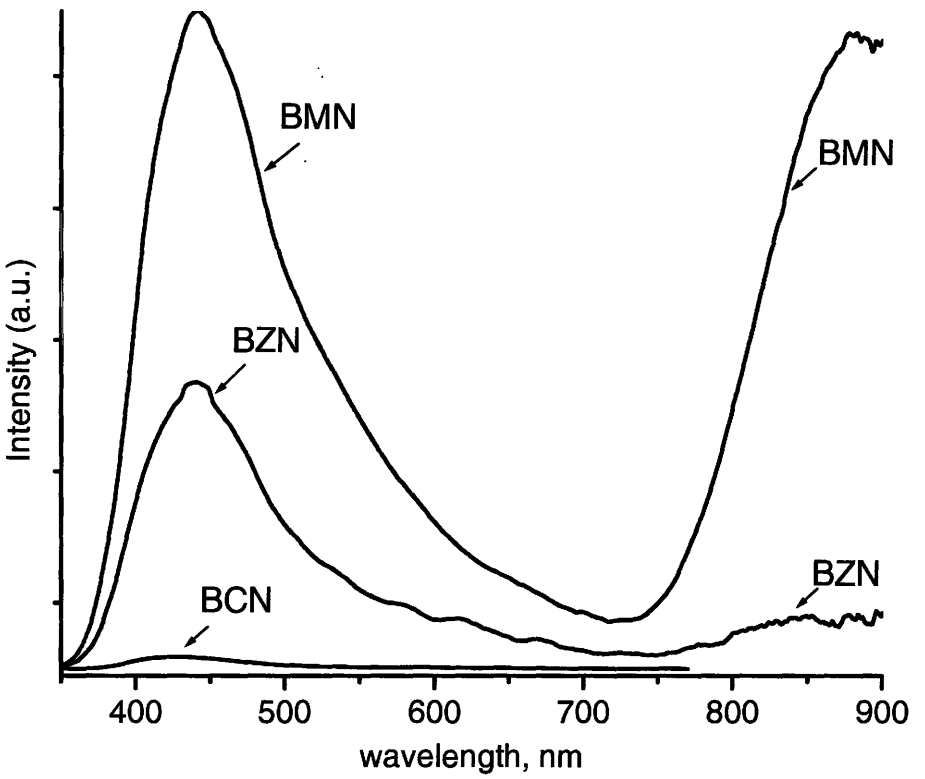

Figure 9.14 Photoluminescence spectra of $Ba(B'_{1/3}B''_{2/3})O_3$ (B' = Mg, Co or Zn, B'' = Nb or Ta) perovskites.

perovskite materials having different degree of 1:2 cation ordering are presented in Figure 9.14.

PL spectra are characterized by the appearance of two broad bands at approximately 430nm and 900nm with intensities as well as positions varying from sample to sample. Based on the correlation of structural data obtained from the X-ray diffraction and the appearance of PL bands (samples demonstrating complete disorder according to the X-ray diffraction data have only high energy PL band; while those containing 1:2 cation order, according to the X-ray measurements, have both high and low energy bands relative intensities of which coincides with the relative intensities of the X-ray peaks due to the disorder and 1:2 order) we made the following band assignment: the high energy band positioned around 430nm is ascribed to the presence of B-site cation disorder whereas 1:2 cation order gives rise to a low energy band at 900nm. The limited spectral range of the apparatus used did not permit a complete measurement of the low energy PL signal. Examination of the high-energy peak for niobium perovskites containing different cations on the B′-site shows that the band maximum gradually shifts from approximately 425nm for cobalt perovskites to 445nm for magnesium materials. Zinc perovskite occupies an intermediate position (440nm).

Deviation from stoichiometry leading to the appearance of cation deficient secondary phases modifies the PL spectra. Figure 9.15 shows PL signals of nonstoichiometric perovskites containing Ba- and B-site deficient secondary phases. Precipitation of the $Ba_6BNb_9O_{30}$ phase, the amount of which depends on the nonstoichiometry, facilitates grain growth and intensifies the PL signal (Figure 9.15a).

Grain boundaries represent broken bonds and are the source of a large number of defects. Increase in the size of grains due to precipitation of the Ba-deficient phase results in a reduction of grain surface leading to smaller number of defects connected with a surface. The origin of the PL signal is a charge transfer transition from transition metal d^0 orbital to p orbitals of oxygen. The presence of vacancies on either oxygen positions or on cation sites participating in the absorption process would result in reduced emission. In the considered perovskites the most probable defect types present on the surface are cation vacancies. So, changes in the intensity of the PL signal with grain size are probably due to the reduced number of cation defects.

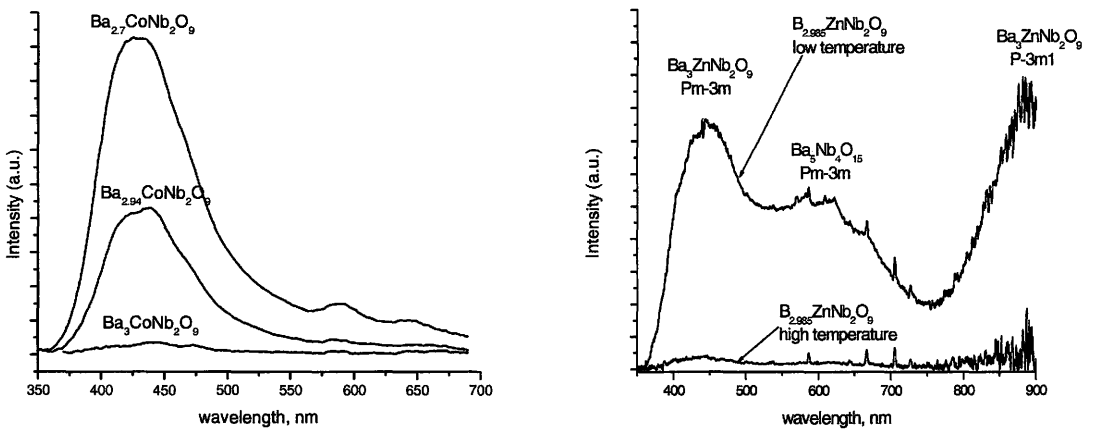

a) b)

Figure 9.15 PL signal of nonstoichiometric perovskites.

Formation of B-cation deficient phases resulting from either deviation from the stoichiometry on the B-sites, or loss of respective oxide (ZnO in zinc perovskites samples), results at first in the appearance of an additional band at low level of B-cation deficiencies that peaks at 600 nm, which was attributed to a $Ba_5Nb_4O_{15}$ phase (Figure

9.15b, $B_{2.985}ZnNb_2O_9$ material sintered at lower, 1350°C, temperature) and then to a decrease in the overall signal with the appearance of a $Ba_8BNb_6O_{24}$ phase (Figure 9.15b, $B_{2.985}ZnNb_2O_9$ material sintered at higher, 1445°C, temperature). The position of the emission maximum of the $Ba_5Nb_4O_{15}$ structure is close to that reported by Srivastava *et al* [204] at 575nm.

9.6 Discussion of photoluminescence spectroscopy' results

Numerous experimental studies, confirmed by first principle calculations, on the emission properties of transition metal ions in oxygen environments indicate that the absorption and re-emission of electromagnetic radiation in the optical range is due to the charge transfer from the highest occupied molecular orbitals formed mostly from the oxygen atomic orbitals (*2p*) to the lowest unoccupied molecular orbitals formed from transition metal (TM) atomic orbitals (nd^0) [175-177,205]. Atomic orbitals of isolated transition metal atoms are characterized by five-fold degeneracy (d_{xy}, d_{xz}, d_{yz}, $d_{x^2-y^2}$ and d_{z^2}) that can be removed by placing an atom in a crystal lattice. Perovskite oxides $Ba(B'_{1/3}B''_{2/3})O_3$ having disordered cubic structure with a Pm-3m space group form octahedral arrangements around the B″-cation. Octahedral symmetry of the BO_6^{-7} complex partially removes degeneracy by moving e_g molecular orbitals (formed from $d_{x^2-y^2}$ and d_{z^2} atomic orbitals of TM) to higher energies and t_{2g} molecular orbitals (formed from d_{xy}, d_{xz}, d_{yz} atomic orbitals of TM) to lower energies. The latter can mix with oxygen orbitals. Lowering in symmetry from cubic to hexagonal due to 1:2 cation order causes expansion of the cubic cell along the [111] direction and a change in the mutual

orientation of atomic orbitals within BO_6^{-7} complex. Repulsion between ligand orbitals and $d_{x^2-y^2}$ and d_{z^2} orbitals of TM that were pointing toward ligands in the case of cubic symmetry decreases causing lowering in energy of e_g molecular orbitals. Thus, the band gap of the 1:2 ordered structure decreases. This explains the appearance of a low-energy PL band, the intensity of which correlates with the intensity of the high energy band: increase in the degree of 1:2 order results in intensification of the low energy PL peak and decrease in the intensity of high energy peak. Results of PL measurements agree with conclusions of Blasse *et al* [180] that studied $Ba_3SrB"_2O_9$ (B" = Nb and Ta) perovskites exhibiting order-disorder phase transition and observed formation of two emission bands. The authors attributed the appearance of two bands to the coexistence of two distinct $B"O_6$ octahedral structures having slightly different oxygen environment.

Change in the band-gap caused by correlated displacement of oxygen anions during ordering process and leading to changes in spatial overlap between transition metal-ligand orbitals can also be sensitive to out of center motion of the d^0 TM cations. The value of unit cell distortion in $Ba(B'_{1/3}Nb_{2/3})O_3$ perovskites caused by the Nb-cation depends on the stiffness of B′-O (B′ = Mg, Co or Zn) bonds forming a network around the NbO_6 octahedron or the ability of B′ ions to stabilize distortion. The difference in electronegativities of cations and anions forming B-O bonds defines how covalent or ionic a bond is. According to the Pauling electronegativity table, Co^{2+} forms more covalent bonds with oxygen anions followed by Zn^{2+} cations. In the case of magnesium containing perovskites Mg-O forms a softer ionic bond. More rigid CoO_6 octahedra can stabilize the distortion of adjacent NbO_6 oxygen complexes while the softer MgO_6

structure cannot as effectively stabilize distortion of neighboring NbO_6 octahedra resulting in smaller repulsion between ligands and e_g orbitals of Nb^{5+}. This leads to a change in the position of the observed PL bands: BCN perovskites containing rigid CoO_6 octahedra produce emission at higher energies while the emission signal of BMN materials with more ionic MgO_6 octahedra is red-shifted. These conclusions are in agreement with the results of Lufaso [66] for 1:2 ordered structures of $Ba(Mg_{1/3}Nb_{2/3})O_3$, $Ba(Zn_{1/3}Nb_{2/3})O_3$ and $Ba(Ni_{1/3}Nb_{2/3})O_3$ perovskites taking into account the similarity in electronegativities of Co and Ni ions that revealed different amount of NbO_6 distortion depending on the neighboring B′ cation (B′ = Mg, Zn or Ni).

Chapter 10

Conclusions and Suggestions for Future Work

This chapter summarizes several important results obtained during our investigation of near stoichiometric compositions of $Ba_{3+3x}B'_{1+y}Nb_2O_9$ (B' = Co or Zn) perovskites and suggests some aspects of the studied ceramic materials that could be addressed during future work.

The studied oxides having perovskite structure remain stable in a narrow range of nonstoichiometries on Ba- and B'-sites. Introduction of interstitial ions in perovskite materials containing an excess of cations is energetically unfavorable because of the close packing of the structure and leads to precipitation of secondary phases. Secondary phase formation was also observed in materials having large cation deficiencies due to the changes in the tolerance factor beyond the stability values commonly observed for a perovskite structure. Moderate amounts of cation deficiencies promote 1:2 cation order due to an increased number of available defect sites for cation diffusion in the case of B'-site nonstoichiometry and distortion of the lattice potential caused by "missing oversized" barium atoms. Formation of 1:2 ordered domains depends on the induced strain that changes the grain growth rate. Future work can be concentrated on the TEM measurements to reveal changes in the microstructure with strain present in the system in order to find the optimum pressure during pressing of precursor materials.

Formation of B-site deficient phases ($Ba_5Nb_4O_{15}$ and $Ba_8B'Nb_6O_{24}$) having an ordered arrangement of cation vacancies in perovskite materials having tolerance factors

above unity can relax their structure. It has been observed that the microstructure of materials containing $Ba_5Nb_4O_{15}$ and $Ba_8B'Nb_6O_{24}$ phases is characterized by close grain packing with minimal distance between grains and depends on the grain growth rate. High resolution TEM accompanied by neutron diffraction measurements could be used to study the local cation environment including the determination of the B-O bond length around secondary phases.

It was demonstrated that commonly observed Raman spectra of $Ba(B'_{1/3}B''_{2/3})O_3$ perovskite oxides originate from 1:2 cation order rather than 1:1 ordered nanodomains. Formation of the 1:1 cation order manifests itself in the appearance of an additional mode attributed to the $A_{1g}(O)$ type vibration. To understand the change in the phonon spectra of the 1:1 ordered structure described by the "space-charge" model, first principle calculations could be done. Formation of both types of cation order was observed through appearance of {h±1/3,k±1/3,l±1/3} and {h±1/2,k±1/2,l±1/2} reflections on electron diffraction patterns. In order to understand the origin of the coexistence of both types of cation order (whether both of them form on the same structural defects or there is a phase transition between 1:1 and 1:2 ordered structures) high resolution TEM could be used.

Emission properties of $Ba_{3+3x}B'_{1+y}Nb_2O_9$ (B' = Co or Zn) perovskites originate from the presence of NbO_6^{-7} group as well as formation of secondary phases. It was shown that trigonal distortion resulting from 1:2 cation order leads to the appearance of two photoluminescence bands with band maxima at approximately 430nm and 900nm, respectively for disordered and 1:2 ordered structures. Formation of the $Ba_5Nb_4O_{15}$ phase results in the emergence of an additional band having a band maximum at 600nm. A

semi-empirical approach was used to interpret the optical properties of the considered materials. First principle calculations on a molecular orbital level scheme are required. By carefully controlling preparation conditions and stoichiometry it is possible to produce ceramic materials with emission bands covering the visible range.

References

1 W. Wersing. Curr. Opin. Sol. State Mater. Sci., 1:715, 1996

2 R.J. Cava. J. Mater. Chem., 11:54, 2001

3 H. Tamura. Am. Ceram. Soc. Bull., 73:92, 1994

4 H.M. O'Bryan, J. Thomson and J.K. Plourde. J. Am. Ceram. Soc., 57:450, 1974

5 J.K. Plourde, D. F. Linn, H.M. O'Bryan and J. Thomson. J. Am. Ceram. Soc., 58:418, 1975

6 T. Negas, G. Yeager, S. Bell, N. Coats and I. Minis. Am. Ceram. Soc. Bull., 72:80, 1993

7 K. Wakino, K. Minai and H. Tamura. J. Am. Ceram. Soc., 67:278, 1984

8 F. Galasso and J. Pyle. J. Phys. Chem., 67:533, 1963

9 F. Galasso and J. Pyle. Inorg. Chem., 2:482, 1963

10 F. Galasso, J.R. Barrante and L. Katz. J. Am. Chem. Soc., 83:2830, 1961

11 S. Kawashima, M. Nishida, I. Ueda and H. Ouchi. J. Am. Ceram. Soc., 66:421, 1983.

12 K. Matsumoto, T. Hiuga, K. Takada and H. Ichimura. Proceedings of the 6th IEEE International Symposium on Application of Ferroelectrics. Pp118-121, 1986

13 P.K. Davies, J. Tong and T. Negas. J. Am. Ceram. Soc., 80:1727, 1997

14 L. Chai and P.K. Davies. J. Am. Ceram. Soc., 80:3193, 1997

15 I. Molodetsky and P.K. Davies. J. Eur. Ceram. Soc., 21:2587, 2001

16 J.-I. Yang, S. Nahm, C.-H. Choi, H.-J. Lee, J.-C. Kim and H.-M. Park. Jpn. J. Appl. Phys., 41:702, 2002

17 J.-I. Yang, S. Nahm, C.-H. Choi, H.-J. Lee and H.-M. Park. J. Am. Ceram. Soc., 85:165, 2002

18 M.-H. Kim, S. Nahn, W.-S. Lee, M.-J. Yoo, J.-C. Park and H.-J. Lee. Jpn. J. Appl. Phys., 43:1438, 2004

19 W.-A. Lan, M.-H. Liang, C.-T. Hu, K.-S. Liu and I.-N. Lin. Mater. Chem. Phys., 79:266, 2003

20 S.M. Moussa, R.M. Ibberson, M. Bieringer, A.N. Fitch and M.J. Rosseinsky. Chem. Mater., 15:2527, 2003

21 C.-H. Lu and C.-C. Tsai. J. Mater. Res., 11:1219, 1996

22 J.H. Paik, S. Nahm, J.D. Bylin, M.H. Kim and H.J. Lee. J. Mater. Sci. Lett., 17:1777, 1998

23 S.B. Desu and H.M. O'Bryan. J. Am. Ceram. Soc., 68:546, 1985

24 I.-T. Kim, K.S. Hong and S.-J. Yoon. J. Mater. Sci., 30:514, 1995

25 K.P. Surendran, M.T. Sebastian, P. Mohanan, R.L. Moreira and A. Dias. Chem. Mater., 17:142, 2005

26 J.-K. Park, D.-Y. Kim and N.-M. Hwang. Scripta. Mater., 44:195, 2001

27 M.P. Harmer, J. Chen, P. Peng, H.M. Chan and D.M. Smyth. Ferroelectrics, 97:263, 1989

28 R.H. Mitchell. *Perovskites: Modern and Ancient.* Thunder Bay, Ont.: Almaz Press, 2002

29 V.M. Goldschmidt. Geochemische Verterlungsgesetze der Elemente. Norske Videnskap, Oslo, 1927

30 V.M. Goldschmidt. Skr. Nor. Vidensk.-Akad., 1:1, 1926

31 H.D. Megaw. Proc. Phys. Soc., 58:133, 1946

32 J.B. Goodenough and J.M. Longo. In *Landolt-Bornnstein* New Series, K.H. Hellwege, A.M. Hellwege, Eds., Springer-Verlag, Berlin, vol. 4, part A

33 J.B. Goodenough. In *Solid State Chemistry*. C.N.R. Rao, Ed., Marcel Dekker, New York, 1974

34 S.A. Speakman, J.W. Richardson, B.J. Mitchell and S.T. Misture. Solid State Ionics, 149:247, 2002

35 J.M. Gonzalez-Calbet, M.J. Sayagues and M. Vallet-Regi. Solid State Ionics, 32:721, 1989

36 J.P. Hodges, S. Short, J.D. Jorgensen, X. Xiong, B. Dabrowski, S.M. Mini and C.W. Kimball. J. Solid State Chem., 151:190, 2000

37 B.C. Tofield and W.R. Scott. J. Solid State Chem., 10:183, 1974

38 M.A. Pena and J.L.G. Fierro. Chem. Rev., 101:1981, 2001

39 A. M. Abakumov, G. Van Tendeloo, A.A. Scheglov, R.V. Shpanchenko and E.V. Antipov. J. Solid State Chem., 125:102, 1996

40 R. Roy. J. Am. Ceram. Soc., 37:581, 1954

41 P.K. Davies. Curr. Opin. Solid State Mater. Sci., 4:467, 1999

42 J.H. Park, P.M. Woodward and J.B. Parise. Chem. Mater., 10:3092, 1998

43 Y. Harada, T. Ishigaki, H. Kawai and J. Kuwano. Solid State Ionics, 108:407, 1998

44 S.G. Steward and H.P. Rooksby. Acta Crystallogr., 4:503, 1951

45 F. Galasso. *Structure, properties and preparation of perovskite type compounds.* Pergamon Press, 1969

46 A.W. Sleight. Ph.D. Thesis, Univ. of Connecticut, 1963

47 M.T. Anderson, K.B. Greenwood, G.A. Taylor and K.R. Poeppelmeier. Prog. Solid State Chem., 22:197, 1993

48 I. Levin, J.Y. Chan, J.E. Maslar, T.A. Vanderah and S.M. Bell. J. Appl. Phys., 90:904, 2001

49 P.M. Woodward. Ph.D. Thesis, Oregon State Univ., 1997

50 N. Setter and L.E. Cross. J. Appl. Phys., 51:4356, 1980

51 N. Setter. Ph.D. Thesis, Penn. State Univ., 1980

52 K. Ramesha, V. Thangadurai, D. Sutar, S.V. Subramanyam, G.N. Subbanna and J. Gopalakrishnan. Mater. Res. Bull., 35: 559, 2000

53 D.J. Barber, K.M. Moulding, J. Zhou and M. Li. J. Mater. Sci., 32:1531, 1997

54 Y. Du and A.S. Nowick. J. Am. Chem. Soc., 78:3033, 1995

55 H. Vincent, C. Perrier, P. I'Heritier and M. Labeyrie. Mater. Res. Bull., 28:951, 1993

56 A. Alonso, E. Mzayek and I. Rasines. Mater. Res. Bull., 22:69, 1987

57 M.A. Subramanian. J. Solid State Chem., 111:134, 1994

58 J.A. Alonso, E. Mzayek and I. Rasines. J. Solid State. Chem., 84:16, 1990

59 P.K. Davies, H. Wu, A.Y. Borisevich I.E. Molodetsky and L. Farber. Annu. Rev. Mater. Res., 38:369, 2008

60 A.Y. Borisevich and P.K. Davies. J. Solid State Chem., 170:198, 2003

61 I.T. Kim, Y.H. Kim and S.J. Chung. J. Mater. Res., 12: 518, 1997

62 I.T. Kim, T.S. Oh and Y.H. Kim. J. Mater. Sci. Lett., 12: 182, 1993

63 A.F. Fuentes, M. Garza-Garcia, J.I. Escalante-Garcia, G. Mendoza-Suarez, K. Boulahya and U. Amador. J. Solid State Chem., 175: 299, 2003

64 J. Berthon, J.C. Grenet and P. Poix. Ann. Chim. (Paris), 8:609, 1979

65 D. Harari and P. Poix. Comput. Rend. Hebdom., C276:265, 1973

66 M. W. Lufaso. Chem. Mater., 16:2148, 2004

67 U. Treiber and S. Kemmler-Sack. Z. Anorg. Allg. Chem., 487:161, 1982

68 D. Harari, P. Poix and J.C. Bernier. J. Solid State Chem., 11:330, 1974

69 J. Chen, H.M. Chan and M.P. Harmer. J. Am. Ceram. Soc., 72:593, 1989

70 M.A. Akbas and P.K. Davies. J. Am. Ceram. Soc., 80:2933, 1997

71 T.-F. Tsai, M.-H. Lin, R.-Y. Yang and H.-Y. Lu. Mater. Sci. Eng. A, 372:56, 2004

72 G.A. Smolenskii and A.I. Agranovskaya. Soviet Phys.- Solid State, 1:1429, 1960

73 L.E. Cross. Ferroelectrics, 76:241, 1987

74 B.P. Burton. Model. Simul. Mater. Sci. Eng., 8:211, 2000

75 V. Primo-Martin and M. Jansen. J. Solid State Chem., 157:76, 2001

76 M.A. Akbas and P.K. Davies. J. Am. Ceram. Soc., 81:670, 1998

77 H.J. Youn, K.S. Hong and H. Kim. J. Mater. Res., 12:589, 1997

78 M.A. Akbas and P.K. Davies. J. Am. Ceram. Soc., 81:1061, 1998

79 L. Chai and P.K. Davies. J. Am. Ceram. Soc., 80:3193, 1997

80. H. Tamura, T. Konoike, Y. Sakabe and K. Wakino. J. Am. Ceram. Soc., 67:C59, 1984

81 P.K. Davies. Pp137-52 in *Ceramic Transactions*, Vol. 53, Materials and Processes for Wireless Communication. Edited by T. Negas and H. Ling. American Ceramic Society, Westerville, OH, 1995

82 M. Kunz and I.D. Brown. J. Solid State Chem., 115:395, 1995

83 A.M. Glazer. Acta Crystallogr., Sect. B, 28:3384, 1972

84 P.M. Woodward. Acta Crystallogr., Sect. B, 53:32, 1997

85 I.M. Reaney, E.L. Colla and N. Setter. Jpn. J. Appl. Phys., 33:3984, 1994

86 H. Zhang, N. Li, K. Li and D. Xue. Acta Crystallogr. B, 63:812, 2007

87 A. Belsky, M. Hellenbrandt, V.L. Karen and P. Luksch. Acta Crystallogr. B, 58:364, 2002

88 A.J. Jacobson, B.M. Collins and B.E.F. Fender. Acta Cryst. B, 32:1083, 1976

89 P. Lemmens, G. Guntherodt and C. Gros. Physics Reports, 375:1, 2003

90 J.A. Alonso, M.T. Casais, M.J. Martinez-Lope, J.L. Martinez, P. Velasco, A. Munoz and M.T. Fernandez-Diaz. Chem. Mater., 12:161, 2000

91 M.del C. Viola, M.J. Martinez-Lope, J.A. Alonso, P. Velasco, J.L. Martinez, J.C. Pedregosa, R.E. Carbonio and M.T. Fernandez-Diaz. Chem. Mater., 14:812, 2002

92 A.D. Hilton, D.J. Barber, C.A. Randall and T.R. Shrout. J. Mater. Sci., 25:3461, 1990

93 F. Zhao, Z. Yue, Z. Gui and L. Li. Jpn. J. Appl. Phys., 44:8066, 2005

94 M. Takata and K Kageyama. J. Am. Ceram. Soc., 72:1955, 1989

95 R. Zurmuhlen, E.L. Colla, D.C. Dube, J. Petzelt, I. Reaney, A. Bell and N. Setter. J. Appl. Phys., 76:5864, 1994

96 H. Sreemoolanadhan, R. Ratheesh, M.T. Sebastian and P. Mohanan. Mater. Lett., 33:161, 1997

97 R.D. Richtmyer. J. Appl. Phys., 10:391, 1939

98 W. Wersing. In *Electronic Ceramics*. B.C. Steele editor. London and New York: Elsevier Applied Science; 67-199, 1991

99 A.P.S. Khanna. *Dielectric Resonators*. D. Kajfez and P. Guillon editors. Artech. House, Norwood, 1986

100 S.J. Fiedziuszko, I.C. Hunter, T. Itoh, Y. Kobayashi, T. Nishiwaka, S.N. Stitzer and K. Wakino. IEEE Trans. Microwave Theory Tech., 50:706, 2002

101 C.L. Huang, J.J. Wang, B.J. Li and C.F. Shih. Mater. Lett., 62:2516, 2008

102 I.M. Reaney and D. Iddles. J. Am. Ceram. Soc., 89:2063, 2006

103 Y.J. Wu and X.M. Chen. J. Eur. Ceram. Soc., 19:1123, 1999

104 A.G. Belous and O.V. Ovchar. J. Eur. Ceram. Soc., 19:1119, 1999

105 C.C. Lee and P. Lin. Jpn. J. Appl. Phys., 37:878; 1998

106 Y.I. Gornikov, Z.Y. Makarova, A.G. Belous, L.G. Gavrilova, V.M. Paskov and V.P. Chalyi. Sov. Prog. Chem., 50:1243, 1984

107 M. Valant, D. Suvorov, C. Hoffmann and H. Sommariva. J. Eur. Ceram. Soc., 21:2647; 2001

108 H. Takahashi, Y. Baba, K. Ezaki, Y. Okamoto, K. Shibata, K. Kuroki and S. Nakano. Jpn. J. Appl. Phys., 30:2339, 1991

109 A.G. Belous and O.V. Ovchar. Ukrainskii Khimicheskii Zhurnal, 61:73, 1995

110 E.L. Colla, I.M. Reaney and N. Setter. Ferroelectrics, 133:217, 1992

111 O. Steiner, E. Colla, I.M. Reaney and N. Setter. Conf. Proc. Eur. Ceram. Soc., Madrid, 2:223, 1993

112 S. Nishigaki, H. Kato, S. Yano and R. Kamimura. Am. Ceram. Soc. Bull., 66:1405, 1987

113 A.G. Belous. J. Eur. Ceram. Soc., 21:2717, 2001

114 S. Nomura. Ferroelectrics, 49:61; 1983

115 W.-Y. Lin, R.F. Speyer, W.S. Hackenberger and T.R. Shrout. J. Am. Ceram. Soc., 82:1207, 1999

116 S. Nomura, K. Toyama and K. Kaneta. Jpn. J. Appl. Phys., 21:L624, 1982

117 H. Matsumoto, H. Tamura and K. Wakino. Jpn. J. Appl. Phys., 30:2347, 1991

118 M. Onoda, J. Kuwata, K. Kaneta, K. Toyama and S. Nomura. Jpn. J. Appl. Phys., 21:1707, 1982

119 C.-W. Ahn, H.-J. Jang, S. Nahm, H.-M. Park and H.-J. Lee. J. Eur. Ceram. Soc., 23:2473, 2003

120 F. Azough, C. Leach and R. Freer. J. Eur. Ceram. Soc., 26:2877, 2006

121 T. Kolodiazhnyi, A. Petric, A. Belous, O. V'yunov and O. Yanchevskij. J. Mater. Res., 17:3182, 2002

122 K. Endo, K. Fujimoto and K. Murakawa. J. Am. Ceram. Soc., 70:C215, 1987

123 T. Takahashi. Jpn. J. Appl. Phys., 39:5637, 2000

124 Y. Dai, G. Zhao and H. Liu. J. Appl. Phys., 105:034111, 2009

125 L. Bellaiche and D. Vanderbilt. Phys. Rev. Lett., 81:1318, 1998

126 A.K. Tagantsev, J. Petzelt and N. Setter. Solid State Comm., 87:1117, 1993

127 R. Zurmuhlen, J. Petzelt, S. Kamba, G. Kozlov, B. Volkov, B. Gorshunov, D.C. Dube, A. Tagentsev and N. Setter. J. Appl. Phys., 77:5341, 1995

128 E. Schlomann. Phys. Rev., 135:A413, 1964

129 L. Chai, M.A. Akbas, P.K. Davies and J.B. Parise. Mater. Res. Bull., 32:1261, 1997

130 I. Qazi, I.M. Reaney and W.E. Lee. J. Eur. Ceram. Soc., 21:2613, 2001

131 H. Yoshioka. Bull. Chem. Soc. Jpn., 60:3433, 1987

132 P.J.W. Debye. Berichte der Deutschen Physikalischen Gesellschaft. 15:777, 1913

133 V.L. Gurevich and A.K. Tagantsev. Adv. Phys., 40:719, 1991

134 V.L. Gurevich. Transport in Phonon Systems. North-Holland, Amsterdam, 1986

135 R. Stolen and K. Dransfeld. Phys. Rev. A, 139:1295, 1965

136 G.J. Coombs and R.A. Cowley. J. Phys. C, 6:121, 1973

137 K.H. Yoon, D.P. Kim and E.S. Kim. J. Am. Ceram. Soc., 77:1062, 1994

138 Y.-K. Kim, K.-M. Lee and H.M. Jang. J. Korean. Phys. Soc., 32:S292, 1998

139 E.J. Fresia, L. Katz and R. Ward. J. Am. Chem. Soc., 81:4783, 1959

140 W.C. Mackrodt. Phil. Trans. Roy. Soc. Lond., 341:301, 1992

141 A. Zangwill. *Physics of Surfaces*. Cambridge University Press, Cambridge, 1988

142 J.W. Christian. *The Theory of Transformations in Metals and Alloys*. Vol.1, Pergamon Press, Oxford, 1975

143 A.A. Bokov, I.P. Rayevskii, V.G. Smotrakov and O.I. Prokopalo. Phys. Stat. Sol. A, 93:411, 1986

144 O.I. Prokopalo. Izv. Akad. Nauk. SSSR, Ser. Fiz., 35:1956, 1971

145 O.I. Prokopalo. Izv. Akad. Nauk. SSSR, Ser. Fiz., 39:995, 1975

146 C.A. Randall, D.J. Barber, R.W. Whatmore and P. Groves. J. Mater. Sci., 21:4456, 1986

147 K. Matsumoto, T. Hiuga, K. Takada and H. Ichimura. 6th IEEE International Symposium on Applications of Ferroelectrics (IEEE, Piscataway, NJ, 1986), p.118

148 R. Kudesia, A.E. McHale, R.A. Condrate and R.L. Snyder. J. Mater. Sci., 28:5569, 1993

149 K. Fukuda, R. Kitoh and I. Awai. J. Am. Ceram. Soc., 77:149, 1994

150 Y.-C. Chen, H.-F. Cheng, H.-L. Liu, C.-T. Chia and I-N. Lin. J. Appl. Phys., 94:3365, 2003

151 K. Tochi and N. Takeuchi. J. Mater. Sci. Lett., 8:1144, 1989

152 D.L. Rousseau, R.P. Bauman and S.P.S. Porto. J. Raman. Spectroscopy, 10:253, 1981

153 J. Petzelt, S. Pacesova, J. Fousek, S. Kamba, V. Zelezny, V. Koukal, J. Schwarzbach, B.P. Gorshunov, G.V. Kozlov and A.A. Volkov. Ferroelectrics, 93:77, 1989

154 J. Petzelt, R. Zurmuhlen, A. Bell, S. Kamba, G.V. Kozlov, A.A. Volkov and N. Setter. Ferroelectrics, 133:205, 1992

155 G. Burns and B.A. Scott. Solid State Commun., 13:423, 1973

156 M.E. Lines and A.M. Glass. *Principles and Applications of Ferroelectrics and Related Materials*. Clarendon Press, Oxford, 1977

157 S.K. Manlief and H.Y. Fan. Phys. Rev. B, 5:4046, 1972

158 U. Bismayer, V. Devarajan and P. Groves. J. Phys. Condensed Matter, 1:6977, 1989

159 B.E. Douglas and C.A. Hollingsworth. *Symmetry in Bonding and Spectra. An Introduction.* Academic Press Inc., Orlando, 1985

160 G.A. Smolensky, I.G. Siny, R.V. Pisarev and E.G. Kuzminov. Ferroelectrics, 12:135: 1976

161 I. Gregora, J. Petzelt, J. Pokomy, V. Vorlicek, Z. Zikmund, R. Zurmuhlen and N. Setter. Solid State Commun., 94:899, 1995

162 R. Tao, I.G. Siny, R.S. Katiyar, R. Guo and A.S. Bhalla. J. Raman Spectrosc., 27:873, 1996

163 H. Tamura, D.A. Sagala and K. Wakino. Jpn. J. Appl. Phys., 25:787, 1986

164 E. Koga, H. Moriwake, K.-I. Kakimoto and H. Ohsato. Ferroelectrics 356:146, 2007

165 S. Kamba, H. Hughes, D. Noujni, S. Surendran, R.C. Pullar, P. Samoukhina, J. Petzelt, R. Freer, N. Mcn Alford and D.M. Iddles. J.Phys. D: Appl. Phys., 37:1980, 2004

166 R. Tao, A.R. Guo, C.-S. Tu, I. Siny, R.S. Katiyar, R. Guo and A.S. Bhalla. Ferroelectrics Lett., 21:79, 1996

167 I.G. Siny, R. Tao, R.S. Katiyar, R. Guo and A.S. Bhalla. J. Phys. Chem. Solids, 59:181, 1998

168 R.L. Moreira, F.M. Matinaga and A. Dias. Appl. Phys. Lett., 78:428, 2001

169 A. Dias, V.S.T. Ciminelli, F.M. Matinaga and R.L. Moreira. J. Eur. Ceram. Soc., 21:2739, 2001

170 C.-T. Lee, Y.-C. Lin, C.-Y. Huang, C.-Y. Su and C.-L. Hu. J. Am. Ceram. Soc., 90:483, 2007

171 B.-K. Kim, H.-O. Hamaguchi, I.-T. Kim and K.S. Hong. J. Am. Ceram. Soc., 78:3117, 1995

172 C.-T. Chia, Y.-C. Chen, H.-F. Cheng and I.-N. Lin. J. Appl. Phys., 94:3360, 2003

173 I.G. Siny, R.S. Katiyar and A.S. Bhalla. J. Raman Spectr., 29:385, 1998

174 M. W. Lufaso, E. Hopkins, S.M. Bell and A. Llobet. Chem. Mater., 17:4250, 2005

175 T. Ziegler, A. Rauk and E.J. Baerends. Chem. Phys., 16:209, 1976

176 A.H. Kahn and A.J. Leyendecker. Phys. Rev., 135:A1321, 1964

177 R.E. Cohen. J. Phys. Chem. Solids, 57:1393, 1996

178 R. Courths. Ferroelectrics, 26:749, 1980

179 J.H.G. Bode and A.B.V. Oosterhout. J. Luminescence, 10: 237, 1975

180 G. Blasse, G.J. Dirksen and D.J.W. Ijdo. Mat. Res. Bull., 18: 721, 1983

181 W.D. Kingery. Introduction to Ceramics. New York: Wiley, 1976

182 Y.-S. Yoo, H. Kim and D.-Y. Kim. J. Eur. Ceram. Soc., 17:805, 1997

183 H. Song and R.L. Coble. J. Am. Ceram. Soc., 73:2077, 1990

184 D. Grebennikov. M.A.Sc. Thesis, McMaster University, 2007

185 R. Krause-Rehberg and H.S. Leipner. *Positron Annihilation in Semiconductors. Defect Studies*. Germany: Springer, 1999

186 M.J. Puska and R.M. Nieminen. Rev. Modern Phys., 66:841, 1994

187 V.J. Ghosh, B. Nielsen and T. Friessnegg. Phys. Rev. B, 61:207, 2000

188 A.S. Hamid, A. Uedono, T. Chikyow, K. Uwe, K. Mochizuki and S. Kawaminami. Phys. Stat. Sol. A, 203:300, 2006

189 K. Suvegh, A. Domjan, R. Tarsoly and A. Vertes. J. Radioanal. Nucl. Chem., 211:255, 1996

190 D.J. Keeble, S. Singh, R.A. Mackie, M. Morozov, S. McGuire and D. Damjanovic. Phys. Rev. B, 76:144109, 2007

191 I.M. Reaney, I. Qazi and W.E. Lee. J. Appl. Phys., 88:6708, 2000

192 T. Kolodiazhnyi. PhD Thesis, McMaster University, 2002

193 P. Kirkegaard, N.J. Pedersen and M. Eldrup. PATFIT-88 : a data-processing system for positron annihilation spectra on mainframe and personal computers (Risφ National Laboratory, Denmark, 1989)

194 T.V. Kolodiazhnyi, A. Petric, G.P. Johari and A.G. Belous. J. Eur. Ceram. Soc., 22:2013, 2002

195 T.A. Vanderah, T.R. Collins, W. Wong-Ng, R.S. Roth and L. Farber. J. Alloys Comp., 346:116, 2002

196 P.W. Mallinson, M.M.B. Allix, J.B. Claridge, R.M. Ibberson, D.M. Iddles, T. Price and M.J. Rosseinsky. Angew. Chem. Int. Ed., 44:7733, 2005

197 U. Lehmann and H. Meuller-Buschbaum. Z. Anorg. Allg. Chem., 481:7, 1981

198 D. Grebennikov and P. Mascher. J. Appl. Phys. Accepted for publication

199 M.W. Lufaso and P.M. Woodward. Acta Crystallogr. Sect. B, 57:725, 2001

200 A.G. Belous, O.V. Ovchar, O.V. Kramarenko, J. Bezjak, B. Jancar, D. Suvorov and G. Annino. Ferroelectrics, 367:149, 2008

201 M. Sugiyama and T. Nagai. Jpn. J. Appl. Phys., 32:4360, 1993

202 I. Gregora, J. Petzelt, J. Pokomy, V. Vorlicek, Z. Zikmund, R. Zurmuhlen and N. Setter. Solid State Commun., 94:899, 1995

203 M. Wang, C.C. Cheng, C.D. Beling, S. Fung and K.J. Chen. Phys. Status Solidi A, 207:1332, 2010

204 A.M. Srivastava, J.F. Ackerman and W.W. Beers. J. Solid State Chem., 134:187, 1997

205 G. Blasse. Structure and Bonding, 42:1, 1980